27
7-19-77
250 NTIS

UCRL-52275

SYSTEMATICS OF GAMMA DECAY THROUGH LOW-LYING VIBRATIONAL LEVELS OF EVEN-EVEN NUCLEI EXCITED BY (p,p') AND (n,n') REACTIONS

Ronald Paul Koopman

(Ph.D. Thesis)

June 30, 1977

Prepared for U.S. Energy Research & Development Administration under contract No. W-7405-Eng-48

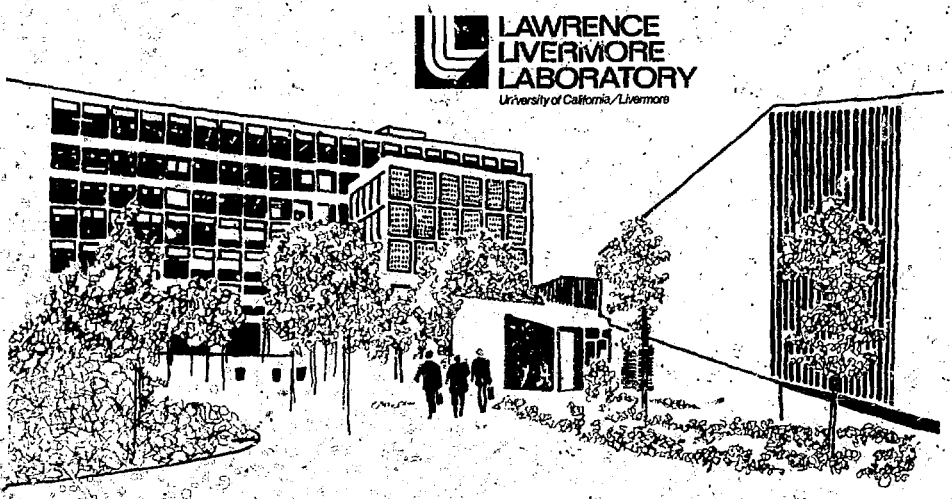

Printed in the United States of America
Available from
National Technical Information Service
U.S. Department of Commerce
5285 Port Royal Road
Springfield, VA 22161
Price: Printed Copy $ * ; Microfiche $3.00

Page Range	Domestic Price	Page Range	Domestic Price
001–025	$ 3.50	326–350	10.00
026–050	4.00	351–375	10.50
051–075	4.50	376–400	10.75
076–100	5.00	401–425	11.00
101–125	5.50	426–450	11.75
126–150	6.00	451–475	12.00
151–175	6.75	476–500	12.50
176–200	7.50	501–525	12.75
201–225	7.75	526–550	13.00
226–250	8.00	551–575	13.50
251–275	9.00	576–600	13.75
276–300	9.25	601–up	*
301–325	9.75		

*Add $2.50 for each additional 100 page increment from 601 to 1,000 pages; add $4.50 for each additional 100 page increment over 1,000 pages.

LAWRENCE LIVERMORE LABORATORY
University of California Livermore, California 94550

UCRL-52275

SYSTEMATICS OF GAMMA DECAY THROUGH LOW-LYING VIBRATIONAL LEVELS OF EVEN-EVEN NUCLEI EXCITED BY (p,p') AND (n,n') REACTIONS

Ronald Paul Koopman

June 30, 1977

Table of Contents

ABSTRACT

A series of experiments was performed in which gamma-ray spectra were measured, using a Ge(Li) detector, for incident 7 to 26-MeV protons on the even-even vibrational nuclei ^{56}Fe, ^{62}Ni, ^{64}Zn, ^{108}Pd, ^{110}Cd, ^{114}Cd, ^{116}Cd, ^{116}Sn, ^{120}Sn, and ^{206}Pb, and for incident 14-MeV neutrons on natural Fe, Ni, Zn, Cd, Sn, and Pb. These measurements yielded gamma-ray cross sections from which it was inferred that almost all of the gamma cascades from (p,p') and (n,n') reactions passed down through the first 2^+ levels. Consequently, the strength of the $2^+ \rightarrow 0^+$ gamma transitions were found to be an indirect measure of the (p,p') or (n,n') cross sections.

Several types of nuclear model calculations were performed and compared with experimental results. These calculations included coupled-channel calculations to reproduce the direct, collective excitation of the low-lying levels, and statistical plus pre-equilibrium model calculations to reproduce the (p,p') and the (n,n') cross sections for comparison with the $2^+ \rightarrow 0^+$ gamma measurements. The agreement between calculation and experiment was generally good except at high energies, where pre-equilibrium processes dominate (i.e. around 26-MeV). Here discrepancies between calculations from the two different pre-equilibrium models and between the data and the calculations were found. Significant isospin mixing of $T_>$ into $T_<$ states was necessary in order to have the calculations match the data for the (p,p') reactions, up to about 18-MeV.

ACKNOWLEDGEMENTS

It is with great pleasure that I thank:

Dr. Frank S. Dietrich for his guidance and tireless effort in bringing this work to fruition. Much of this work represents ideas which he has passed on to me with great care. His willingness to work, to help, to teach, and to review this lengthy manuscript will always be appreciated.

Dr. Luisa F. Hansen for her help with the experiments.

Dr. Steven M. Grimes for his help with the HYBRID calculations and many informative discussions on pre-equilibrium processes.

Dr. Donald G. Gardner for his help with the STAPRE calculations.

Dr. Victor A. Madsen and Dr. Virginia R. Brown for their help with the coupled-channel calculations.

Dr. Stewart D. Bloom for his guidance and instruction in the class room.

Dr. Eugene Goldberg, Dr. John D. Anderson, and Dr. Rudolf W. Bauer, who as E-Division Leaders, provided encouragement and a hospitable atmosphere in which to work.

My wife, Sue, and daughters Caia and Marni who have accepted good-naturedly, the deprivations caused by my devotion to the academic ratrace, and who have supported me through the minor tragedies along the way.

I. Introduction

Inelastic scattering is always an important contributor to nuclear reactions and can often be the most difficult on which to obtain reliable measurements. Difficulties with (n,n') and (p,p') measurements arise because of experimental problems associated with trying to measure particle spectra down to low energies, where most of the evaporation cross section is found. Such problems as multiple scattering, slit scattering, and scattering from contaminants often make the spectra difficult to interpret. At high incident particle energies, above the nucleon separation energy, the spectra include multiple particle emission events as well as (n,n') or (p,p') events and again are hard to interpret. Reliable measured values of these cross sections are needed to compare with nuclear reaction model calculations and (particularly for incident neutrons) as nuclear data in nuclear reactor and nuclear weapons calculations. This work investigates a method whereby total (n,n') and (p,p') cross sections may be determined easily and without contamination by (p,pn), (p,2p), (n,2n), etc. events, even at high energies.

General arguments[6] based on angular momentum conservation suggest that inelastic scattering from nuclei with an even number of neutrons and an even number of protons almost always results in gamma decays which cascade down through the first excited state. Consequently, the cross section for the gamma transition from the first excited state to the ground state is nearly equal to the inelastic scattering cross section. Such an equivalence was exploited as early as 1953 by Day.[26] The original purpose of the present work was to investigate

this observation both by experiment and nuclear model calculation, and to determine its limits of validity and applicability. In addition, these measurements and their comparison with model calculations have provided some valuable insight into pre-equilibrium processes at high energies (around 26-MeV incident energy) where these processes dominate compound nuclear processes, and into isospin-conserving statistical reactions and their importance as a function of incident particle energy and target nucleus.

Both $(n,n'\gamma)$ and $(p,p'\gamma)$ reactions were investigated in this work, the former for only 14-MeV incident neutrons and the latter for 7 to 26-MeV incident protons. The $(p,p'\gamma)$ reactions were particularly convenient because of the ease with which the experiments could be done as a function of energy. In principle, the $(p,p'\gamma)$ experiments can be used to infer information about $(n,n'\gamma)$ reactions using isospin-conservation arguments and nuclear model calculations. Investigating the behavior of the $(p,p'\gamma)$ reactions as a function of energy was necessary in order that the reaction mechanism might be understood and that the limits of applicability of the technique of using gamma measurements to determine inelastic scattering cross sections might be determined.

This work was confined to spherical even-even nuclei which have the characteristic low-lying level structure shown schematically in Fig. I-1. All even-even nuclei have a 0^+ (spin, parity) ground state, and almost all have a 2^+ first excited state. The 2^+ first excited state is typically 0.5 to 1.5-MeV above the ground state and can be described as a collective, quadrupole vibration of the nucleus about a spherical equilibrium shape. This one-quadrupole-phonon vibration

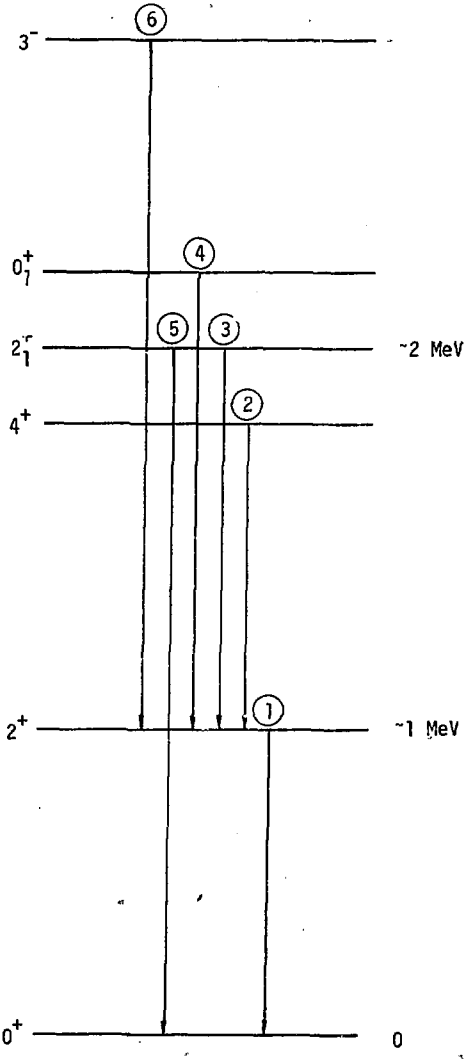

Fig. I-1. The typical low-lying level structure of a vibrational even-even nucleus with relevant gamma transitions shown. These transitions are discussed in Section III B.

carries two units of angular momentum. The next excitation is generally a two-quadrupole-phonon vibration which forms a triplet of states, with spins 0, 2, and 4, at about twice the energy of the one-quadrupole-phonon state. In actual nuclei these states are not degenerate in energy and there is no preferred ordering of the three levels. The one-octupole-phonon vibrational level is also important. It has a spin-parity of 3^- and occurs at a somewhat higher excitation energy, generally around 4-MeV. Although the structure of actual nuclei does not conform in all details to a pure vibrational model, the principal feature that is exploited in this work is the regularity of the level sequence, which allows a systematic study of the gamma cross sections over a wide range of nuclear masses.

To further introduce the ideas to be investigated in this work, the general nature of a (p,p') reaction on an even-even nucleus, as shown in Fig. I-2, will be discussed. The important feature to note about the level density is that it increases rapidly with increasing excitation energy. Level densities, at a fixed excitation energy, also increase with increasing nuclear mass and are strongly influenced by shell structure. The density of levels for magic or nearly magic nuclei is an order of magnitude smaller than for nuclei between shells at the same excitation, due primarily to the larger low energy level spacing.

It is not possible to describe highly excited states as single particle levels. Instead, many nucleons are excited and the emission spectrum becomes complex due to the many different ways the energy may be distributed among the nucleons. In this way, calculating

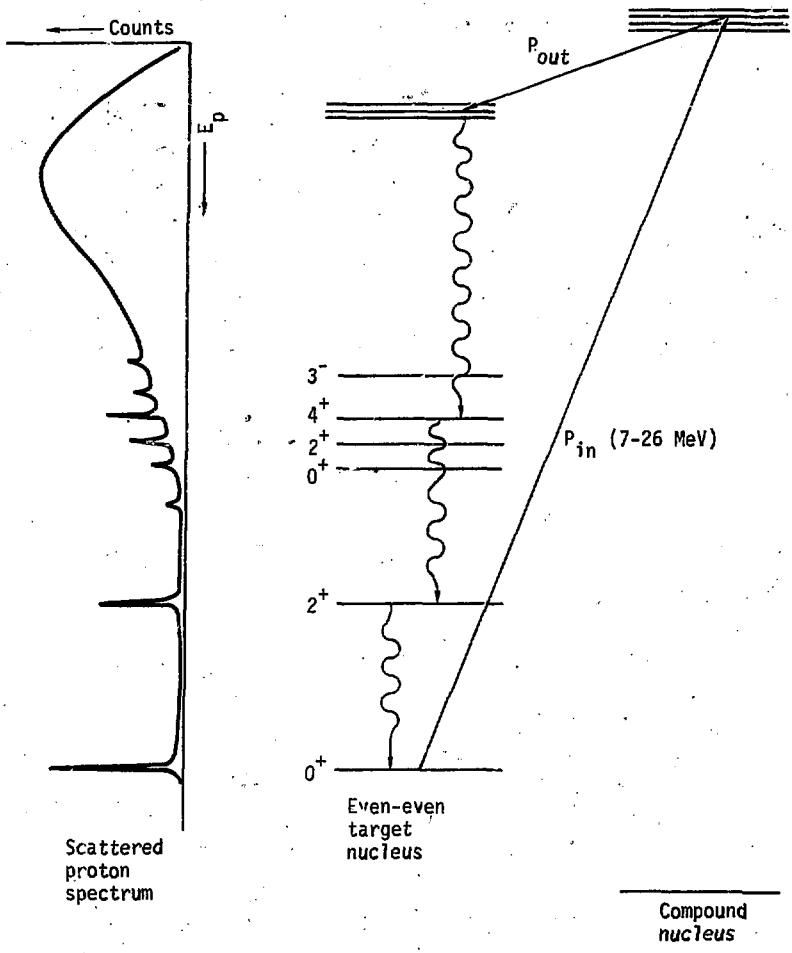

Fig. I-2. A schematic diagram of a (p,p') reaction on an even-even nucleus

nuclear level densities becomes a statistical mechanics problem and (with suitable assumptions) provides the basis for the Fermi gas model of the nucleus and the statistical model of nuclear reactions.

Since the nuclear reaction can be viewed in a statistical way, it is easy to understand why most emitted particles come out with low energy, like molecules being evaporated from a hot body. The compound nucleus will decay with highest probability to that configuration with the highest density of states, which will occur at high excitation energies for the residual nucleus. A sketch of a typical proton emission spectrum is shown in Fig. I-2. Angular momentum is also treated statistically and the spin distribution is found to peak at 3-5 units[6] in the region of closely spaced levels relevant to the present work.

After the particle decay the nucleus is usually left with a substantial amount of excitation energy. If this energy exceeds the nucleon separation energy, then a second nucleon emission will usually occur. Proton emission will, of course, be hindered by the Coulomb barrier, and alpha emission is usually very small because of this. If the excitation energy is below the nucleon separation energy (generally the neutron separation energy) then the nucleus will decay by a gamma cascade from the highly excited state down to the ground state. The nature of this cascade will depend on the excitation energy and angular momentum of the initial configuration, as well as the energies and spins of the low-lying levels. For the choice of energies and incident particles used in

this work, it is believed that the gamma decays from the region of closely spaced levels are predominantly electric dipole. If a large amount of angular momentum has been deposited in the nucleus by the incident particle, the gamma decay will preferentially feed low-lying levels with higher spins such as the 3^- and 4^+ levels. If very little angular momentum is deposited by the incident particle, the decay will favor those levels with lower spins, such as the 0_1^+, 2_1^+, 2^+, and 0^+ levels. In the high angular momentum, high incident particle energy case, the gamma cascade should nearly always pass through the first 2^+ level. At lower energies, decays to the ground state which bypass the first 2^+ level become more probable.

Also shown schematically in Fig. I-2 are peaks from high energy scattered protons corresponding to the low-lying levels in the final nucleus. These are due primarily to direct collective reactions and are reproduced by coupled-channel calculations which are discussed in Section IV-A.

To complete the description of the reaction process it is necessary to include isospin conservation and pre-equilibrium emission. The relative importance of these processes varies with incident particle energy, and the inclusion of both processes was necessary in order to reproduce and understand experimental data. Isospin-conserving reactions are particularly important for protons, with energies up to about 20-MeV, incident on relatively heavy ($A \sim 100$) nuclei. In some cases, such as for the heavier mass isotopes, isospin-conserving reactions produce essentially all of the (p,p') cross section not accounted for by pre-equilibrium reactions.

Conversely, pre-equilibrium emission becomes increasingly important as the incident particle energy increases until, by 26-MeV, it accounts for virtually all of the observed (p,p') cross section. The amount of calculated pre-equilibrium emission at any given energy is somewhat dependent on the model used.

The experimental techniques and the equipment used to determine $(p,p'\gamma)$ gamma cross sections for ^{56}Fe, ^{62}Ni, ^{64}Zn, ^{108}Pd, ^{110}Cd, ^{114}Cd, ^{116}Cd, ^{116}Sn, ^{120}Sn, and ^{206}Pb are discussed in Section II-A. Section II-B contains the discussion of the $(n,n'\gamma)$ experiments on natural Fe, Ni, Zn, Cd, Sn, and Pb. It was found necessary to employ pulsed beam and timing or coincidence techniques in order that reliable measurements of $(p,p'\gamma)$ and $(n,n'\gamma)$ cross sections might be obtained, free of ambiguities associated with beta decay, electron capture, or background-associated gamma rays with the same energies as those from the (p,p') or (n,n') events of interest.

The results of these experiments, generally in the form of gamma cross sections, are discussed in Section III. The $(p,p'\gamma)$ results are presented as a function of incident particle energy, which ranged from 7 to 26-MeV, and the $(n,n'\gamma)$ results are presented at 14-MeV. What is observed, basically, is that the $(2^+ \rightarrow 0^+)$ gamma transition does account for nearly all of the (p,p') or (n,n') cross section. Because of angular momentum conservation, however, this near-equality tends to break down at low incident energies when very little angular momentum is brought into the nucleus and direct decay to the 0^+ ground state, bypassing the 2^+ first excited state, becomes more favored.

Section IV contains the computer model calculations. First, the coupled-channel calculations of the direct collective excitation of the low-lying states in the final nucleus are discussed. The excitations of the vibrational levels of these nuclei are very significant, accounting for up to 50% of the observed ($2^+ \rightarrow 0^+$) gamma cross section. Next, the statistical plus pre-equilibrium model calculations are discussed and compared with experimental data both from this work and from the work of others. These calculations were done essentially in two parts. First, calculations using the HYBRID code, which combines the simple Weisskopf evaporation model[41] (which does not include angular momentum) with the pre-equilibrium formulation due to Blann[40] and Grimes,[42,48] were performed for almost all of the nuclei investigated experimentally, as a function of incident proton energy and for neutron energies near 14-MeV. These calculations reproduced the data reasonably well and clearly showed how important isospin-conserving and pre-equilibrium reactions are in reproducing experimental observations. They also verified the near equality of the (p,p') and (n,n') cross sections with the ($2^+ \rightarrow 0^+$) gamma cross section. Second, calculations using the STAPRE[68] code, which consists of the Hauser-Feshbach[65] statistical model (which includes angular momentum), the pre-equilibrium formalism due to Cline and Blann,[46] and gamma-ray strength functions described by the Brink-Axel[69] model, were performed for incident protons on ^{62}Ni and neutrons on ^{56}Fe. These calculations produced details of the gamma cascade and ($2^+ \rightarrow 0^+$) cross sections which were not obtainable from the HYBRID calculations.

Cross sections for both the particle emission and the gamma transitions were calculated and they agreed quite well with the corresponding measured values. Again, the near-equality between the $(2^+ \rightarrow 0^+)$ gamma cross section and the (n,n') or (p,p') cross section was demonstrated, but with this calculation the change in the relationship with incident particle energy could be inferred. Further conclusions, based on comparison of these calculations with experimental data, are presented in Section V along with recommendations for further experiments.

II. Experimental Methods

The purpose of the experiments was to measure the gamma-ray spectra from the inelastic scattering of both protons and neutrons by a series of even-even target nuclei. The experiments focused on the gamma-rays from the low-lying vibration-like levels in these nuclei, where energies, spins, and parities were generally known. The gamma-rays of interest had energies between 200-keV and 3-MeV.

A. The $(p,p'\gamma)$ Experiments

A.1. The Apparatus

The experiments were performed at the Livermore cyclograaff facility.[2] This is a two-part accelerator consisting of a 76-cm, fixed energy cyclotron and a 6 MV, variable energy, tandem Van de Graaff. The cyclotron produces 14.8-MeV negatively charged hydrogen ions. The Van de Graaff can be used by itself to accelerate protons to energies up to 12-MeV, or it can be used with cyclotron injection to produce proton beams with energies up to 27-MeV. This is a very versatile system, but does leave a gap between about 12 and 15-MeV which cannot be reached by either machine. The 25 MHz pulse rate of the cyclotron was reduced with an external sweeper which eliminated 6 out of 7 beam pulses before injection into the tandem. A schematic drawing of the facility and the experimental setup is shown in Figs. II-1 and II-2.

Data were taken at a series of proton energies, generally beginning at 7.5-MeV (9-MeV for the heavier elements) and moving up in steps of about 2-MeV to 26-MeV. For proton energies between 7.5 and 12-MeV, the tandem alone was used. For the data at 14.8-MeV, the cyclotron alone was used and the beam was drifted through the tandem

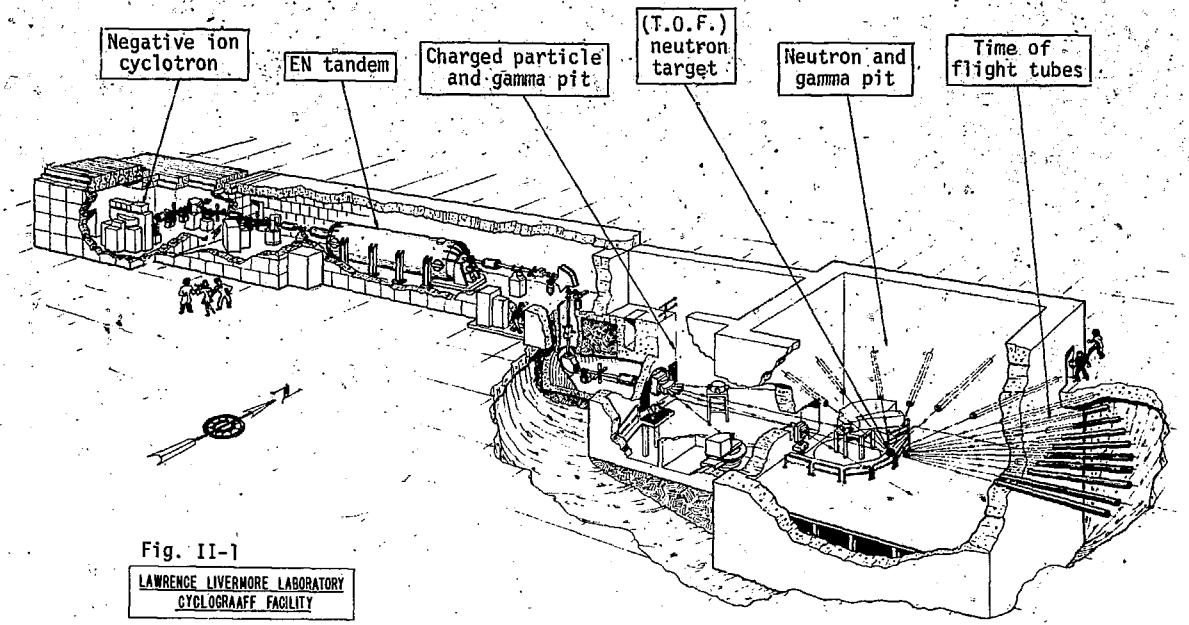

Fig. II-1

LAWRENCE LIVERMORE LABORATORY
CYCLOGRAAFF FACILITY

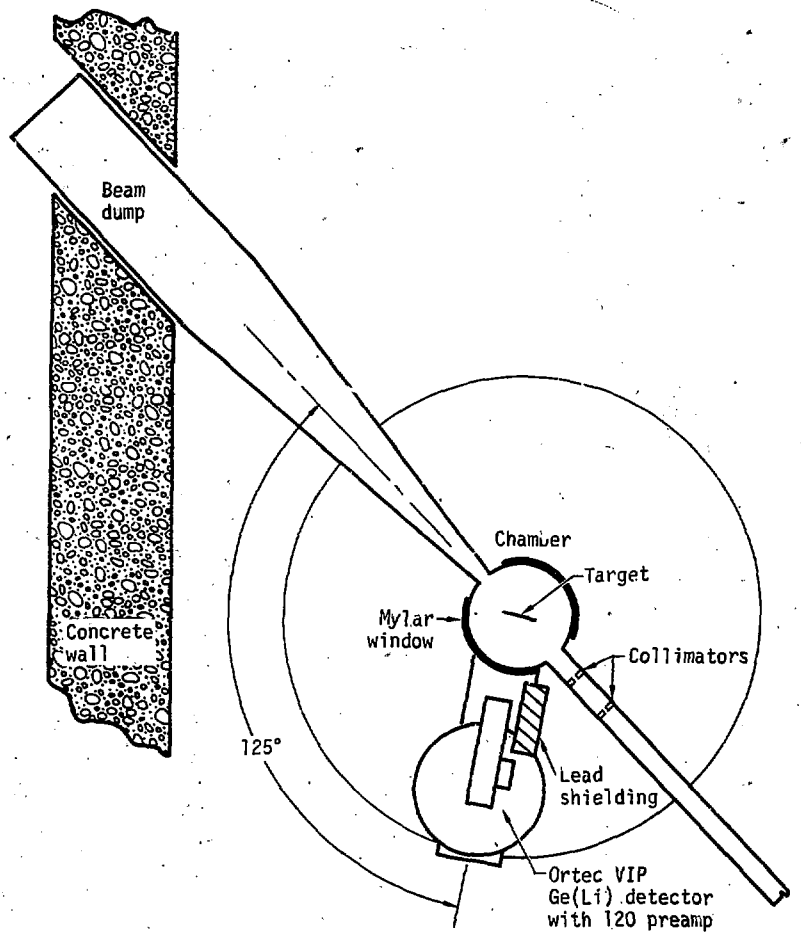

Fig. II-2. The top view of the experimental setup for Ge(Li) detector gamma spectroscopy at the LLL Cylo-Graaff facility.

with the terminal shorted to ground. For energies between 16 and 26-MeV, the combination of fixed energy cyclotron and variable energy tandem was used. Beam currents were typically between 25 and 100 nA with runs taking from 20 to 30 minutes.

The proton beam emerging from the tandem was momentum analyzed and bent down into the underground experiment pit. It was then focused through two collimators (generally 3/16 and 3/32 inches in diameter) onto the target. Thin self-supporting targets (about 2 mg/cm^2) were used, and the transmitted beam was collected in an electrically isolated beam dump. It is believed that this integrated current can be measured with an accuracy of better than 3%.

An Ortec VIP series Ge(Li) detector was used to detect gamma-rays. These detectors have an active volume of about 55 cc and a resolution of about 2.2 keV for ^{60}Co γ-rays. The detector was oriented at 125° with respect to the beam direction. Gamma angular distributions may be described by a series of even Legendre polynomials and this angle corresponds to a zero for the $\ell = 2$ polynomial, P_2, which describes most of the anisotropy of the angular distribution. The P_4 term is generally small and somewhat uncertain. Ignoring the P_4 term will introduce an error of between 3 and 9% in the case of ^{56}Fe(n,n'γ) at 14-MeV[28] and about 1% for ^{206}Pb(n,n'γ) at 4-MeV.[29] These values are thought to be typical of the other nuclei as well. More will be said about angular distributions in Section III.

It must be kept firmly in mind that the (p,p'γ) measurements were made only at 125° and actually represent differential cross

sections. They can, with only a few percent error, be multiplied by 4π and considered to be angle-integrated cross sections, however.

The detector viewed the target through a mylar window on the target chamber. It was shielded from background radiation, which came principally from collimators in the beam line, by several inches of lead in the form of an annulus around the detector and lead bricks between the detector and the collimators. For some targets the target itself was the source of excessive amounts of x-rays. This low energy radiation was reduced to acceptable levels by putting a 0.1-cm thick copper absorber between the target and the detector.

The Ge(Li) detectors are single crystals of germanium with lithium drifted into them to compensate for impurities. It is necessary to keep the crystal at liquid nitrogen temperature to avoid thermal excitation, with its resultant noise, and to keep the lithium immobile within the crystal. A high voltage is applied across the crystal, which causes it to act like a large diode. Gamma rays interacting with the germanium atoms create electron-hole pairs which are swept out by the applied electric field. The charge collected is proportional to the energy deposited in the crystal by the gamma-ray.

Gamma-rays with energies between 200-keV and 3-MeV were of interest in these experiments. At the end of each experiment, the detector was left in place and the targets replaced by several calibrated gamma-ray sources to determine the detector efficiency. Figure II-3 is a typical efficiency determination for [illegible] of the runs. Cross sections for the $(p,p'\gamma)$ experiments were calculated as follows. The reaction rate in the target in the region between x and x + dx is

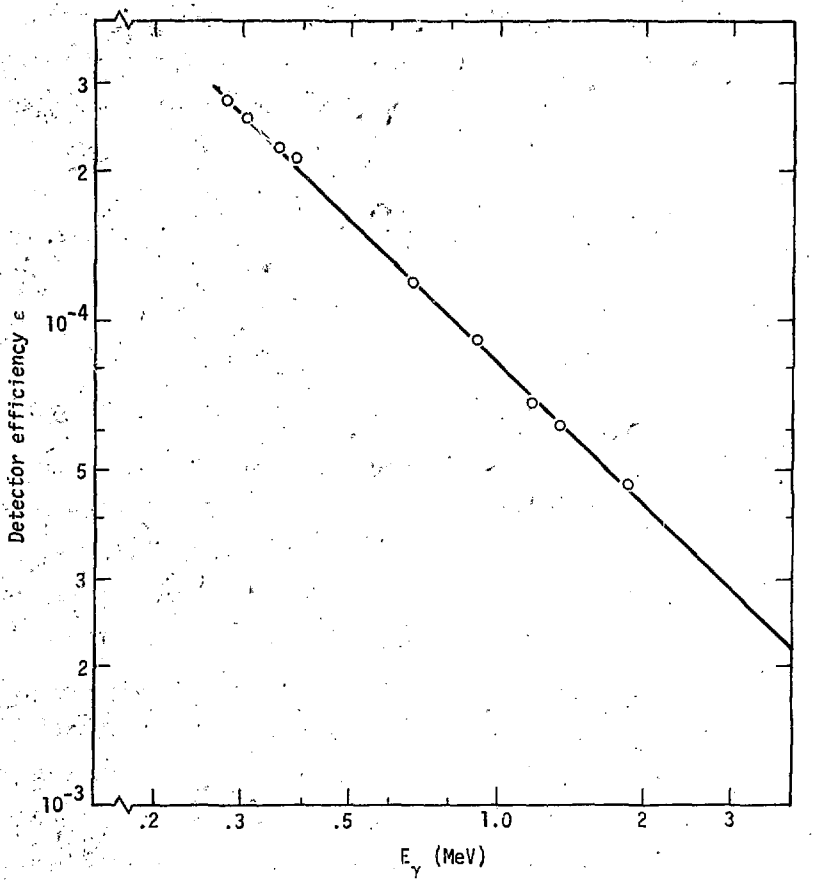

Fig. II-3. The efficiency calibration for the 55cc Ge(Li) detector at 13.25 inches from the target.

$$dR_p(x) = \sigma I N \, dx,$$

where

x = distance into target,

σ = cross section,

I = beam current (protons/second),

N = nuclei/cm^3 = $\frac{N_A \rho}{M} \chi$,

$N_A = 6.02 \times 10^{23}$, ρ = density, M = mol. wt.,

and χ = isotopic abundance.

If we assume a thin target, with I and energy constant, then

$$R_p(x) = \sigma I N t,$$

where

t = target thickness.

Gamma-ray photo-peak areas were measured. These can be related to the reaction rate for incident protons by the expression

$$R_p = \frac{eAI}{\varepsilon f Q},$$

where

$e = 1.602 \times 10^{-19}$ Coulomb,

ε = measured detector efficiency,

f = measured live fraction for the electronics,

Q = charge collected (Coulombs),

and A = γ-ray photo-peak area (number of counts).

The live fraction for the electronics, referred to above, is that fraction of the time the electronics were available to process a pulse, i.e.

f = 1 - dead time.

The dead time is roughly proportional to count rate in the system. The TAC (Time-to-Amplitude Coverter) and the MCA (Multi-Channel Analyzer) both

contributed to the system dead time, but the MCA was the dominant contributor. The live fraction, and the timing gate width, were determined for each experiment using a pulser pulse at the high energy end of the spectrum. The pulser output was scaled, and the number of pulses getting into the spectrum was counted. Runs were made at very low count rates to define the zero dead time condition and the timing gate widths. Actual runs were compared with these to determine the live fraction, which was generally about 80%.

Combining the above equations, the total cross section can be expressed as

$$\sigma = \frac{eA}{\varepsilon f Q N t}$$

A.2. The Electronics

Figure II-4 is a schematic diagram of the electronics used in these experiments. The power supply for the Ortec 120 preamplifier and the high voltage power supply for the Ge(Li) detector were located in the experimental pit and isolated from line noise by an isolation transformer. This substantially improved the resolution upstairs in the control room where the preamp signal was amplified by an Ortec 451 spectroscopy amplifier.

The accelerator was run in the pulsed beam mode with the beam bunched to a width of about 2 ns and with a repetition rate of 2.5 MHz for the tandem alone and 3.57 MHz for the cyclograaff. The principal reason for doing the timing was to eliminate the background events due to (p,n) reactions in the target and the subsequent beta decay back to excited states in the nucleus of interest. This was initially a substantial problem with some of the nuclei.

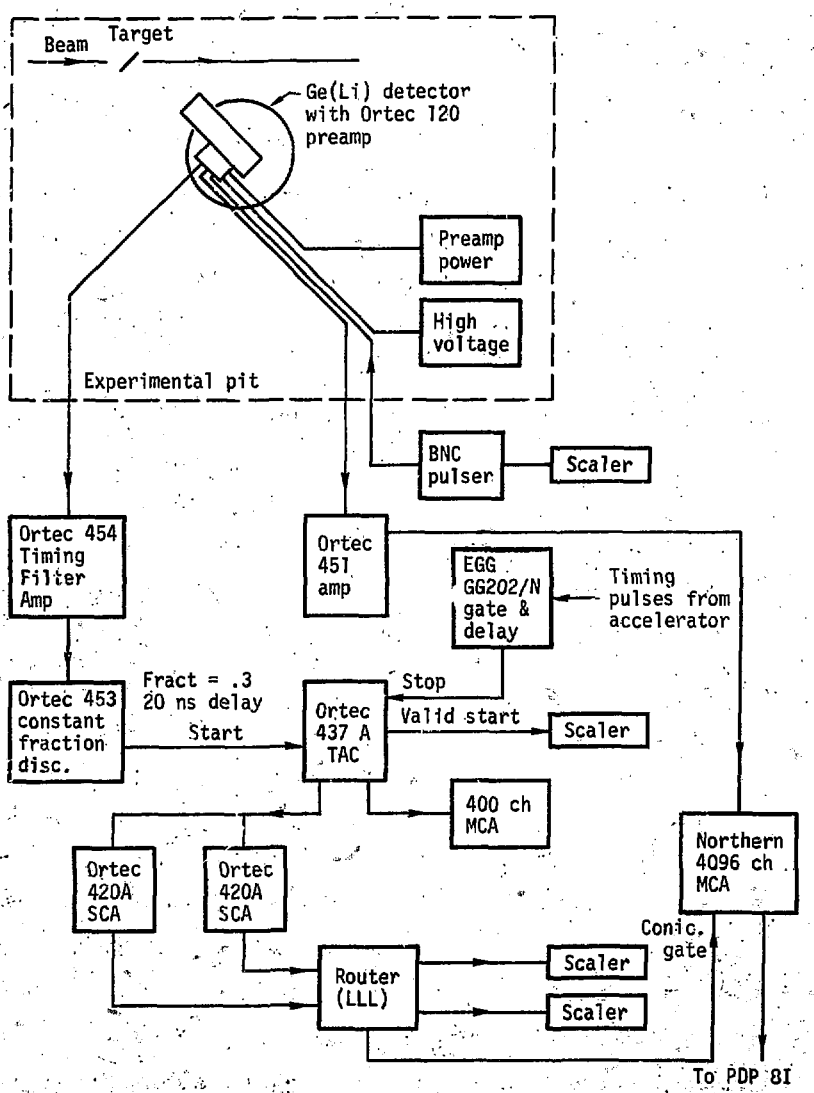

Fig. II-4. The electronics for both the $(p,p'\gamma)$ and the $(n,n'\gamma)$ experiments

Timing pulses corresponding to beam bursts were taken from the RF and used to generate stop pulses for an Ortec 437A TAC. The start signals came from the Ge(Li) detector. One output from the preamplifier was run through an Ortec 454 Timing Filter Amplifier and then into an Ortec 453 Constant Fraction discriminator. Getting reliable timing over a wide dynamic range with the Ge(Li) detectors was a difficult problem. Several different timing units were tried, including Ortec 463 and 453 Constant Fraction units and a Canberra EZS (Extrapolated Zero Strobe). The 463 and the EZS did not give the dynamic range needed while the 453 was difficult to set up but did provide the required dynamic range. The signal from the 453 was used to start the TAC. A typical spectrum from the TAC is shown in Fig. II-5. Two Ortec 420A SCA's (Single Channel Analyzers) were used to define gates on the TAC spectrum. One gate was set over the prompt peak, that is, over the events occurring immediately after the beam burst strikes the target. The other gate was set on the flat background region. This corresponds to events which are out of time with the beam bursts. Each gate was approximately 25 ns wide and the TAC peak itself had a FWHM (Full Width at Half Maximum) of about 5 ns. The TAC output was displayed on a small MCA and checked after each energy change so that the TAC peak could be kept within the SCA gate. The output from the SCAs went to an LLL-designed router which was used to gate a Northern 4096 channel multichannel analyzer. We accumulated two 2048 channel spectra in the MCA, one corresponding to events which fell within the prompt gate and the other to events which fell within the out-of-time or random gate. Since the prompt gate also contains a random contribution, the spectrum corresponding to the random events was normalized for different gate widths and subtracted from

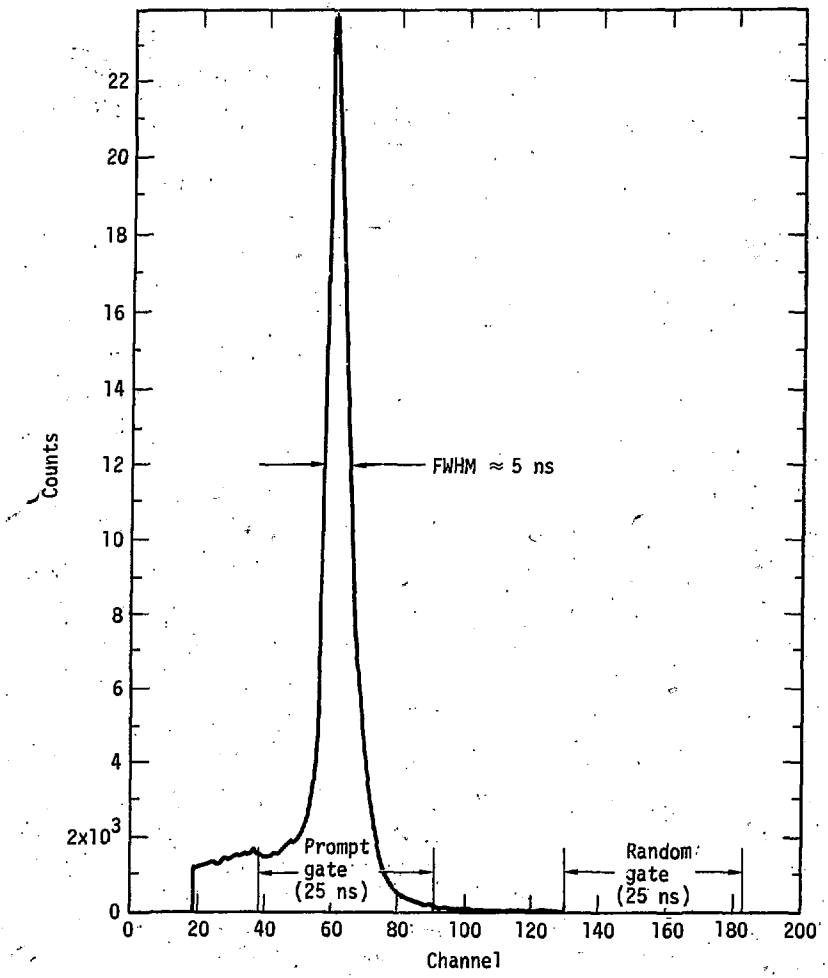

Fig. II-5. The $^{56}Fe(p,p'\gamma)$ TAC spectrum (0.5 ns/channel).

the prompt data, leaving only those counts which corresponded to beam burst coincident events. The normalization was accomplished with a Berkeley Nucleonics Corp. BHI pulser. The pulse shape from this pulser was set to match, as closely as possible, the signals from the Ge(Li) detector. The amplitude was set such that pulses went into about channel 2000 in the MCA. Since the pulser output was uncorrelated with the beam, counting the pulses in the prompt and delayed spectra was an indirect measurement of the gate width. The pulser output was scaled so that the number of pulses attempting to enter the system was known. Very low count rate runs were made by stopping the beam before it passed through the target and far away from the experiment. These runs were used to define the "zero dead time" conditions. The experimental dead time was determined from the ratio of pulser counts during the experiment to those corresponding to "zero dead time". The count rate in the Ge(Li) system was generally about 10 kHz and the dead time was less than 20%.

A.3. Targets

The targets were self-supporting metallic foils with thicknesses of about 2 mg/cm^2 except for the Sn and Pb targets, which were about 5 mg/cm^2. Target thicknesses were determined by weighing foils with known areas and by measuring the energy losses of 5-MeV alphas from ^{241}Am. The results of these two measurements were generally in good agreement.

A general series of even-even isotopes with the essential simple vibration-like low-lying level structure was chosen for examination. Nuclei were needed whose low-lying level structures were known and which had a 0^+ ground state and a 2^+ first excited state. We chose ^{56}Fe, ^{62}Ni, ^{64}Zn, ^{108}Pd, ^{110}Cd, ^{114}Cd, ^{116}Cd, ^{116}Sn, ^{120}Sn, and ^{206}Pb as nuclei which satisfied

these criteria and were available as isotopically separated targets. All the targets had isotopic purities of more than 95%; most were nearly 99%. There are many other nuclei which satisfy our criteria, but the ones chosen allowed us to look at the gamma decay over a range of nuclear masses and over a range of isotopic masses for individual elements. This is important because neutron emission becomes more favored as the isotopic mass increases. According to Cohen et al.,[1] the inelastic protor scattering from the heavier, more neutron rich isotopes will be almost entirely direct, since almost all compound nuclear events will decay by neutron emission. The lighter, less neutron rich isotopes will undergo a combination of compound and direct processes. These arguments neglect isospin considerations and pre-equilibrium processes. The level structure of the low-lying levels in the nuclei of interest is summarized in Fig. II-6.[25]

B. The (n,n'γ) Experiments

B.1. The Apparatus

These experiments were performed at the Livermore ICT (Insulated-Core Transformer) neutron generator. This is a 400 kV dc, high current machine used to accelerate a deuteron beam onto a solid tritium-titanium target, producing copious quantities of D-T fusion neutrons. Schematic drawings of the facility and our experimental setup are shown in Figs. II-7 and II-8. The deuteron beam was bunched to a width of 4.5 ns with a repetition rate of 500 kHz and a beam current of about 6.5 μA.

Neutron production was determined by counting alpha particles from the $^{3}H(d,n)^{4}He$ reaction with a silicon surface-barrier detector viewing the target at a backward angle (174°) about 13 inches away. The alpha spectrum was viewed on a MCA, and a single channel analyzer

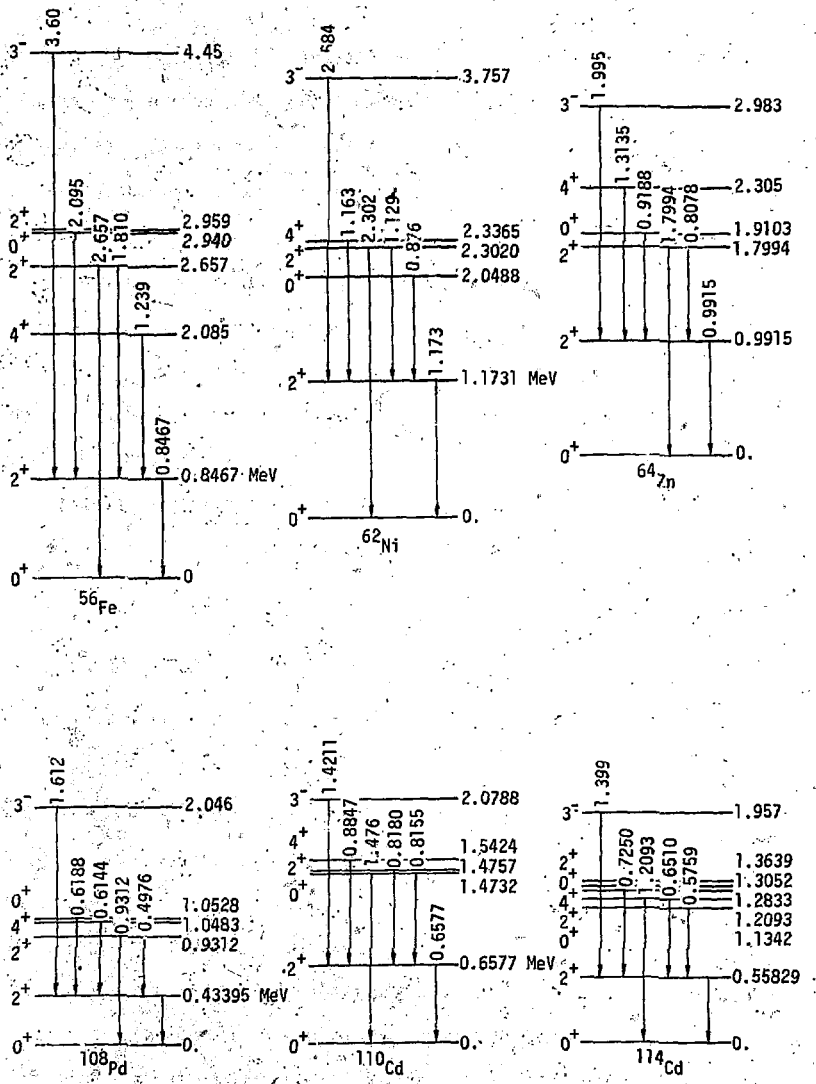

Fig. II-6. The nuclear level structure of the nuclei studied in the (p,p') experiments.

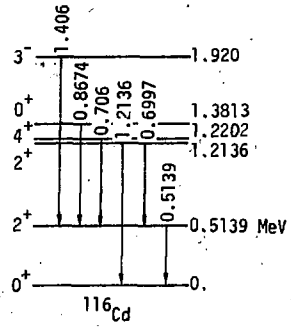

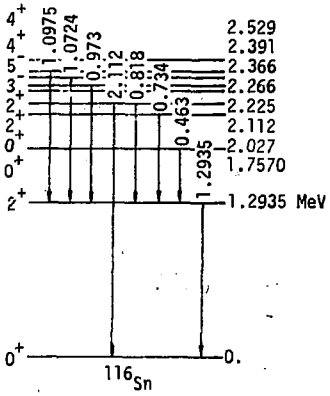

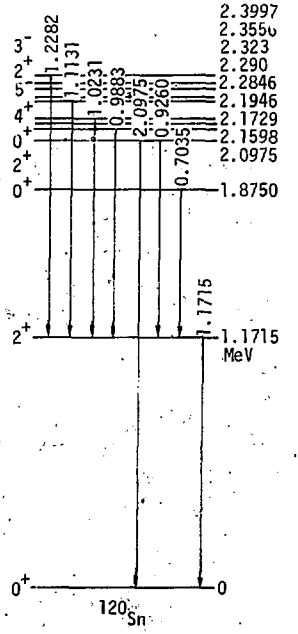

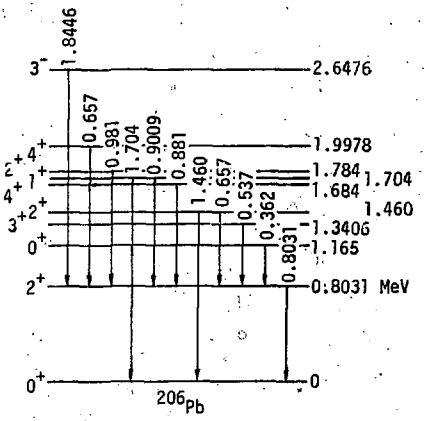

Fig. II-6 Continued

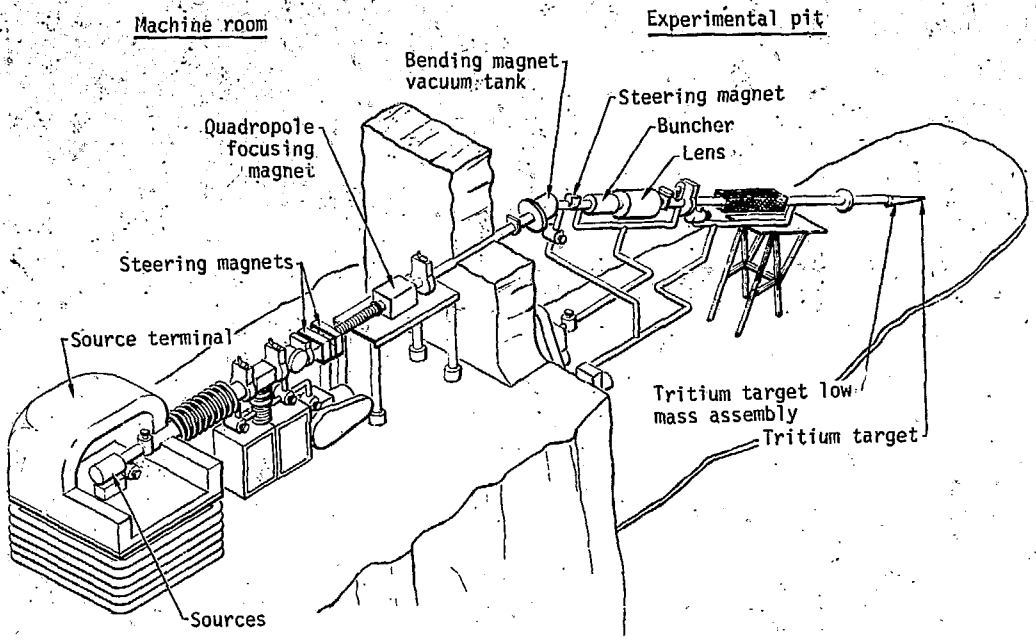

Fig. II-7 The Livermore ICT facility with the low mass assembly in place.

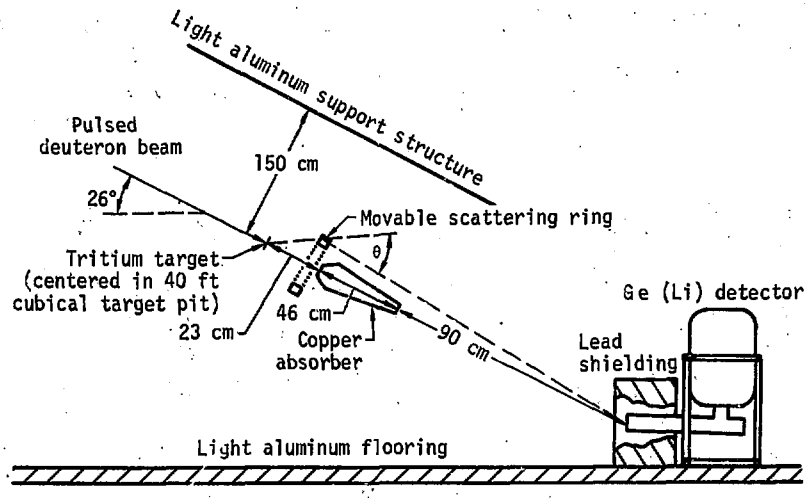

Fig. II-8. The experimental arrangement for Ge(Li) detector gamma spectroscopy at the Livermore ICT facility.

window was set up on the alpha peak. The events falling within this window were scaled and, after calibration, were used to determine neutron production. The absolute neutron source strength was determined using a proton-recoil detector, with an efficiency known to about ± 5%, temporarily set up at about 100 cm from the target. The count rate in the alpha counter was then compared with this detector. The neutron production rate was typically 10^9 sec^{-1}.

An older Nuclear Diodes 35 cc Ge(Li) detector, with a resolution of about 3.2-keV for the ^{60}Co lines and an efficiency about two thirds that of the Ortec VIP detectors, was used for the neutron experiments. The detector was placed on a piece of plywood on the thin aluminum floor and lead brick shielding was stacked around it to try to reduce the rather high background from room-scattered neutrons and activation. A large copper slug, 46 cm long, was placed between the tritium target and the Ge(Li) detector to shield it from radiation coming directly from the source (see Fig. II-8).

The scattering rings were mounted with their axes along the line from target to detector with the target close to the center of the ring and the copper slug close to the target. The energies of the neutrons emitted from the target vary with the angle θ in the manner shown in Fig. II-9. Changing the ring angle θ (see Fig. II-8) from 55° to 125° changed the incident neutron energy from 13.6-MeV to 14.8-MeV. The neutron source intensity also varies with angle as is shown in Fig. II-10. As with the $(p,p'\gamma)$ experiments, these measurements are differential cross sections at a particular angle. Unlike the $(p,p'\gamma)$ experiments, however, the $(n,n'\gamma)$ measurements were generally made at several angles. They are in substantial agreement with published data.[28,29,30,31,32]

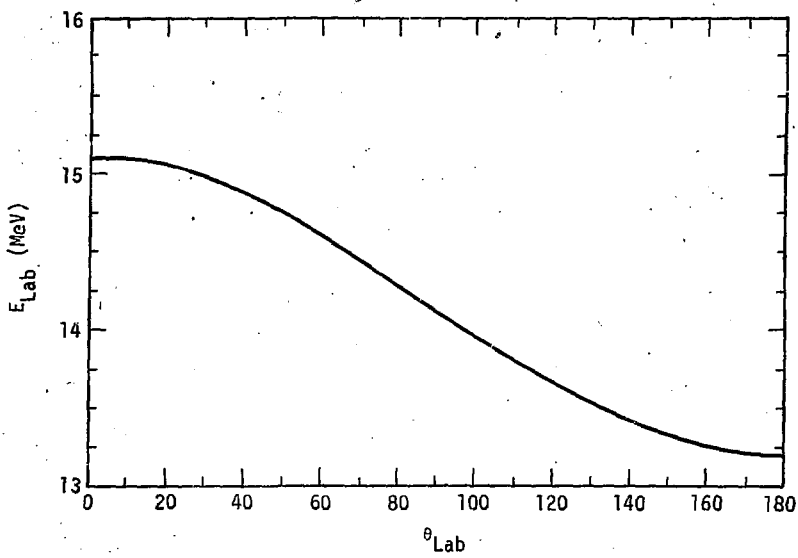

Fig. II-9. Variation of the most probable energy with angle of the $T(d,n)^4He$ source neutrons.

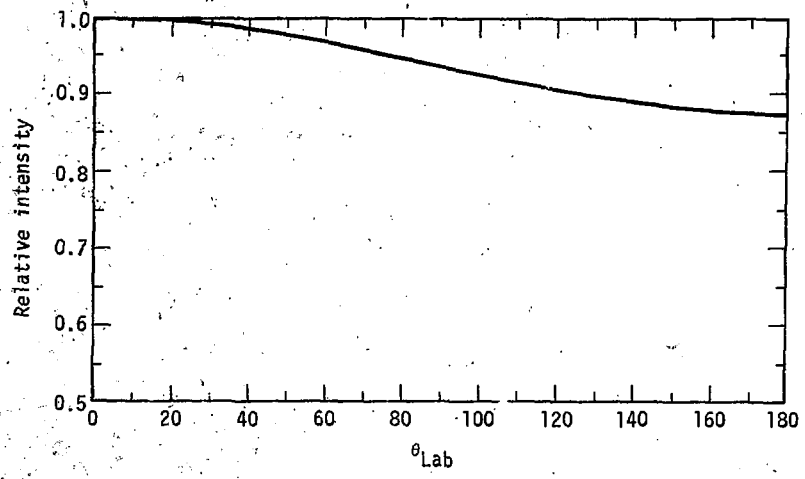

Fig. II-10. Calculated angular distribution of the source neutrons. The most probable reaction energy was 200 keV.

At the end of the experiment, several calibrated gamma-ray sources were placed on one of the rings and counted overnight to determine detector efficiency. Background contributions to the standard lines were so strong that this method failed and the efficiency calibration had to be repeated later.

B.2. The Electronics

The electronics setup was essentially the same as shown in Fig. II-4, including an Ortec 120 preamp for the Ge(Li) detector. A minor difference was that the timing filter amplifier and pulser were left in the experimental pit to minimize noise pickup during the long transmission of low level signals.

The accelerator beam was pulsed, and timing signals were taken from a capacitive time pickoff near the target and used to stop the TAC. Start signals came from the Ge(Li) as in the (p,p') work. The timing was doubly necessary in this case, both to eliminate the beta decay contribution and to reduce the very high background contribution from neutron activation in the experimental pit. Without the timing we could not have obtained reliable data. Figure II-11a is the output of the TAC with the ring in place. The first peak is due to gamma rays from neutron interactions in the ring, and the larger second peak is due to room and equipment-scattered neutrons and gamma rays produced by these neutrons. Short runs with the ring in and out were done, and the first peak was not present when the ring was not there, as can be seen in Fig. II-11b. Single channel analyzer gates were set on the prompt, ring-associated first peak and on the flat, delayed, or random background region. The gates were each about 50 ns wide and were used to gate the MCA to take two simultaneous 2048 channel gamma-ray spectra in exactly the same way as was done in the $(p,p'\gamma)$ experiments.

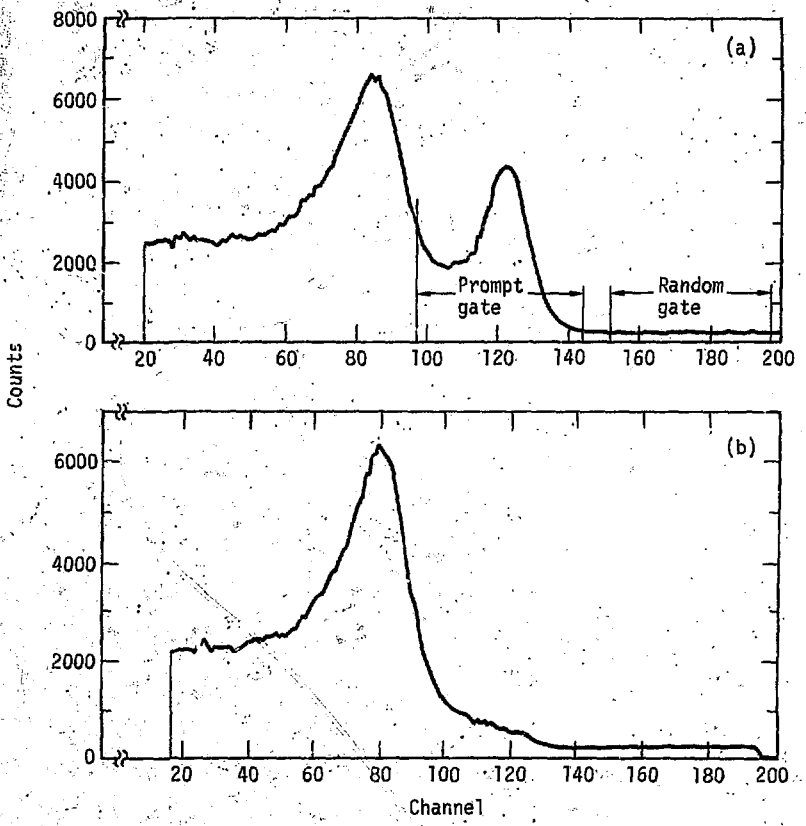

Fig. II-11. The $^{56}Fe(n,n'\gamma)$ TAC spectra
a. With the ring in place
b. Without the ring.

Count rates in the Ge(Li) system were generally about 5 kHz with an associated dead time of about 10%. The runs generally took two to three hours and were done with the rings in three different positions which corresponded to neutron energies of about 13.5, 14.3 and 14.8 MeV, and angles of about 125°, 30°, and 50°.

B.3. Targets and Cross Section Calculation

The targets for the neutron experiments were large rings of the elements, in metallic form and their naturally occurring isotopic abundance. Table II-1 is a summary of the rings used, including the weight, size, and isotopic abundances. Cross sections for the $(n,n'\gamma)$ experiments were calculated as follows. Consider the geometry shown in Fig. II-12. The interaction rate of the source neutrons in the volume element dv is

$$dRn = \frac{S_0}{4\pi r^2} e^{-\sigma_T N(r-r_1)} \sigma N \chi dv,$$

where $e^{-\sigma_T N(r-r_1)}$ describes the source attenuation by the ring, and where

χ = isotopic abundance of isotope of interest,

r_1 = distance to ring surface,

r = distance to volume element dv,

S_0 = source strength,

σ_T = total cross section,

σ = cross section for reaction of interest,

and N = nuclei per unit volume.

Table II-1 Ring Targets for $(n,n'\gamma)$ Experiments

	Outside Diameter (cm)	Inside Diameter (cm)	t Thickness (cm)	w Weight (gm)	σ_T (barn)	$\sigma(n,n'\gamma)$ meas. (barn)	$\frac{\sigma_{true}}{\sigma_{meas.}}$	Isotopic Abundance
Fe	24.0	20.0	0.98	1074	2.5	0.69	0.90	56-91.7%
Ni	22.5	20.0	1.26	921	2.6	0.43	0.98	58-68.3% 60-26.1% 62-3.6%
Zn	24.0	20.0	1.00	978	2.9	0.69	0.93	64-48.9% 66-27.8%
Cd	24.0	20.0	1.00	1204	4.5	1.16	0.92	110-12.4% 112-24.0% 114-28.8% 116-7.6%
Sn	24.0	20.0	1.00	1010	4.6	0.81	0.94	116-14.4% 118-24.1% 120-32.8%
Pb	22.82	17.74	1.28	2324	5.5	0.66	0.81	206-24.1% 208-52.4%

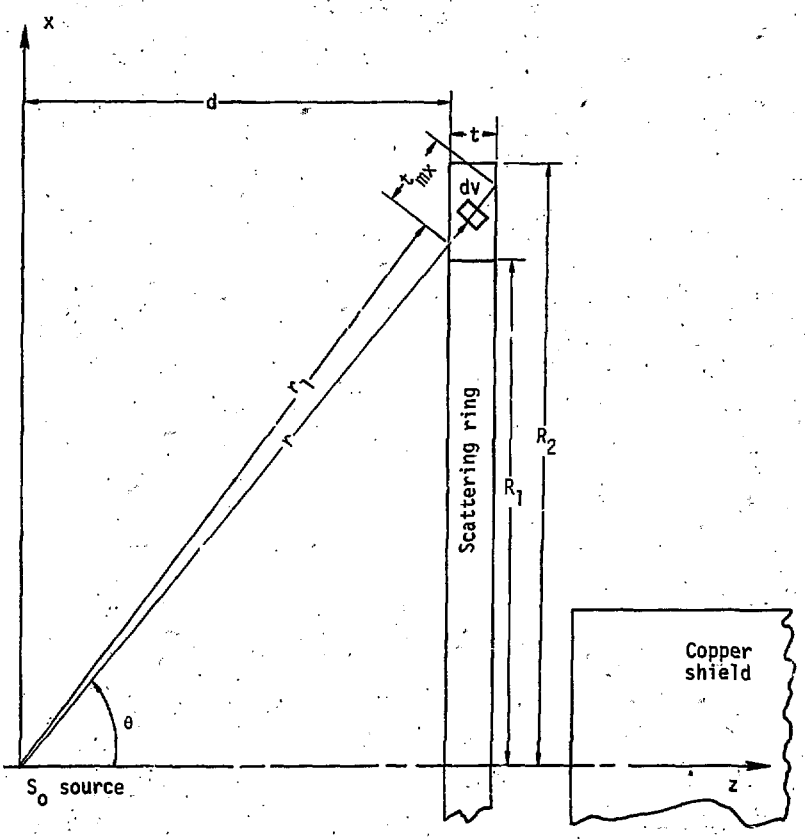

Fig. II-12. The ring geometry used for the (n,n'γ) experiments.

An exact analytical evaluation of the integral of this expression is difficult. Since the ring's cross sectional dimensions are relatively small compared to the source-to-ring distance, it is reasonable to make certain helpful assumptions. First, it is assumed that the source to ring distance is constant, i.e. that

$$\frac{1}{r^2} \simeq \frac{1}{\langle r \rangle^2}$$

where <r> is the distance from the source to the center of the ring's cross-sectional area. The reaction rate will then be

$$R_n = \frac{S_0}{4\pi\langle r \rangle^2} \int_v e^{-\sigma_T N(r-r_1)} \sigma N \chi dv,$$

$$\text{or } R_n = \frac{S_0}{4\pi\langle r \rangle^2} \frac{\chi\sigma v}{t_{eff}\sigma_T} (1 - e^{-\sigma_T N t_{eff}}),$$

where t_{eff} equals the path length through the ring. For small $\sigma_T N t_{eff}$, $e^{-\sigma_T N t_{eff}} \approx 1-\sigma_T N t_{eff}$; e.g. $\sigma_T N t_{eff} = 0.2$ for the more or less typical Zn ring. The reaction rate then becomes

$$R_n = \frac{S_0}{4\pi\langle r \rangle^2} \sigma N V \chi$$

Next, consider gamma-ray production in the ring and detection in the Ge(Li) detector, correcting for gamma-ray self absorption in the ring. We assume that the gamma production occurs uniformly throughout the ring. The rate of detection of gamma-rays in the Ge(Li) detector is

$$R_\gamma = R_n \varepsilon \int_0^t \frac{dx}{t} e^{-\mu x},$$

where

μ = γ-ray attenuation coefficient

and ε = Ge(Li) detector efficiency.

Then

$$R_\gamma = \frac{S_0 V \varepsilon \chi}{4\pi \langle r \rangle^2 \mu t} \sigma N (1 - e^{-\mu t})$$

and

$$\sigma = \frac{4\pi \langle r \rangle^2 R_\gamma}{S_0 V \varepsilon N \chi} \left[\frac{\mu t}{(1 - e^{-\mu t})} \right]$$

The cross sections for (n,n'γ) events were calculated from this expression, with multiple scattering corrections applied later. Multiple scattering contributions due to neutrons scattered from the copper shadow bar back into the ring were calculated (see Appendix I) and account for 3%, at most, of the neutrons interacting in the ring. Their contribution is probably less than this because of our timing requirements. The scattered neutrons would be delayed and produce gammas which would fall outside our prompt time window. Monte Carlo calculations with the copper shield in and out indicate that its effect, without the timing requirement, is of the order of 3%, supporting the analytical calculation.

Multiple scattering in the ring itself is a more difficult problem. Day[26] demonstrated experimentally that a multiple scattering contribution exists even for relatively small rings and becomes increasingly important with increasing ring size. He did Monte Carlo calculations and found that, in general, multiple scattering and neutron attenuation balanced each other. He found that neglecting both produced results which differed by only 3.5% from those results which had been corrected

for both phenomena. These were low energy neutrons, however, well below the (n,2n) threshold. Kammerdiener[24] investigated multiple scattering for 14-MeV incident neutrons on rings in a geometry identical to ours (indeed, some of the rings were the same) and found the effect to be small. He measured (n,n') cross sections and used a Monte Carlo code, iteratively, to correct the data.

The TART[27] Monte Carlo code was used for calculations with a geometry which exactly reproduced the important aspects of the experimental geometry. It was found that the effects were indeed small but not ignorable. After the (n,2n) threshold is crossed, at about 10-MeV, the multiple scattering is no longer balanced by the attenuation. Table II-1 gives the ratio of "true"-to-measured (n,n') cross sections and it can be seen that the net correction is generally less than 10% except for Pb where it is 19%. The measured cross section, $\sigma_{meas.}$, is the sum of the $2^+ \rightarrow 0^+$ gamma transition cross sections for the major isotopic constituants of the rings, at 14 MeV. The "true" cross section, σ_{true}, comes from the Monte Carlo calculation in the following way

$$\sigma_{true} = \frac{S_o \sigma_{meas.} - \sum_{i}^{i<14} \sum_{k} S_{k,i} \sigma_i(2^+)}{\sum_{k} S_{k,14}} ,$$

where

S_o = mean path length in the ring with no interactions,

$\sum_k S_{k,i}$ = neutron path length in the ring, at energy i, summed over k contributions.

and $\sigma_i(2^+)$ = cross section for $2^+ \rightarrow 0^+$ gamma produotion at neutron energy i.

The measured cross section, $\sigma_{meas.}$, was subsequently multiplied by the ratio, $\sigma_{true}/\sigma_{meas}$, which corrected for multiple scattering events from reactions induced by lower energy neutrons from (n,n'), (n,2n), and (n,np) events.

III. Data Analysis and Results

A. The Data Analysis Computer Programs

The data were taken in a Northern Scientific 4096 channel multichannel analyzer, examined at the end of each run, and dumped onto small DEC magnetic tapes through a PDP-8I computer. The data was then transferred to large magnetic tapes and printed and plotted via a CDC-6600 time-sharing computer system. Data analysis was performed on a PDP-15 computer system with a 32 K memory, a scope and light pen, and a Versatac printer-plotter. This proved to be a very versatile and useful system although a bit slow for some of the more involved calculations.

The data analysis was done almost entirely with a program called GRASP which originated at Stanford and has been altered for our use. It is based on a nonlinear least-squares algorithm called CURFIT by P. R. Bevington,[3] which uses the Marquardt method.[4] The program will fit a selected region of experimental data with up to four superimposed Gaussian line shapes plus a background polynomial of up to second order. It is designed to allow the operator maximum control of and interaction with the data being analyzed. It is designed for finding and analyzing particular peaks in a spectrum consisting of many peaks, most of which are not of interest. The program is divided into three main loops, the I/O or input/output loop, the PEAK loop where peak and background regions are defined, and the FIT loop where the actual fitting is done.

In the I/O loop, data are read into the computer and the asychronous background spectrum is multiplied by a previously determined normalization constant and subtracted from the prompt spectrum, with care being

taken to calculate the correct standard deviation for each data point. The operator can then input previously determined parameters which describe peak width variation as a function of channel number, energy variation as a function of channel number, detector efficiency variation as a function of gamma-ray energy, and a target parameter which includes target thickness, molecular weight, integrated beam current, and instrumental live time.

In the PEAK loop the data is examined on the scope and, using a light pen, the peak region and the stable background regions on each side of it are chosen. Estimates for the locations of the peak centroids are also marked with the light pen. The user has the additional option of entering particular values for any of the peak parameters and fixing them so that they are not varied in the fitting process.

The user then goes on to the FIT loop and fits a polynomial through the two stable background regions on either side of the peak region. This determines the background under the peak region which will be subtracted to yield peak areas. From one to four Gaussian functions are then fit to the peak region. The parameters of the Gaussian plus quadratic background function,

$$y(x_i) = c_1 \exp\left[-\frac{1}{2}\left(\frac{x_i - \bar{x}}{\sigma}\right)^2\right] + c_2 + c_3 x_i + c_4 x_i^2 ,$$

which are varied to obtain the best fit to the data, y_i, are the centroid or mean, $\bar{x}$, the full width at half maximum, $\Gamma = 2.354\sigma$, where σ is the standard deviation, and the peak area, which is related to c_1. The parameters c_2, c_3 and c_4 have already been determined from fitting the stable

background regions. The best fit is defined as the minimum χ^2 where $\chi^2 = \sum_i [(y_i - y(x_i)/\sigma_i]^2$. The program iterates until two successive values of χ^2 differ by less than a predetermined quantity (5×10^{-4} for this work) or for a maximum of 15 iterations. An example of a fit to several overlapping peaks plus a quadratic background is shown in Fig. II-1. Very little low energy tailing was observed, consequently a simple Gaussian peak shape was adequate.

B. The Results - General Comments

The idealized picture of the low-lying level structure of a vibrational nucleus was shown in Fig. I-1. The results presented here are an attempt to measure the cross sections for the production of those gamma-rays shown in Fig. I-1 for 7 to 26-MeV proton bombardment and 14-MeV neutron bombardment of a number of even-even target nuclei. The nuclei investigated are ^{56}Fe, isotopes of Ni and Zn, ^{108}Pd, isotopes of Cd and Sn, and ^{206}Pb. Before discussing the results for the individual nuclei, we will indicate the general features observed in the present work and their systematic behavior with incident energy and target mass.

When nuclei, with the characteristic level structure shown in Fig. I-1, undergo gamma decay from sufficiently highly excited states, the result is generally a cascade of gamma transitions down to the ground state. What is observed is that virtually all of the gamma decay funnels down through the first 2^+ level followed by decay to the ground state.

The $2^+ \rightarrow 0^+$ transition, labeled (1) in Fig. I-1, is usually the strongest transition in the spectrum. The first 2^+ level is fed primarily by the by the $4^+ \rightarrow 2^+$ transition, labeled (2) in Fig. I-1, which generally accounts for about one half of the strength of the $2^+ \rightarrow 0^+$ transition.

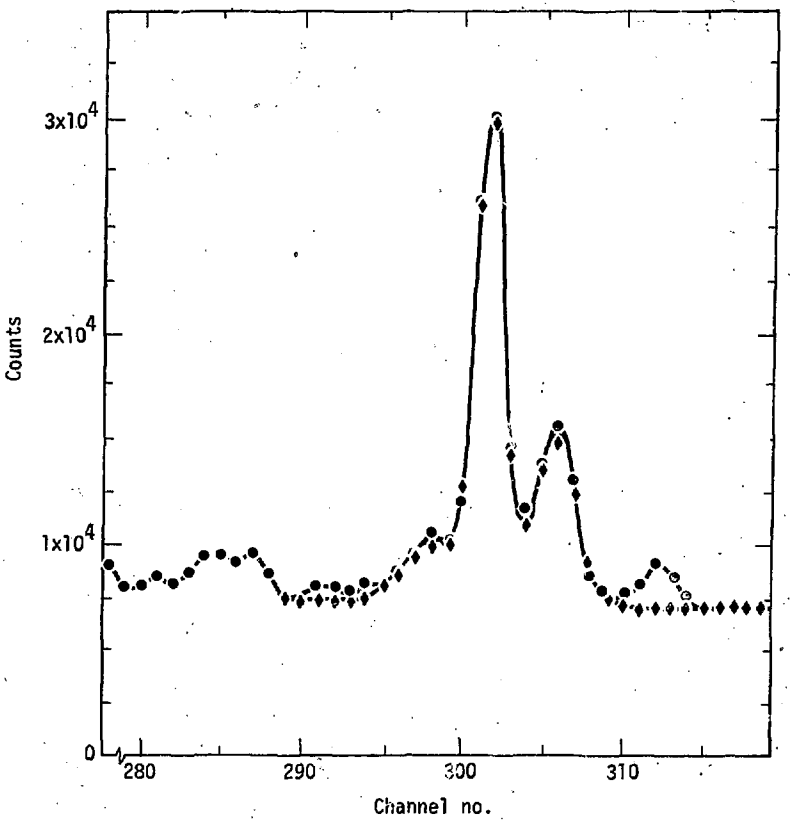

Fig. III-1. A GRASP calculated fit (-♦-) to an experimental gamma triplet of about 430 keV (-●-).

The formation of the 4^+ level requires that more angular momentum be brought into the nucleus than does the formation of 2^+ or 0^+ levels. Consequently the $4^+ \rightarrow 2^+$ transition is relatively less important at low incident particle energies than it is at high energies. In some nuclei the $3^- \rightarrow 2^+$ transition, labeled (6) in Fig I-1, is more important than the $4^+ \rightarrow 2^+$ transition.

The $2_1^+ \rightarrow 2^+$ transition, labeled (3), and the $2_1^+ \rightarrow 0^+$ transition, labeled (5), are also investigated. The $2_1^+ \rightarrow 0^+$ transition is important because it bypasses the first 2^+ leve and decays directly to the ground state. This transition is observed to be always very weak compared to the $2^+ \rightarrow 0^+$ transition.

The $0_1^+ \rightarrow 2^+$ transition, labeled (4), is also of interest because it gives an indication of the amount f feeding of the 0^+ ground state from higher lying states other than the first 2^+. This is important because it indicates the amount of gamma decay b passing the first 2^+ state. The feeding of these two 0^+ levels will be similar only if the configurational details of the final 0^+ state are not important because of averaging over many possible initial configurations and intermediate transitions. These arguments require the qualitative validity of a statistical picture for the gamma cascades. This transition is always weak but it is relatively strongest at low incident particle energies where very little angular momentum is brought into the nucleus and decay to low spin states is favored.

B.1 The (p,p') Results

The gamma cascades generally start from high energy states (E_x = 5-8 MeV) in the final nucleus. This can be seen by examining the

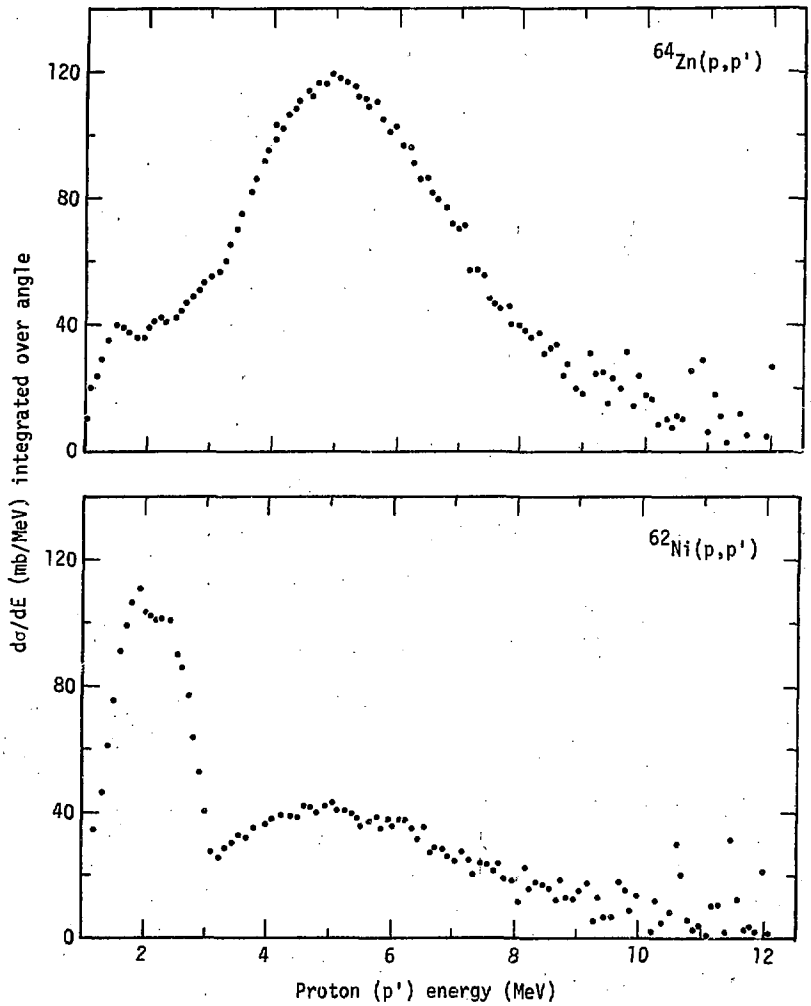

Fig. III-2. The ^{64}Zn(p,p') and ^{62}Ni(p,p') spectra of Sprinzak et al.[5] for 14 MeV incident protons.

difference between incoming and outgoing proton energies. Fig. III-2 shows the scattered proton spectra of Sprinzak et al.[5] for 14-MeV protons on ^{64}Zn and ^{62}Ni. The (p,p') part of the spectra peaks around 5-MeV. Hence the final nucleus is left with 9-MeV excitation, on the average. The nucleus is also left with several units of angular momentum, as can be inferred from Table III-1. This table lists the most probable angular momentum transfer to the compound nucleus, as calculated by the LOKI[34] optical model code. The scattered particles will be emitted with much less energy and angular momentum; s-wave (ℓ=0) and p-wave (ℓ=1) events are favored. Consequently the final nucleus will be left with most of the angular momentum deposited by the incident particle. For the nuclei investigated, over the range of incident proton energies from 8 to 26-MeV, the most probable angular momentum transferred varies from 2 to 6 units. The predominant feeding of high angular momentum final states (e.g., the 4^+ rather than the 0^+) can be qualitatively understood in terms of the difficulty of getting rid of large amounts of initial angular momentum during the cascade.

Also important in understanding the behavior of the gamma cascades and the relative feeding of the various low-lying states is the spin dependence of the level density, which typically peaks at 3 to 4 units[6] in the region of closely-spaced levels at 5-8 MeV excitation.

If the final nucleus is left with enough energy to emit another particle, it will usually do so. States above the neutron separation energy decay predominantly by neutron emission. A compilation of neutron, proton, and alpha separation energies for the nuclei investigated is given in Table III-2.[15] Looking again at the ^{62}Ni proton data[5] in Fig. III-2, a substantial lower energy peak is apparent just below the neutron separation

Table III - 1

Most Probable Angular Momentum Transferred to the Compound Nucleus as a Function of Incident Proton Energy - from LOKI[34] Optical Model Calculations

Nucleus	Energy (MeV)	Angular Momentum Transfer 10	12	14	17	20	23	26
^{56}Fe		2.5	3.0	3.2	3.6	4.0	4.6	5.0
^{62}Ni		2.7	3.1	3.3	3.7	4.3	4.6	5.0
^{64}Zn		2.8	3.0	3.2	3.5	4.3	4.5	5.0
^{110}Cd		2.3	2.7	3.5	3.8	4.6	4.8	5.5
^{114}Cd		2.3	2.8	3.5	4.1	5.0	5.0	5.6
^{116}Cd		2.4	2.8	3.5	4.2	5.0	5.2	6.0
^{116}Sn		2.3	2.6	3.5	4.2	4.8	5.3	5.5
^{120}Sn		2.4	2.8	3.5	4.1	5.0	5.4	5.6
^{206}Pb		1.5	2.5	3.5	4.0	4.5	5.5	6.0

TABLE III - 2

Particle Separation Energies (MeV)

	Sn	Sp	Sα
^{56}Fe	11.20	10.19	7.62
^{58}Ni	12.20	8.18	6.41
^{60}Ni	11.39	9.53	6.30
^{62}Ni	10.60	11.12	7.02
^{64}Zn	11.86	7.71	3.95
^{66}Zn	11.05	8.92	4.57
^{108}Pd	9.23	9.95	3.86
^{110}Cd	9.88	8.91	2.86
^{112}Cd	9.40	9.64	3.48
^{114}Cd	9.04	10.27	4.10
^{116}Cd	8.70	11.09	4.87
^{116}Sn	9.56	9.27	3.37
^{118}Sn	9.33	10.01	4.06
^{120}Sn	9.10	10.66	4.80
^{206}Pb	8.08	7.25	-1.15

energy at 10.6-MeV. This comes from (p,np) protons which have energies below E - Sn = 3.2-MeV. In this particular case it is relatively easy to separate the protons due to (p,np) events from those due to (p,p') events. At higher energies the situation becomes more ambiguous, it may be necessary to use gamma data, such as those presented here, if one is interested in separating the (p,p') or (n,n') cross sections from the total inelastic cross sections.

When the final nucleus is left below the particle emission threshold, it will gamma decay. Degnan et al.[9] have determined the multiplicities of the gamma cascade following (p,p') reactions on nuclei over the mass range 59 to 122. They have observed a strong similarity between gamma multiplicities from all of the different nuclei. For an incident energy of 17-MeV, they observe the multiplicity to vary smoothly with initial excitation energy from about 4 at 10-MeV to about 1 at 2-MeV.

The collective vibrational levels of spherical even-even nuclei are also strongly excited by direct reactions. In the (p,p') spectra, the direct excitation manifests itself as strong high energy peaks which were not included in the integration of the (p,p') data. In the gamma spectra it is simply another contributor to the various low-lying transitions shown in Fig. I-1, most of which go into the $2^+ \rightarrow 0^+$ transition. Therefore, if one desires to compare gamma cross sections with integrated proton or neutron cross sections which do not include the low-lying states, it is necessary to determine the amount of direct excitation contributing to the gamma cross sections. This can be calculated quite successfully using the coupled-channel formalism described by Tamura.[18] The Oregon State Coupled-Channel Code[17] was used to perform these calculations, which will be described in detail in Section IV.

The calculated direct excitation of the various collective levels is subtracted from the gamma data before they are compared with integrated (p,p') data. These calculations have been checked against (p,p') measurements of individual collective levels, when available, and the agreement between data and calculation is generally quite good. A summary of the results of the coupled-channel calculations is given in Table III-3. The calculated direct excitations, along with the measured total cross sections, are listed in columns for each of the transitions of interest and for all of the nuclei studied. The sum of the direct contributions, $\Sigma\sigma$ direct, is listed in a column at the right. This is subtracted from the total $2^+ \rightarrow 0^+$ cross section with the result, σ'_{2^+}, listed in the next column at the right. These numbers can then be compared directly with integrated (p,p') spectra, $\sigma(p,p')$, some of which are given in the next column. The furthest column on the right lists the percentage of the direct reaction contributing to the total measured gamma cross section. This is substantial in nearly all cases, being of the order of 40%. For the lighter nuclei there is substantial variation with incident proton energy. In ^{64}Zn, for instance, direct reactions contribute 8% at 9-MeV, rising to 50% at 26-MeV. A similar summary is given in Table III-4 for the neutron experiments.

In general, the gamma spectra were measured with the Ge(Li) detector only at an angle of 125° with respect to the proton beam. The only exception was ^{120}Sn which was measured at 90°. The total gamma cross sections were calculated from the expression

$$4\pi(d\sigma/d\Omega)_{125°} ,$$

Table III - 3

A Summary of Measured (p,p'γ) Gamma Cross Sections, Coupled-Channel Calculations, σ_{direct}, and Integrated Proton Data, $\sigma(p,p')$

$4\pi(d\sigma/d\Omega)_{125°}$ (mb)

Nucleus	Ep	$\sigma(2_1^+ \to 0^+)$	c.c. Calc.	$\sigma(4^+ \to 2^+)$	c.c. Calc.	$\sigma(2_1^+ \to 2^+)$	c.c. Calc.	$\sigma(0_1^+ \to 2^+)$	c.c. Calc.	$\sigma(3^- \to 2^+)$	c.c. Calc.	$\Sigma\sigma_{direct}$	$\sigma_{2^+}^{*}$	$\sigma(p,p')$		Percent Direct
^{56}Fe	9	350 ± 20	22.7	85 ± 5	1.0	44 ± 4	1.2	7 ± 1	2.2		1.4	28.5	321 ± 20			8
	14	450 ± 20	41.6	190 ± 9	2.8	50 ± 4	2.3	2.5 ± 1	3.6		7.6	57.9	392 ± 20	374		13
	20	248 ± 20	36.4	111 ± 6	2.2	24 ± 2	1.6	1.8 ± .5	2.6		10.8	53.6	194 ± 20			22
	26	~210	32.5	~70	1.7	~23	1.0	~1.5	2.0		12.3	49.5	~160			24
^{62}Ni	9	130 ± 8	16.4	19 ± 2	1.0	9 ± 1	1.4	7 ± 1	3.2		2.1	24.1	106 ± 8			19
	14	210 ± 10	33.6	5[illegible] ± 3	2.9	15 ± 2	2.7	7 ± 1	4.5		8.7	52.4	154 ± 10	190		25
	20	147 ± 8	33.4	43 ± 3	2.7	10 ± 1	1.9	3 ± 1	3.2		12.5	53.7	93 ± 7			37
	26	130 ± 8	32.1	32 ± 3	2.2	9 ± 1	1.4	2.5 ± 1	2.6		14.2	52.5	78 ± 8			40
^{64}Zn	9	461 ± 20	26.3	68 ± 3	0.8	113 ± 5	1.8	14 ± 2	2.3		3.7	34.9	426 ± 20			8
	14	500 ± 20	53.5	140 ± 5	3.1	130 ± 10	3.3	6 ± 1	3.4		13.9	77.2	423 ± 20	498		15
	20	219 ± 11	51.3	66 ± 3	2.7	40 ± 2	2.2	1 ± .5	2.2		19.6	78.0	141 ± 11			36
	26	~150	47.4	~40	1.9	~26	1.3	~0	1.6		22.3	74.5	~76			50
^{108}Pd	10	43 ± 3	13.2	6 ± 1	1.3	6 ± 1	1.6	4 ± 2	1.2		1.7	19.0	24 ± 3			44
	14	100 ± 5	34.2	21 ± 1	3.9	15 ± 1	3.2	3 ± 1	2.2		6.5	50.0	50 ± 5			50
	20	125 ± 6	41.3	40 ± 2	4.2	18 ± 1	2.7	3 ± 1	1.7		10.4	60.3	65 ± 6			50
	26	133 ± 6	40.9	38 ± 2	3.2	21 ± 5	1.9	3 ± 1	1.4		11.3	58.7	74 ± 6			44
^{110}Cd	10	34 ± 2	10.6	10 ± 6	0.4	4 ± 1	~0.6	3.5 ± 1	0.5		1.8	13.9	20 ± 2			41
	14	105 ± 8	28.4	37 ± 2	1.4	10 ± 1	1.0	3 ± 1	1.1		8.3	40.2	65 ± 8	64		37
	20	122 ± 8	31.5	48 ± 5	1.5	11 ± 1	0.8	1 ± 1	0.9		13.8	48.5	74 ± 8			40
	26	~122	30.2	~48	1.1	~8	~0.5	~0	0.7		15.4	47.9	74 ± 8			39

Table III - 3 (Continued)

Nucleus	Ep	$\sigma(2^+_1 \to 0^+_1)$	c.c. Calc.	$\sigma(4^+_1 \to 2^+_1)$	c.c. Calc.	$\sigma(2^+_2 \to 2^+_1)$	c.c. Calc.	$\sigma(0^+_2 \to 2^+_1)$	c.c. Calc.	$\sigma(3^- \to 2^+_1)$	c.c. Calc.	$\Sigma\sigma_{direct}$	σ'_{2^+}*	$\sigma(p,p')$	Percent Direct
^{114}Cd	10	30 ± 5	11.2	5.5 ± 1	1.4	5.0 ± 1	0.9	3.5 ± 1	1.2		1.6	16.3	14 ± 5		54
	14	84 ± 8	27.6	19 ± 2	4.6	13 ± 2	2.0	8.5 ± 2	2.3		6.6	43.1	41 ± 8	47	51
	20	109 ± 8	31.0	34 ± 2	7.1	14 ± 2	2.4	9 ± 2	2.5		10.7	53.7	55 ± 8		49
	26	112 ± 8	29.4	42 ± 2	6.5	14 ± 2	2.1	9 ± 2	2.1		11.7	51.8	60 ± 8		46
^{116}Cd	10	31 ± 8	11.2	17 ± 5	0.6	3 ± 1	0.3	2 ± 1	0.5		1.6	14.2	17 ± 8		46
	14	98 ± 10	28.2	70 ± 5	1.8	15 ± 3	0.7	10 ± 2	1.0		6.8	38.5	60 ±10	49	39
	20	120 ± 15	32.9	73 ± 5	3.9	25 ± 3	0.7	11 ± 2	0.9		10.7	47.1	73 ±15		39
	26	120 ± 15	31.2	50 ± 5	1.4	19 ± 3	0.5	9 ± 2	0.6		11.7	45.4	75 ±15		38
^{116}Sn	10	19 ± 1	3.1	1 ± .5	-*	1 ± .5	-*	1 ± .5	-*	2 ± 1	1.8	6.3*	13 ± 1		33
	14	56 ± 3	10.2	6 ± 1	-	3 ± .5	-	2 ± .5	-	14 ± 2	10.0	23.7	32 ± 3		42
	20	75 ± 5	11.6	100 ± 5	-	4 ± .5	-	1.5 ± .7	-	30 ± 2	17.4	32.5	43 ± 5		43
	26	75 ± 5	11.2	96 ± 5	-	4.5 ± .5	-	0	-	35 ± 3	19.4	33.1	42 ± 5		44
^{120}Sn	10	18 ± 7	2.8	2 ± 2	-*	3 ±2	-*	-	-*	2 ± 2	1.1	5.3*	13 ± 7		29
	14	61 ± 15	8.5	10 ± 3	-	8 ±4	-	-	-	10 ± 3	5.7	17.7	43 ± 15	34	29
	20	80 ± 15	9.8	30 ± 5	-	17 ±4	-	-	-	30 ± 5	9.7	23.0	57 ± 15		29
	26	-	9.4	-	-	-	-	-	-	-	10.7	-	-		-
^{206}Pb	14	14 ± 2	1.7	20 ± 3	0.3	4 ±1	0.1	∿0	0.2	3.5 ± 1	1.8	4.1	10 ± 2		29
	20	51 ± 15	3.7	200 ± 30	1.3	5.0 ±1	0.2	∿1 ± 1	0.4	8.5 ± 1	8.0	13.6	45 ± 15		23
	26	72 ± 15	3.7	75 ± 10	1.4	5.5 ±1	0.2	∿2 ± 1	0.4	8.5 ± 1	10.3	16.0	56 ± 15		22

* Deformation parameters were not available for any level other than the 2^+ and 3^- in these nuclei. The calculated cross sections from ^{116}Cd were used for the 2^+_1, 0^+_1, and 4^+ levels.

** $\sigma'_{2^+} = \sigma(2^+ \to 0^+) - \Sigma\sigma_{direct}$

which assumes that the P_4 Legendre polynomial coefficient is zero, which is probably not true. The angular distributions are discussed in more detail in Section III-B-2.

^{56}Fe

The excitation functions for the various gamma transitions from ^{56}Fe $(p,p'\gamma)$ reactions are shown in Fig. III-3. A typical Ge(Li) gamma spectrum, taken at 10.5-MeV, is shown in Fig. III-4. All data were taken at 125°. The behavior of the cross sections with energy (i.e. the shapes of the curves in Fig. III-3) can be understood in terms of the angular momentum deposited in the nucleus and the spins of the low-lying levels. The $2^+ \rightarrow 0^+$ transition strength peaks when about 3 units of angular momentum are brought into the nucleus. The $4^+ \rightarrow 2^+$ transition peaks at higher energies, when more angular momentum is brought in and the $0_1^+ \rightarrow 2^+$ transition peaks at very low energy when less angular momentum is brought into the nucleus. The behavior of the gamma transitions observed for ^{56}Fe is typical of the lighter nuclei ^{62}Ni and ^{64}Zn also.

The $2^+ \rightarrow 0^+$ transition (0.847-MeV) is the strongest line in the spectrum. It rises from 300 mb at 7.5-MeV, to a maximum of about 450 mb at about 14.5-MeV. From Table III-1, it can be seen that this peak value corresponds to about 3 units of angular momentum being deposited in the nucleus. Above 15-MeV the 2^+ cross section decreases gradually with increasing proton energy to about 200 mb at 24-MeV.

In order to compare the $2^+ \rightarrow 0^+$ cross sections with measured (p,p') data, the calculated direct excitation of the collective levels was subtracted from the measured gamma cross sections. The

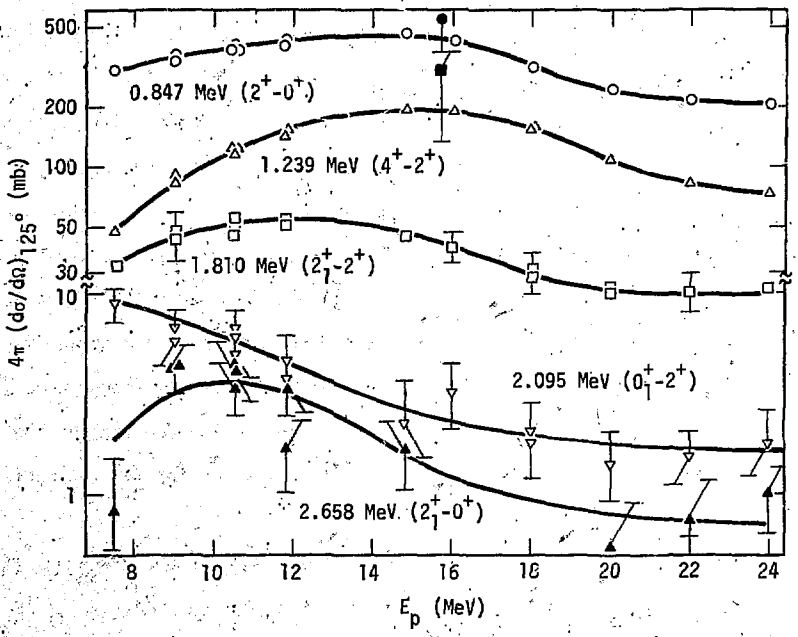

Fig. III-3. The ^{56}Fe(p,p'γ) gamma excitation functions and the ORNL data[11] (● ■)

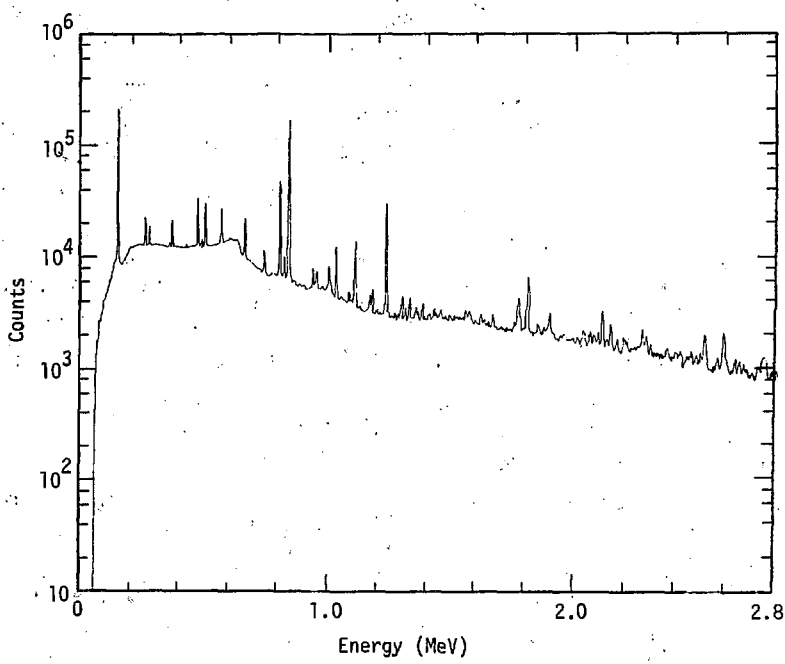

Fig. III-4. The $^{56}Fe(p,p'\gamma)$ gamma spectrum at 125° for 10.5 MeV protons

results of this are listed in Table III-3 and, for the $2^+ \rightarrow 0^+$ cross section, are plotted in Fig. III-5. Direct reactions contribute 8% to 24% of the 2^+ cross section for incident proton energies of 8 to 26-MeV. Also plotted are the (p,p') data of Sprinzak et al.[5] at 14-MeV integrated over angle and energy. The solid line is simply to guide the eye. The 2^+ cross section rises from the Coulomb barrier near 5-MeV and peaks at about 15-MeV. Agreement between the integrated (p,p') data and the $2^+ \rightarrow 0^+$ gamma cross section is quite good. The 2^+ cross section is also in good agreement with (p,p'γ) measurements from ORNL[11] done at 15.7-MeV.

The $4^+ \rightarrow 2^+$ transition (1.239-MeV) has slightly less than half the strength of the $2^+ \rightarrow 0^+$ transition and is the principal decay feeding the first 2^+ level. It rises more sharply from low energy, and peaks at a slightly higher energy, than does the 2^+ transition. It is less likely to be populated at lower energies because the protons do not deposit enough angular momentum in the nucleus. Proton energies of 17-MeV or more are necessary before the angular momentum distribution peaks near 4 units.

The $2_1^+ \rightarrow 2^+$ transition (1,810-MeV) is another member of the two phonon triplet which decays strongly to the one phonon 2^+ state. It peaks at substantially lower energies and is substantially weaker (by a factor of 10) than the $2^+ \rightarrow 0^+$ transition.

The $0_1^+ \rightarrow 2^+$ transition (2.095-MeV) peaks at very low energies where only 1 or 2 units of angular momentum are brought into the nucleus by the incident protons. Under these circumstances the

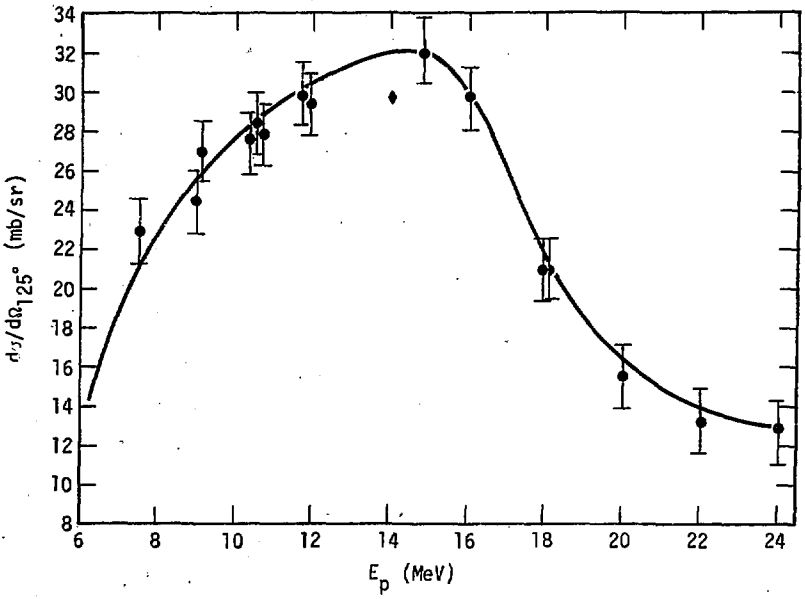

Fig. III-5. The $^{56}Fe(p,p'\gamma)$ 0.847 MeV ($2^+ \rightarrow 0^+$) gamma excitation function minus direct at 125° (♦); proton data (♦).

conditions are most favorable for decay through a 0^+ state. We expect that the 0^+ ground state will be fed from higher-lying states in a similar way.

The $2_1^+ \rightarrow 0^+$ transition (2.658-MeV) is the decay of the two phonon 2^+ state directly to the ground state and is very weak. It rises rapidly, peaking at about 4.5 mb at low energy (10-MeV) and then decreases to about 1 mb. The strength of this transition is an indication of the error involved in using the decay of the first 2^+ state as a measure of $\sigma(p,p')$. Its strength is, however, more than two orders of magnitude less than that of the first 2^+.

^{62}Ni

The results for ^{62}Ni are very similar to those for ^{56}Fe. The measured strengths of the various gamma transitions are shown in Fig. III-6. A typical gamma spectrum is shown in Fig. III-7. All data were taken at 125°.

The $2^+ \rightarrow 0^+$ transition (1.173-MeV) peaks at about 210 mb for 15-MeV incident protons. As with ^{56}Fe, the cross section then decreases to about 130 mb at 26-MeV. Fig. III-8 is a plot of the $2^+ \rightarrow 0^+$ cross section with the direct excitation, as calculated by the coupled-channel code, subtracted. The solid line is simply to guide the eye. Also plotted are the integrated (p,p') cross sections of Sprinzak et al.,[5] Rao et al.,[1] and Lu et al.[12] The (p,p') data are systematically slightly higher than the gamma data but the error bars tend to overlap. It is expected that the $2^+ \rightarrow 0^+$ cross section will slightly underestimate the (p,p') cross section due to transitions bypassing the first 2^+ state.

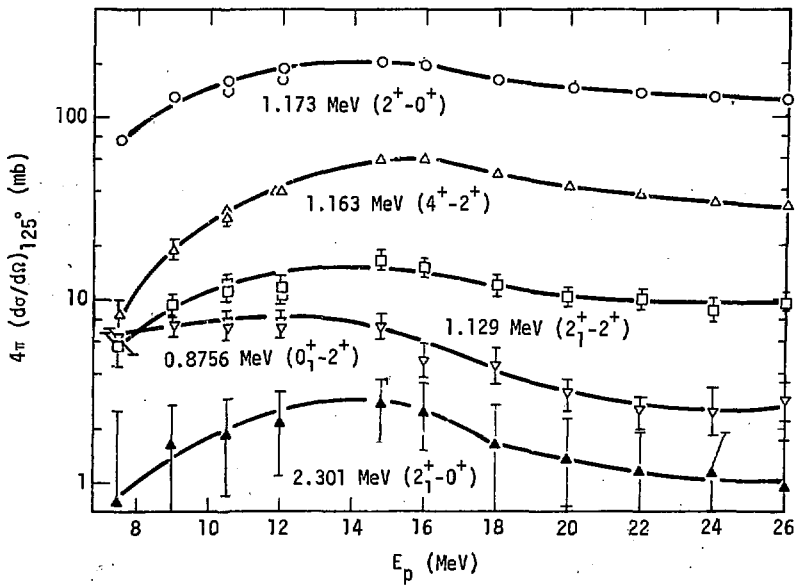

Fig. III-6. The $^{62}Ni(p,p'\gamma)$ gamma excitation functions at 125°.

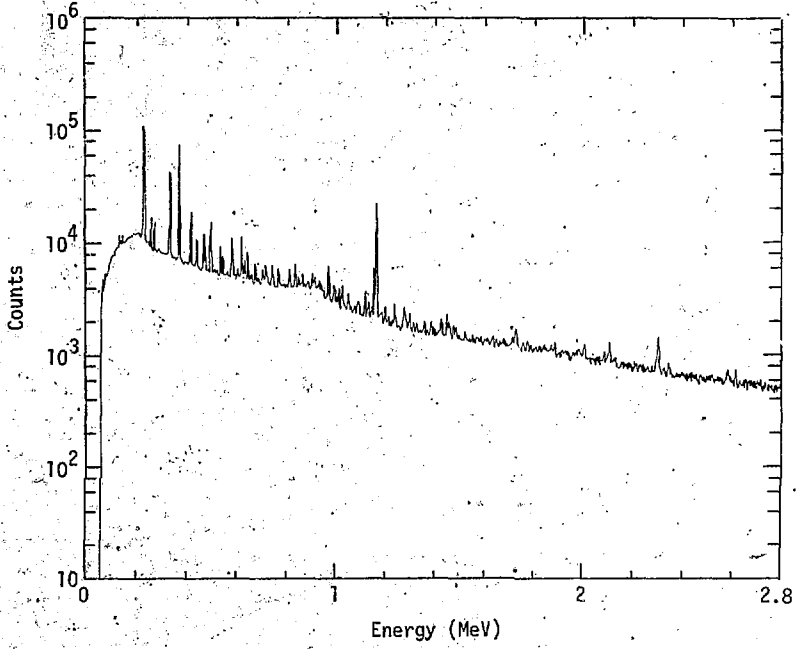

Fig. III-7. The $^{62}Ni(p,p'\gamma)$ gamma spectrum at 125° for 10.5 MeV protons

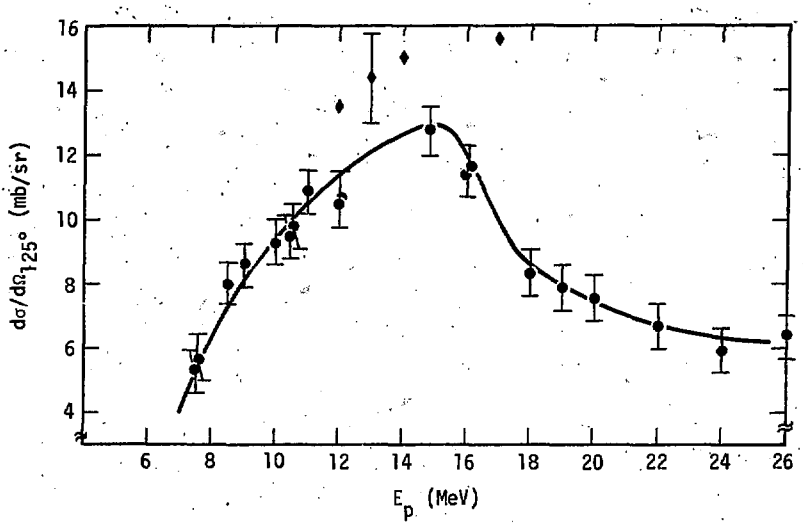

Fig. III-8. The $^{62}Ni(p,p'\gamma)$ 1.173 MeV ($2^+ \rightarrow 0^+$) gamma excitation function minus direct at 125° (♦); proton data (♦).

That appears to be the case here. The underestimate is of the order of 14% and is one of the larger differences between (p,p') and gamma data observed in this work.

As with ^{56}Fe, the $4^+ \rightarrow 2^+$ transition (1.163-MeV) is the principal level feeding the first 2^+ state and its strength peaks at about 15-MeV when about 4 units of angular momentum are brought into the nucleus. Also observed are the $2_1^+ \rightarrow 2^+$ transition (1.129-MeV) and the $0_1^+ \rightarrow 2^+$ transition (0.8756-MeV) whose strength peaks at low energies and decreases to a few percent of the $2^+ \rightarrow 0^+$ strength at higher energies. The decay of the 2_1^+ directly to the ground state, the $2_1^+ \rightarrow 0^+$ transition (2.301-MeV) is weak, of the order of 1% of the $2^+ \rightarrow 0^+$ strength.

^{64}Zn

As with ^{62}Ni, the gamma decay of the collective levels of ^{64}Zn, shown in Fig. III-9, is very similar to that of ^{56}Fe. There are substantial differences in magnitude, but the variations with the energy are similar. Fig. III-10 shows a typical gamma ray spectrum from ^{64}Zn. The measurements were all done at 125°.

The $2^+ \rightarrow 0^+$ transition (0.991-MeV) peaks at about 540 mb for 13-MeV incident protons. It then decreases with increasing energy to 160 mb at 24-MeV. Fig. III-11 shows the variation of the 2^+ differential cross section with energy, after the direct excitation of the collective levels has been subtracted. The transition strength rises sharply from the Coulomb barrier to a broad peak, at about 13-MeV, which corresponds roughly to the neutron separation energy in the final nucleus. For higher energies the decay goes increasingly by neutron emission and the $(p,p'\gamma)$ cross section falls steadily with increasing

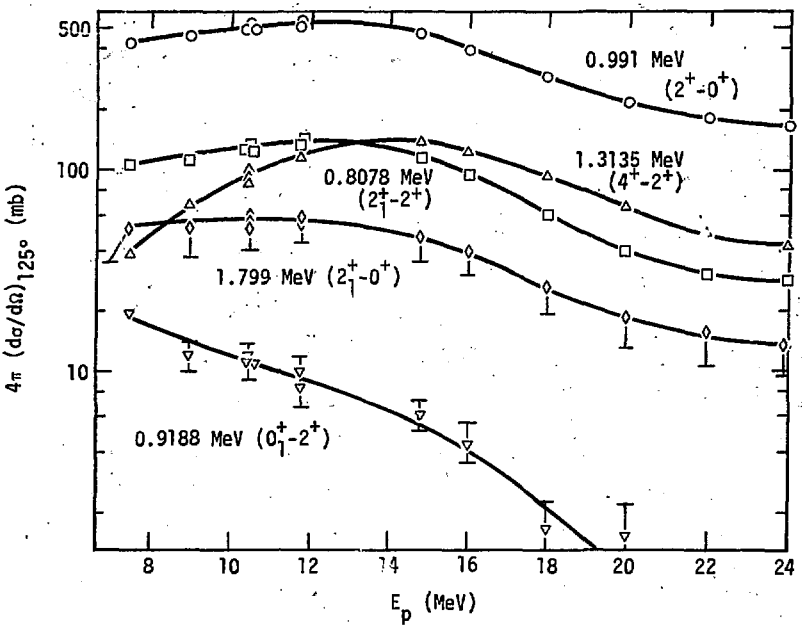

Fig. III-9. The $^{64}Zn(p,p'\gamma)$ gamma excitation functions at 125°.

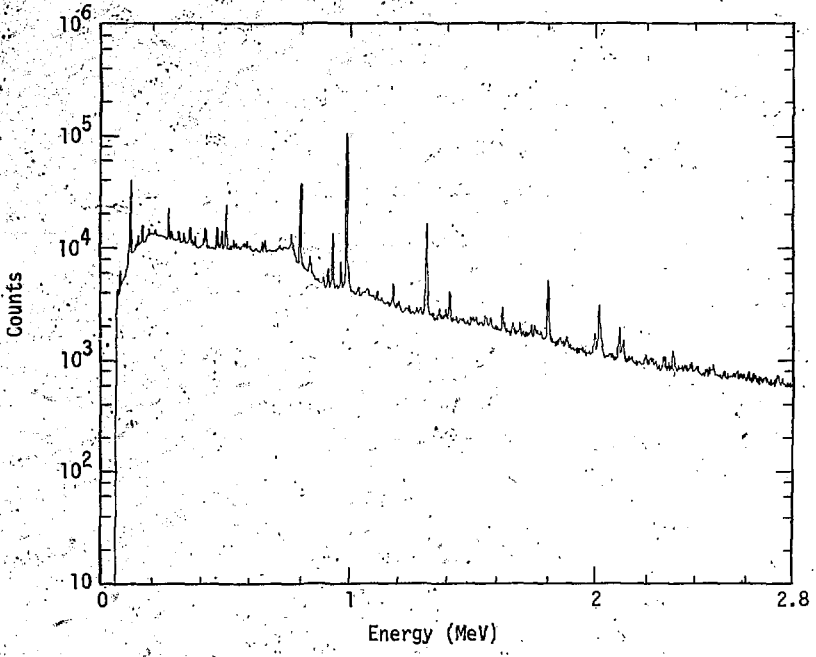

Fig. III-10. The $^{64}Zn(p,p'\gamma)$ gamma spectrum at 125° for 11.8 MeV protons

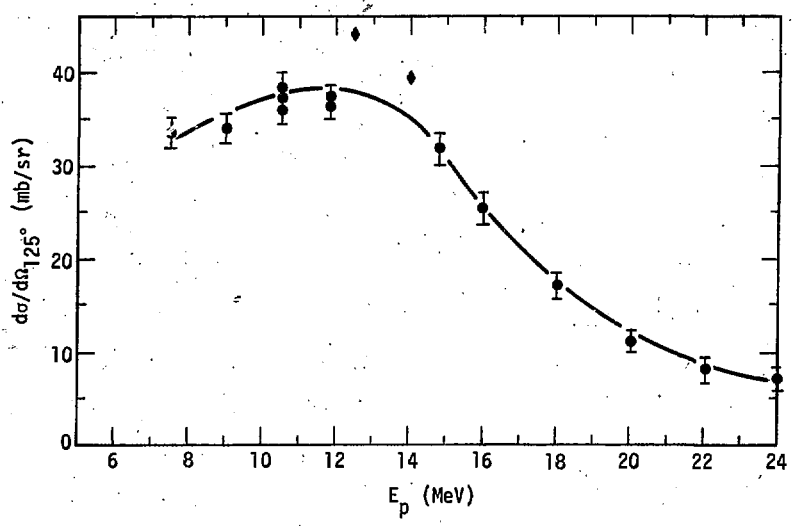

Fig. III-11. The $^{64}Zn(p,p'\gamma)$ 0.991 MeV $(2^+ \rightarrow 0^+)$ gamma excitation function at 125° minus calculated direct excitation ( ), and integrated proton data ( ).

energy. The integrated (p,p') data of Sprinzak et al.[5] and Lux and Porile[13] is also plotted on this figure. The gamma data is slightly lower, but in general the agreement is quite good.

The strengths of the $4^+ \rightarrow 2^+$ transition (1.3135-MeV) and the $2_1^+ \rightarrow 2^+$ transition (0.8078-MeV) are nearly the same and about 1/3 that of the $2^+ \rightarrow 0^+$. The $(2_1^+ \rightarrow 2^+)$ peaks lower than the $(4^+ \rightarrow 2^+)$ because of angular momentum considerations. The $(0_1^+ \rightarrow 2^+)$ transition (0.9188-MeV) is very weak in this case but behaves in the expected way. It is maximum at low energies, decreasing rapidly with increasing proton energy and angular momentum.

The $2_1^+ \rightarrow 0^+$ transition (1.799-MeV) is considerably stronger here than in most other nuclei. This measurement is not in agreement with published values for the branching ratio from the 2_1^+ level at 1.799-MeV.[35] The published branching ratio indicates that this transition should be only 2/3 of what we measured. This transition bypasses the first 2^+ level, and it is important to know its true strength. It could account for as much as 10% of the 2^+ strength or as little as 6%. This would be a significant source of error if the $2^+ \rightarrow 0^+$ transition were used as a measure of the (p,p') cross section. The observed difference between the integrated (p,p') data and the $2^+ \rightarrow 0^+$ gamma cross section is about equal to the strength of this transition.

^{108}Pd

This is the first of the intermediate mass spherical nuclei investigated. Fig. III-12 is a plot of the strength of the relevant gamma transitions for ^{108}Pd (p,p'γ) reactions as a function of proton energy.

A typical $(p,p'\gamma)$ spectrum is shown in Fig. III-13. All measurements were made at 125°.

The $2^+ \rightarrow 0^+$ transition (0.434-MeV) rises from the Coulomb barrier at 7.9-MeV and does not appear to have reached a maximum, even at 26-MeV. This is shown more clearly in Fig. III-14, which is a plot of the 2^+ strength with direct contributions, as calculated by the coupled-channel code, removed. No experimental (p,p') data were available for this nucleus.

The $4^+ \rightarrow 2^+$ transition (0.614-MeV) carries about 1/3 of the strength of the $2^+ \rightarrow 0^+$ transition, and becomes more important as incident energy and angular momentum increase. The $2_1^+ \rightarrow 2^+$ transition (0.498-MeV) is as strong as the $4^+ \rightarrow 2^+$ transition at low energy but becomes less important at higher energies, accounting for only 15% of the 2^+ strength at 26-MeV. The $(0_1^+ \rightarrow 2^+)$ transition (0.619-MeV) is weak, accounting for, at most, 4% of the 2^+ strength.

The $2_1^+ \rightarrow 0^+$ transition (0.931-MeV) is stronger here than in most of the other nuclei. A background gamma ray of exactly the same energy is observed in blank runs which may account for some of the strength. The branching ratio from the 2_1^+ level has been measured by Robinson et al.,[33] using Coulomb excitation, with the result

$$\frac{\sigma\left(2_1^+ \rightarrow 2^+\right)}{\sigma\left(2_1^+ \rightarrow 0^+\right)} = 3.5 \pm 0.7$$

Our measurements are generally not in agreement with this branching ratio and indicate extra strength in the 0.931-MeV transition. The $2_1^+ \rightarrow 0^+$ transition is probably only about 1/2 as strong as indicated by our measurement.

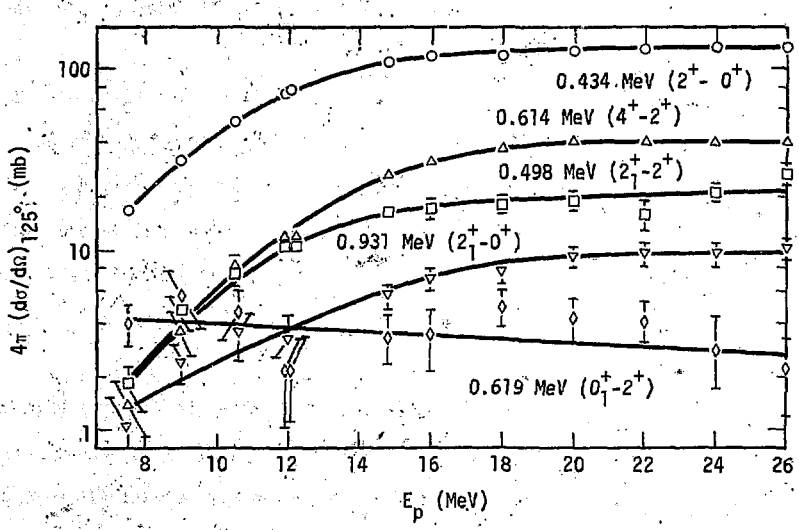

Fig. III-12. The ^{108}Pd(p,p'γ) gamma excitation functions at 125°.

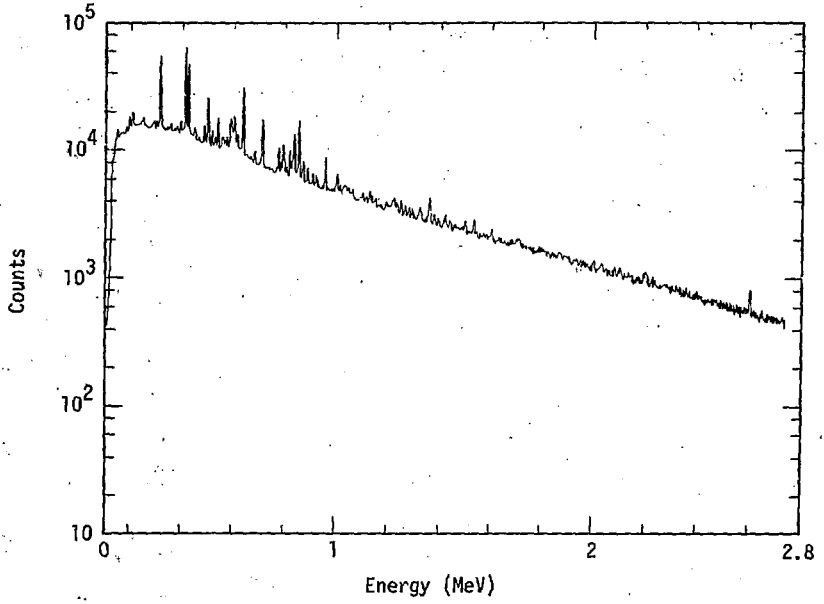

Fig. III-13. The $^{108}Pd(p,p'\gamma)$ gamma spectrum at 125° for 18 MeV protons.

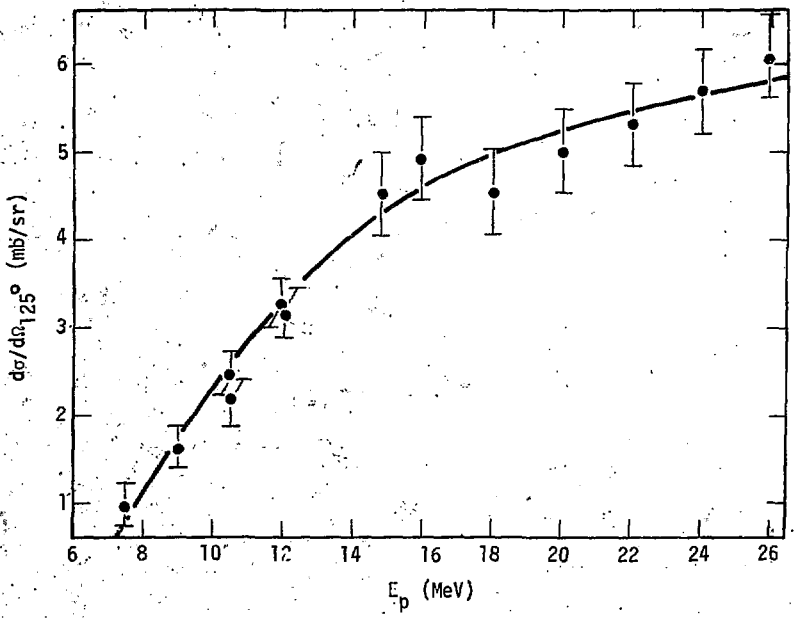

Fig. III-14. The $^{108}Pd(p,p'\gamma)$ 0.434 MeV ($2^+ \rightarrow 0^+$) gamma excitation function minus direct at 125° (Φ).

^{110}Cd

The excitation functions for the various gamma transitions from ^{110}Cd $(p,p'\gamma)$ reactions are shown in Fig. III-15. A typical Ge(Li) gamma spectrum is shown in Fig. III-16. All data were taken at 125°.

The $2^+ \rightarrow 0^+$ transition (0.6577-MeV) rises from the Coulomb barrier at 8-MeV and reaches a plateau of about 120 mb at about 16-MeV. The cross section remains essentially constant through 26-MeV. Fig. III-17 is a plot of the 2^+ strength with direct contributions, as calculated by the coupled-channel code, removed. Also plotted in this figure are integrated measurements of the (p,p') cross section at 12-MeV by Rao et al.[1] and at 16-MeV by Lux et al.[16] The agreement is good; however, another measurement by Rao et al.,[1] at 17-MeV, is high by a factor of two (≈12 mb/sr). The Rao cross section may be in error, because the ^{114}Cd, ^{116}Cd, and ^{120}Sn cross sections from the same reference, at 17-MeV, are all about a factor of two high in comparison with the later results of Cohen et al.[14] and the ^{120}Sn results of Kalbach,[8] at 17-MeV.

The $4^+ \rightarrow 2^+$ transition (0.8847-MeV) accounts for about 40% of the strength of the $2^+ \rightarrow 0^+$ and behaves in a similar way. The $2_1^+ \rightarrow 2^+$ transition (0.8180-MeV) accounts for about 10% of the strength of the 2^+ and seems to reach a plateau at about 16-MeV. The $0_1^+ \rightarrow 2^+$ transition (0.8155-MeV) is quite weak except at low energies where angular momentum considerations cause it to be fed preferentially.

The $2_1^+ \rightarrow 0^+$ transition (1.476-MeV) behaves in a way identical to the $2_1^+ \rightarrow 2^+$ transition. Its strength is about 6% of the 2^+ strength. One should therefore expect at least this amount of error in using the $2^+ \rightarrow 0^+$ transition as a measure of $\sigma(p,p')$.

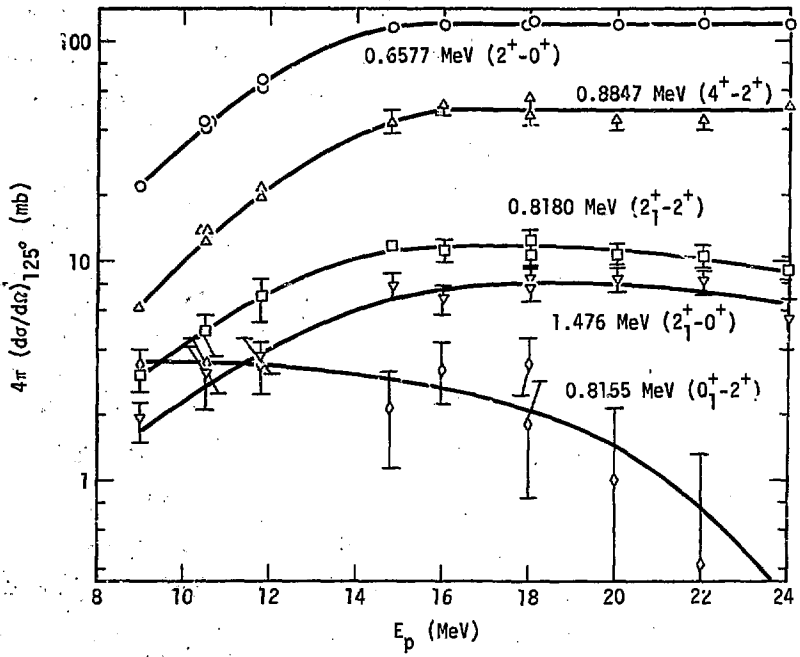

Fig. III-15. The $^{110}Cd(p,p'\gamma)$ gamma excitation functions at 125°.

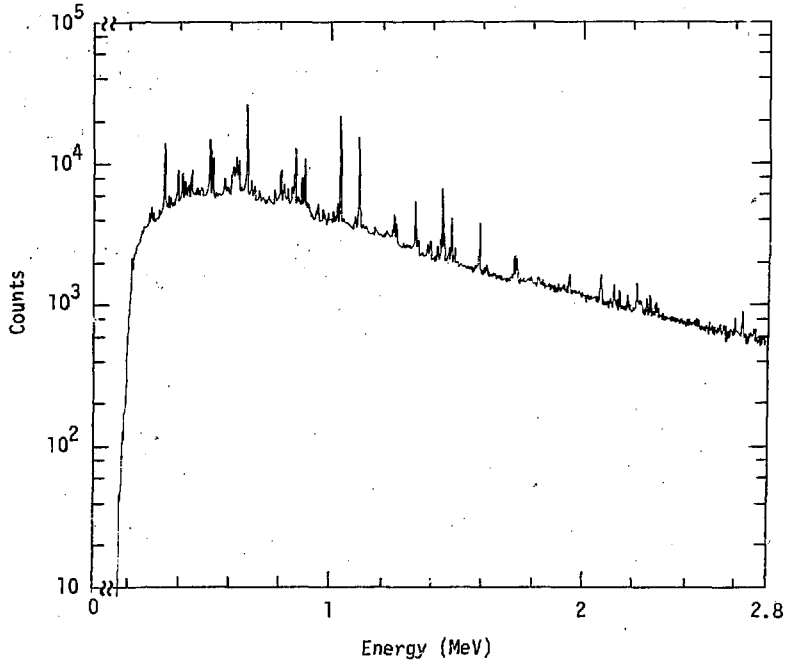

Fig. III-16. The $^{110}Cd(p,p'\gamma)$ gamma spectrum at 125° for 20 MeV protons

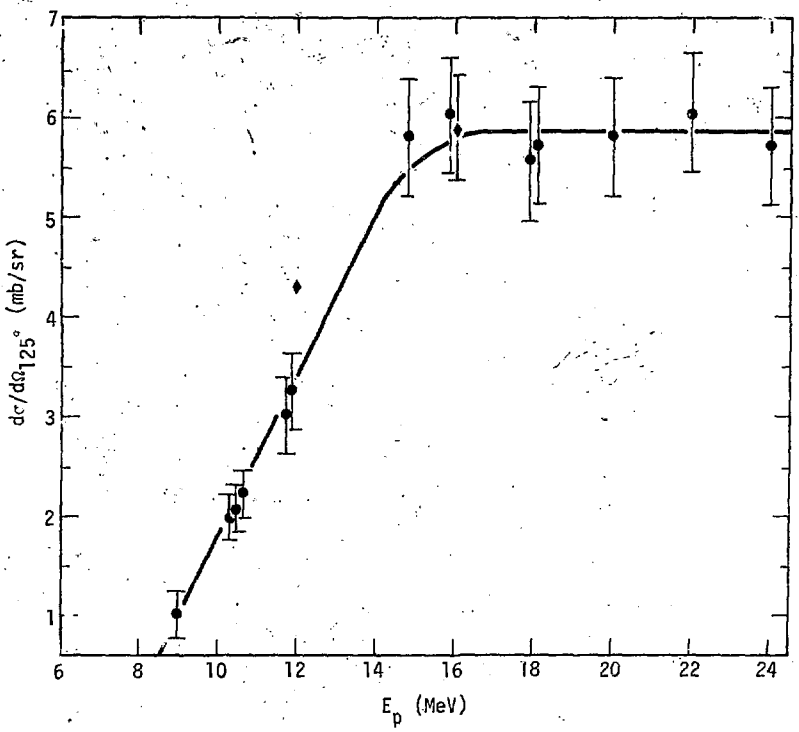

Fig. III-17. The $^{110}Cd(p,p'\gamma)$ 0.658 MeV $(2^+ \rightarrow 0^+)$ gamma excitation function minus direct at 125° (♦); proton data (♦)

^{114}Cd

The experimental gamma-ray cross sections for the various transitions of interest, as a function of the proton energy, are shown in Fig. III-18. A typical $(p,p'\gamma)$ spectrum is shown in Fig. III-19. All measurements were made at 125°.

The $2^+ \rightarrow 0^+$ transition (0.558-MeV) rises from the Coulomb barrier at about 8-MeV, reaches a plateau of about 100 mb at 18-MeV, and remains constant through 26-MeV. Fig. III-20 is a plot of this transition with the calculated direct excitation removed. Its behavior is similar to ^{110}Cd except that it appears to reach a somewhat lower plateau at a somewhat higher excitation energy. Plotted also are data from Rao et al.[1] at 12-MeV and Cohen et al.[14] at 16-MeV. An additional data point at 17-MeV was about a factor of two higher than we observed, and inconsistent with the data at 16-MeV, as was mentioned earlier.

The $4^+ \rightarrow 2^+$ transition (0.725-MeV) rises rapidly with proton energy and angular momentum deposited in the nucleus, eventually accounting for nearly 40% of the strength of the $2^+ \rightarrow 0^+$ transition. Its strength does not appear to reach a plateau but continues to rise, even at 26-MeV. The $2_1^+ \rightarrow 2^+$ transition (0.651-MeV) accounts for about 15% of the $2^+ \rightarrow 0^+$ strength and seems to reach a plateau at about 15-MeV.

The $0_1^+ \rightarrow 2^+$ transition (0.5759-MeV) accounts for somewhat less than 10% of the strength of the first 2^+, considerably more than its counterpart in ^{110}Cd, and increases with proton energy rather than decreasing as one would expect for a 0^+ level. This peak is one of a quadruplet of peaks which are very close in energy and difficult to resolve accurately. It may be that the other transitions are masking the behavior of the $0_1^+ \rightarrow 2^+$ transition.

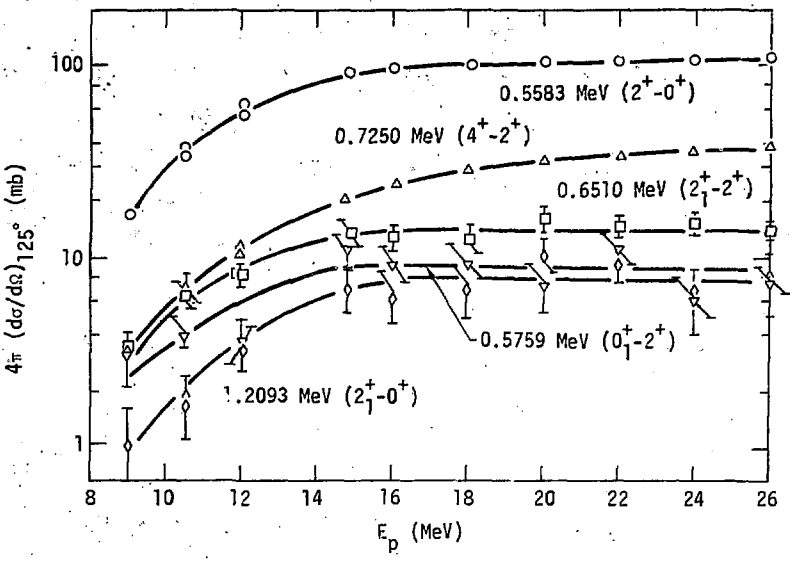

Fig. III-18. The ^{114}Cd(p,p'γ) gamma excitation functions.

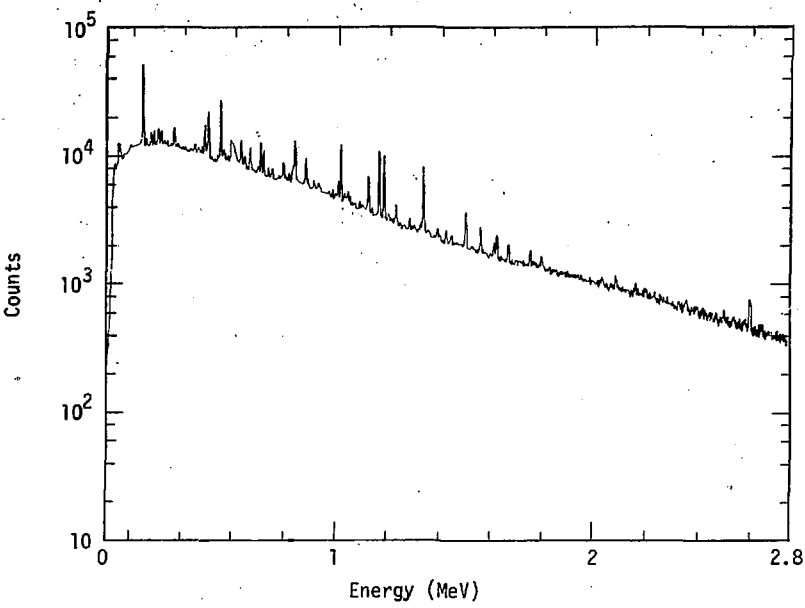

Fig. III-19. The $^{114}Cd(p,p'\gamma)$ gamma spectrum at 125° for 18 MeV protons

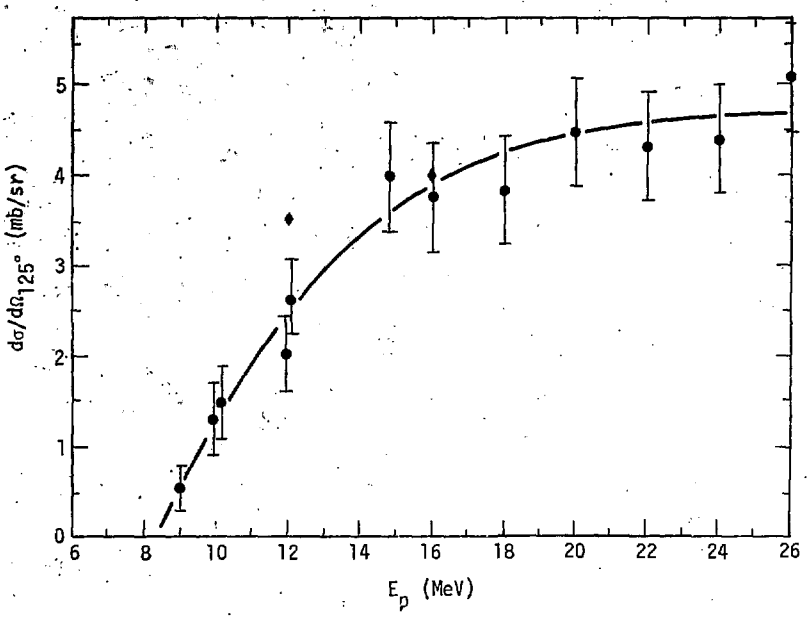

Fig. III-20. The $^{114}Cd(p,p'\gamma)$ 0.558 MeV $(2^+ \rightarrow 0^+)$ gamma excitation function minus direct at 125° (♦); proton data (♦)

The strength of the $2_1^+ \rightarrow 0^+$ transition is about 7% of the strength of the $2^+ \rightarrow 0^+$, and behaves in the same way with increasing proton energy as does the $2^+ \rightarrow 0^+$ transition. One can expect at least this much error in using the $2^+ \rightarrow 0^+$ transition as a measure of the (p,p') cross section.

^{116}Cd

The gamma-ray cross sections measured for this nucleus are shown in Fig. III-21. A typical $(p,p'\gamma)$ spectrum is shown in Fig. III-22. All measurements were made at 125°.

The $2^+ \rightarrow 0^+$ transition (0.5139-MeV) rises from the Coulomb barrier, at about 8-MeV, to a plateau of about 100 mb at 18-MeV. The cross section then increases slightly with increasing proton energy to about 120 mb at 26-MeV. A plot of this transition alone, with the calculated direct excitation subtracted, is shown in Fig. III-23. It behaves in much the same way as did the 2^+ transition in ^{110}Cd and ^{114}Cd. Plotted also is the integrated (p,p') data of Rao et al.[1] at 12 and 17-MeV and Cohen et al.[14] at 16-MeV. As with ^{110}Cd and ^{114}Cd, the (p,p') data of Rao et al., at 17-MeV, is about a factor of two higher than we observe and inconsistent with the data of Cohen et al. at 16-MeV. The 0.5139-MeV transition was very difficult to separate from the 0.511-MeV annihilation peak, which was present in all runs. A systematic determination of the width of the 0.511-MeV line and its centroid was made in other runs and the results were used to constrain the fitting parameters in the 0.511-MeV portion of the doublet. Since the 0.511-MeV line was always strong and quite wide, there is substantially more error in the cross section determination for the $2^+ \rightarrow 0^+$ transition

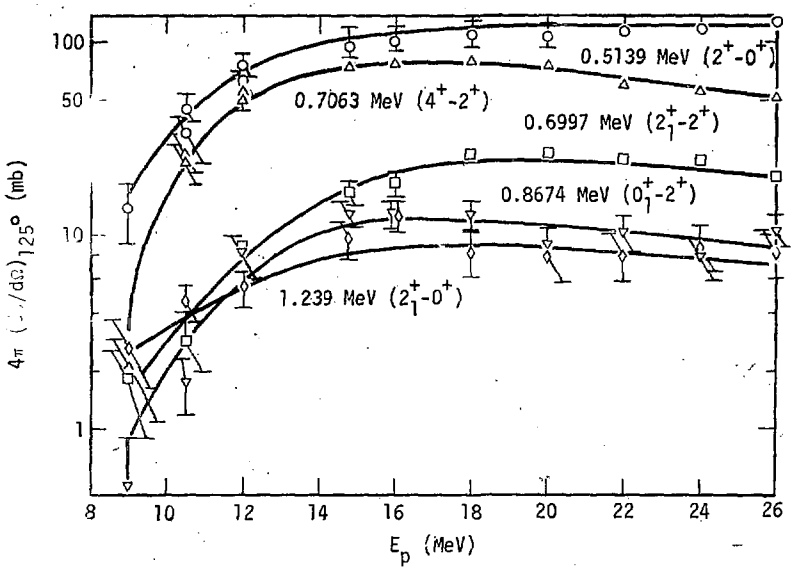

Fig. III-21. The $^{116}Cd(p,p'\gamma)$ gamma excitation functions.

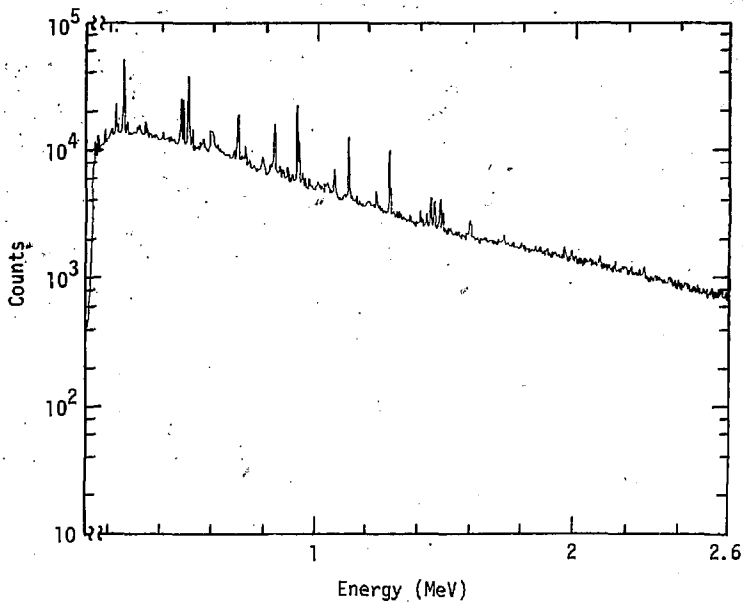

Fig. III-22. The $^{116}Cd(p,p'\gamma)$ gamma spectrum at 125° for 18 MeV protons

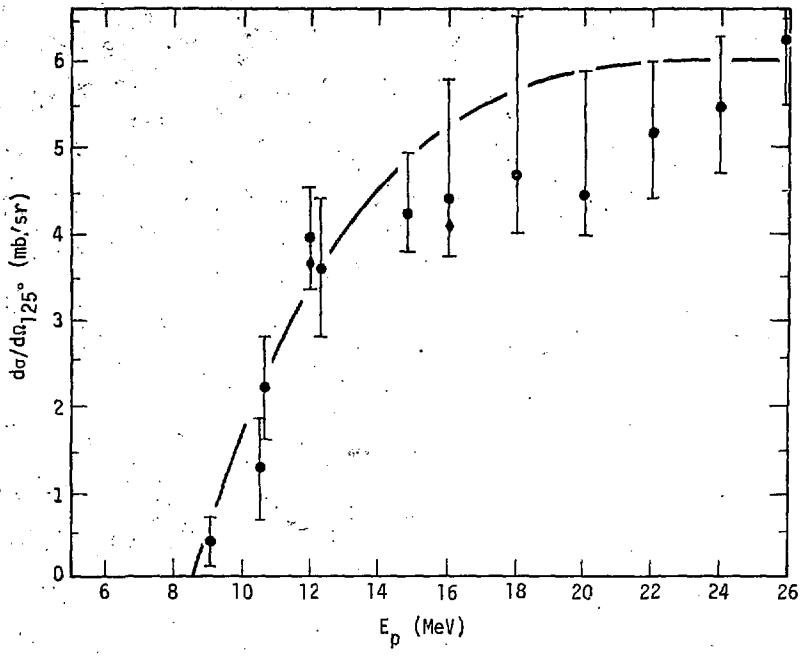

Fig. III-23. The ^{116}Cd(p,p'γ) 0.514 MeV ($2^+ \rightarrow 0^+$) gamma excitation function minus direct at 125° (Φ); proton data (Φ).

in this nucleus than in the others. In some cases (14.8 to 20-MeV) it appears that the sum of the strengths of the transition known to be feeding the first 2^+ state actually exceed the measured strength of the $2^+ \rightarrow 0^+$ transition. Since this cannot be true, it is an indication of the error involved in extracting the 0.514-MeV gamma from the 0.511-MeV. The upper limit on the error bars plotted in Fig. III-23 have been raised to include this sum.

The $4^+ \rightarrow 2^+$ transition (0.7063-MeV) is substantially stronger in this isotope than in the other Cd isotopes or Pd. It rises more sharply from the Coulomb barrier, peaking at 18-MeV at about 80 mb, and then decreasing with increasing bombarding energy. Its behavior is more like that observed in the lighter elements, Fe, Ni, and Zn, than in the heavier elements Pd, Cd, and Sn where the Coulomb barrier has more effect. This transition accounts for about 70% of the strength of the first 2^+, but as was mentioned earlier, the errors involved in the determination of the strength of the $2^+ \rightarrow 0^+$ transition make this value somewhat uncertain. For 18-MeV incident protons, the optimal angular momentum transferred is between 4 and 5 units.

The $2_1^+ \rightarrow 2^+$ transition (0.6997-MeV) behaves similarly, peaking at about 19-MeV. This transition accounts for about 20% of the strength of the first 2^+ state. The remaining 10% is accounted for by the $0_1^+ \rightarrow 2^+$ transition (0.8671-MeV). This transition behaves in a most unusual manner for a transition from a 0^+ state. It rises sharply from a very small value at low energies, to peak at about 17-MeV and then decreases with increasing energy, in much the same way that the 4^+ transition does. From this behavior, one is supicious that this transition may not be from a 0^+ state.

The $2_1^+ \rightarrow 0^+$ transition (1.2136-MeV) is generally less than 10% of the strength of the $2^+ \rightarrow 0^+$ transition. This is of the same order as we observe in ^{114}Cd and substantially larger than in ^{110}Cd.

^{116}Sn

The gamma-ray cross sections measured for this nucleus are shown in Fig. III-24. A typical $(p,p'\gamma)$ spectrum is shown in Fig. III-25. All measurements were made at 125°.

The $2^+ \rightarrow 0^+$ transition (1.2935-MeV) strength rises from the Coulomb barrier at about 8-MeV to a plateau of about 75 mb at 18-MeV. The cross section remains constant as the proton energy increases to 26-MeV. The optimum angular momentum transfer at 18-MeV is between 4 and 5 units. The largest single contributor to the 2^+ level is the decay of the 3^-, one-octupole-phonon state. This 0.973-MeV transition is an E1 transition which is probably fed by at least one other dipole transition from the continuum. The strength of the 2^+ transition with the calculated direct excitation (see Section IV-A) subtracted from it is plotted in Fig. III-26. This may be compared directly with the integrated (p,p') data of Rao[1] at 12 and 17-MeV. The gamma strength from the 2^+ is only about 2/3 of that of the integrated (p,p') cross section at 12-MeV and at 17-MeV the Rao et al.[1] cross section is larger than our values by the usual factor of two. Extracting integrated cross sections from the experimental proton data is ambigious to the extent that (p,np) and (p,2p) reactions contribute. This may account for the difference between the integrated proton data and the gamma data. The strength of the $2^+ \rightarrow 0^+$ transition in ^{116}Sn is about 30% less than it is in the Cd isotopes.

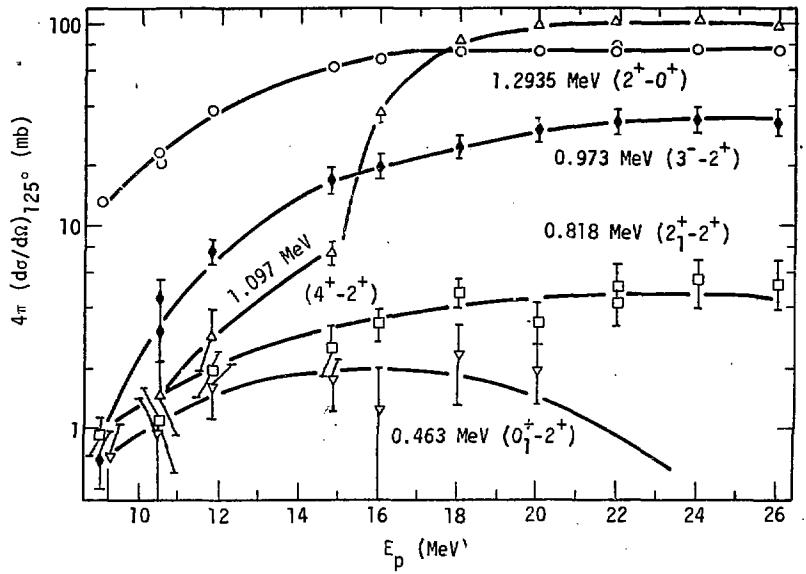

Fig. III-24. The $^{116}Sn(p,p'\gamma)$ gamma excitation functions.

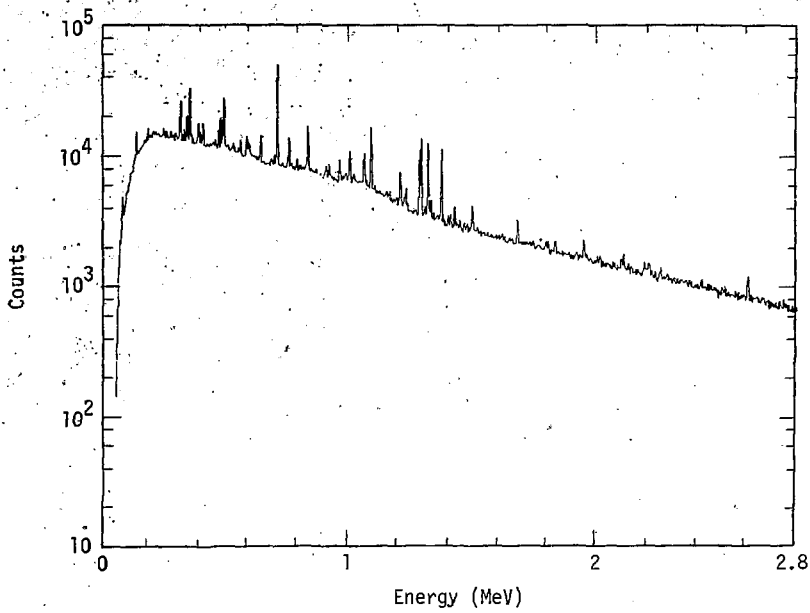

Fig. III-25. The $^{116}Sn(p,p'\gamma)$ gamma spectrum at 125° for 22 MeV protons

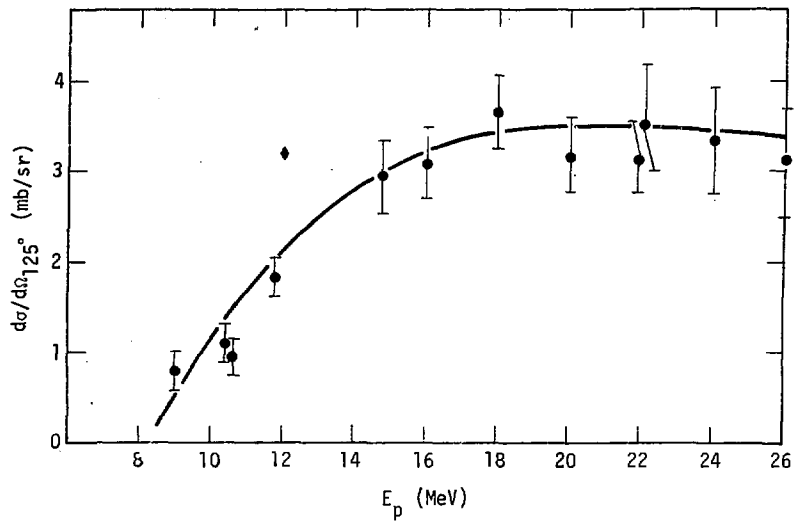

Fig. III-26. The $^{116}Sn(p,p'\gamma)$ 1.293 MeV $(2^+ \rightarrow 0^+)$ gamma excitation function minus direct at 125° (♦); proton data (♦).

The $4^+ \rightarrow 2^+$ transition (1.0975-MeV) in this nucleus is less strong than the $3^- \rightarrow 2^+$ transition. Transitions from the 3^- and 4^+ states account for 70% of the gammas feeding the first 2^+ level. An abrupt increase in the strength of the 1.0975-MeV gamma is observed, with a threshold around 14-MeV. It appears that this additional gamma strength comes from the $3/2^+ \rightarrow 5/2^+$ transition (1.098-MeV) in ^{115}Sb. The ^{116}Sn (p,2n) ^{115}Sb threshold occurs at about 13.5-MeV and the abrupt rise in strength appears to come from about this point. The 1.0975-MeV gamma line shows no apparent widening as this threshold is crossed. We therefore conclude that the difference in energy between the two gammas is much less than our nominal 3-keV resolution.

The $2_1^+ \rightarrow 2^+$ transition (0.818-MeV) behaves in much the same way as does the $2^+ \rightarrow 0^+$ transition but has less than 10% of the strength. The $0_1^+ \rightarrow 2^+$ transition (0.463-MeV) is quite weak and difficult to identify unambiguously. It disappears entirely after 20-MeV. The $2_1^+ \rightarrow 0^+$ transition (2.112-MeV) is very weak and difficult to separate from a 2.113-MeV contaminant line believed to be from ^{56}Fe. Measurements of its branching ratio indicate that it has about the same intensity as the $2_1^+ \rightarrow 2^+$ (0.818-MeV) transition.

^{120}Sn

The gamma-ray cross sections measured for this nucleus are shown in Fig. III-27 and a typical gamma spectrum is shown in Fig. III-28. All measurements on this nucleus were made at 90°. This is older and poorer quality data than have been displayed up to this point. No timing was used and no dead time correction was made. The dead time was estimated

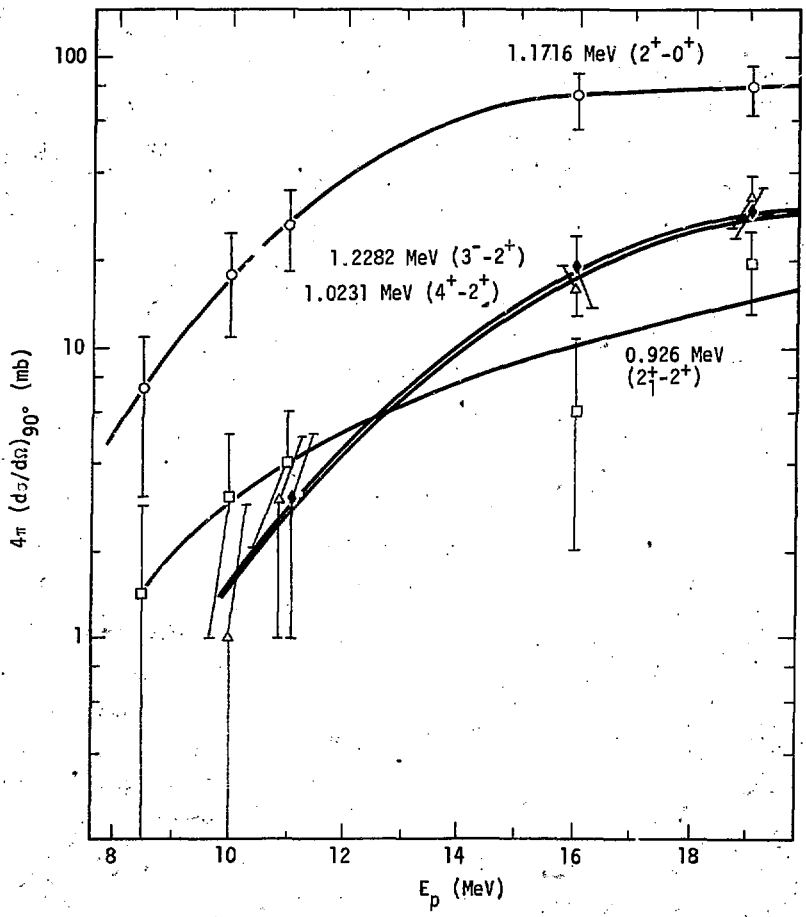

Fig. III-27. The $^{120}Sn(p,p'\gamma)$ gamma excitation functions, 1.1716 MeV (○), 1.228 MeV (●), 1.023 MeV (△), 0.926 MeV (□).

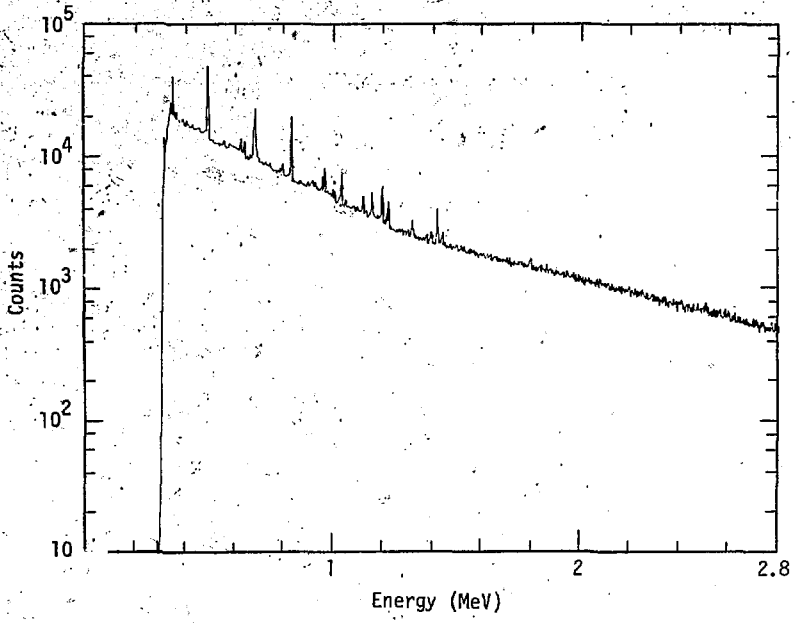

Fig. III-28. The $^{120}Sn(p,p'\gamma)$ gamma spectrum at 90° for 19 MeV protons

to be about 10% or less and will simply be included as a part of the uncertainty in the measurement. The contribution due to β decay and electron capture (EC) from $^{120}Sn(p,n)^{120}Sb$ reactions could be more important, however, and an attempt was made to correct for it.

Essentially all β decay and EC from the ground (1^+) state of ^{120}Sb goes to the ground state of ^{120}Sn. ^{120}Sb has an 8^+ isomeric state, however, which decays by EC to the 2.48-MeV (7^-) level in ^{120}Sn. This level then decays by a gamma cascade down through the first 2^+ level. One of the links in the cascade chain is a 197-keV gamma transition which could be used as a measure of this mode of decay. Unfortunately there was also a contaminant 197-keV gamma-ray observed in runs without the target. In addition, there was a low energy electronic cutoff in some of the runs so that the 197-keV transition could not be observed. The corrections were very difficult to make under these circumstances, and highly uncertain. It was decided that about 5 mb could be attributed to the EC, and this was subsequently subtracted from both the $2^+ \rightarrow 0^+$ and the $4^+ \rightarrow 2^+$ transition cross sections for incident proton energies of 10-MeV and greater. The problems which beset the analysis of this data are a good indication of why timing and pulsed beam techniques were employed in subsequent experiments.

The $2^+ \rightarrow 0^+$ transition (1.1715-MeV) rises from the Coulomb barrier at about 8-MeV to a plateau of about 75 mb at 18-MeV. This behavior is identical to that of ^{116}Sn. As with ^{116}Sn, the largest contributor to the 2^+ is the decay of the 3^-. About 4 units of angular momentum are brought in at 18-MeV. The strength of the 2^+ transition, with the calculated direct excitation subtracted from it, is plotted in Fig. III-29. This

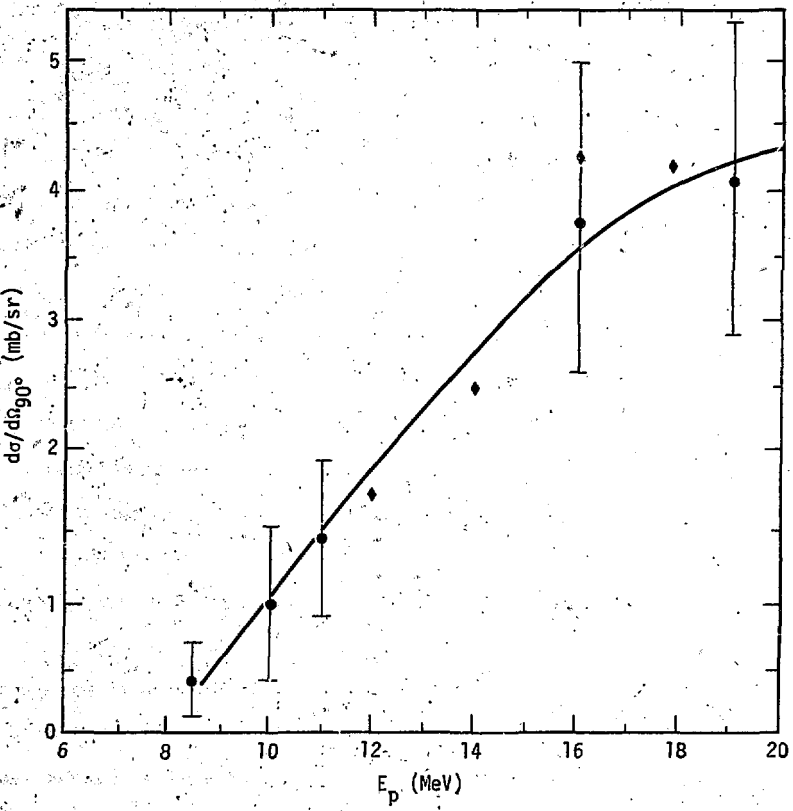

Fig. III-29. The $^{120}Sn(p,p'\gamma)$ 1.172 MeV $(2^+ \rightarrow 0^+)$ gamma excitation function minus direct at 90° (♦); integrated proton data at 75° (♦)

may be compared with the integrated (p,p') data of Kalbach[8] and Rao et al.[1] at 12, 14, 16, 17 and 17.8-MeV. The agreement between the (p,p') and the gamma data is excellent except for the Rao data at 17-MeV.

The $4^+ \rightarrow 2^+$ transition (1.0231-MeV) is essentially equal to the $3^- \rightarrow 2^+$ (1.228-MeV) transition at all energies. The 4^+ and 3^- transitions account for about 80% of the 2^+ strength at 19-MeV. At low energies (near the Coulomb barrier) the 4^+ state is excited only by EC and direct reactions and was used to help estimate the (p,n) contribution to the $2^+ \rightarrow 0^+$ cross section.

The $2_1^+ \rightarrow 2^+$ transition (0.926-MeV) behaves in much the same way as does the $2^+ \rightarrow 0^+$ transition but has only 10-20% of the strength. The $0_1^+ \rightarrow 2^+$ transition (0.7035-MeV) is very weak and somewhat obscured by an intruding neutron peak as well as having a possible contribution from EC from the 1^+ state in ^{120}Sb. Consequently, it is not shown on Fig. III-27.

^{206}Pb

This was the heaviest nucleus examined. The gamma-ray cross sections measured for this nucleus are shown in Fig. III-30. A typical gamma spectrum is shown in Fig. III-31. All measurements were made at 125°.

The $2^+ \rightarrow 0^+$ transition (0.803-MeV) rises from the Coulomb barrier at about 12-MeV to a plateau of about 70 mb. There is considerable scatter in the data, however, and the data from the two runs at 22-MeV do not overlap for this transition, though they generally do for the other transitions. Examination of the target showed that a crack had developed in the region of the beam spot. It is believed that this crack accounts for the scatter in the data. The low points would then be from the beam wandering over the crack. The cross section for the $2^+ \rightarrow 0^+$ transition with

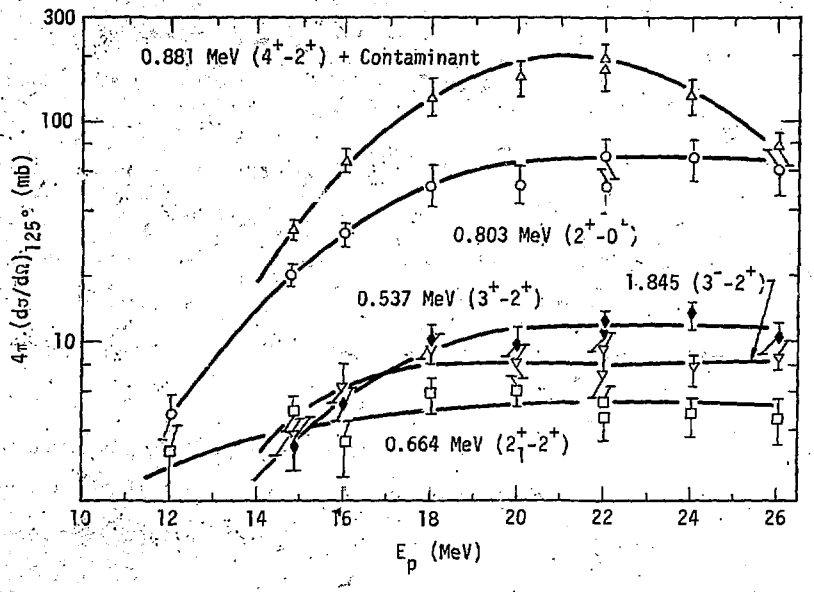

Fig. III-30. The $^{206}Pb(p,p'\gamma)$ gamma excitation functions.

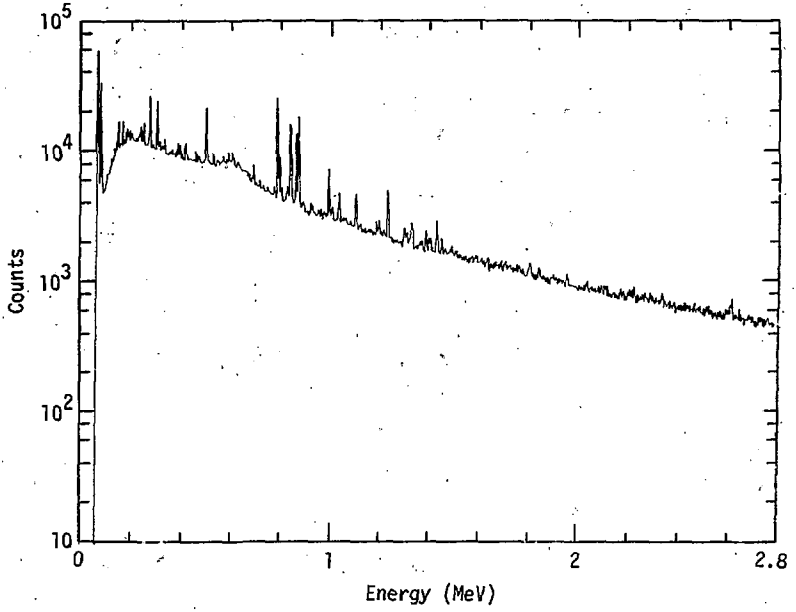

Fig. III-31. The $^{206}Pb(p,p'\gamma)$ gamma spectrum at 125° for 20 MeV protons

the calculated direct excitation subtracted from it is plotted in Fig. III-32. A thorough search of the literature failed to produce any complete (p,p') spectra or integrated cross sections for comparison with the gamma-ray data. The most apparent problem with the data is that the $4^+ \rightarrow 2^+$ transition (0.881-MeV) appears to be twice as strong as the 2^+ transition. The shape of the excitation function suggests that the problem may be an intruding gamma-ray of the same energy whose threshold is about coincident with that of the ^{206}Pb (p,2n) reaction at 11.6-MeV. A literature search of gamma-rays from ^{205}Bi failed to turn up any of exactly 0.881-MeV, however. The closest was a strong transition of 0.872-MeV, which we do observe. ^{206}Bi is also suspect since all of the data in the literature appear to have come from the β decay of the 0^+ ground state of ^{206}Po. This does not excite the higher spin states in ^{206}Bi. Since the ground state of ^{206}Bi is a 6^+ state, high spin states excited by (p,n) reactions would decay in a much different way than was observed in the β decay of ^{206}Po. A satisfactory explanation of the extra strength in the 0.881-MeV gamma-ray has yet to be found.

The two-phonon states do not stand out clearly in Pb as they have in the lighter nuclei. The next most significant transitions are the $3^- \rightarrow 2^+$ (1.8446-MeV) transition and the $3^+ \rightarrow 2^+$ (0.537-MeV) transition. The $2_1^+ \rightarrow 2^+$ (0.664-MeV) transition is somewhat lower yet. The $0_1^+ \rightarrow 2^+$ (0.362-MeV) transition is very weak, with a cross section of 1 mb or less. The $2_1^+ \rightarrow 0^+$ (1.467-MeV) transition is also weak, about 3 mb, and quite erratic. Neither of these last two transitions is plotted in Fig. III-29 because of the uncertainty in their measurement. Fig. III-33a is a summary figure showing the relative strengths of the $2^+ \rightarrow 0^+$ transitions, as a function of energy, for

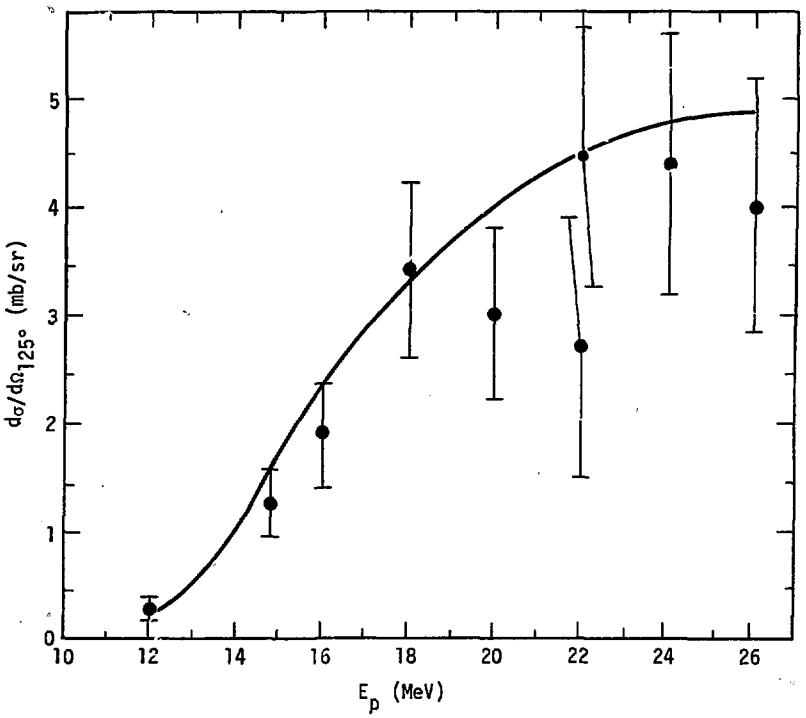

Fig. III-32. The $^{206}Pb(p,p'\gamma)$ 0.803 MeV ($2^+ \rightarrow 0^+$) gamma excitation function minus direct at 125°.

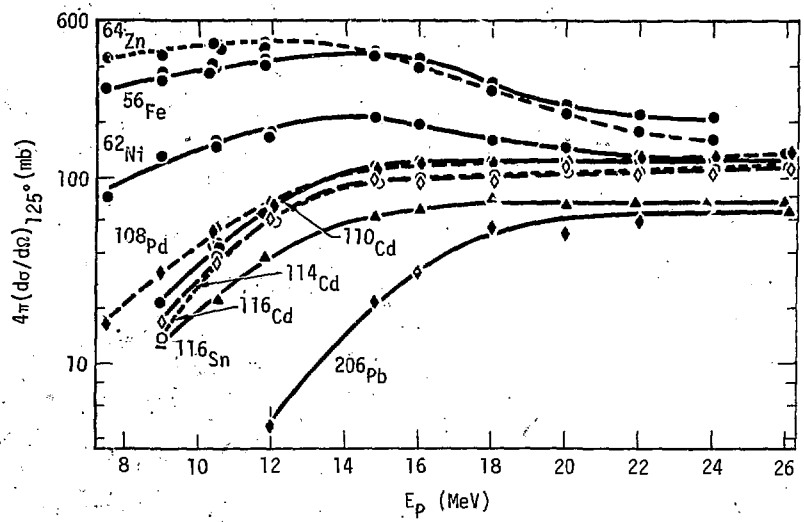

Fig. III-33a. A summary of the (p,p'γ) ($2^+ \rightarrow 0^+$) gamma transition excitation functions.

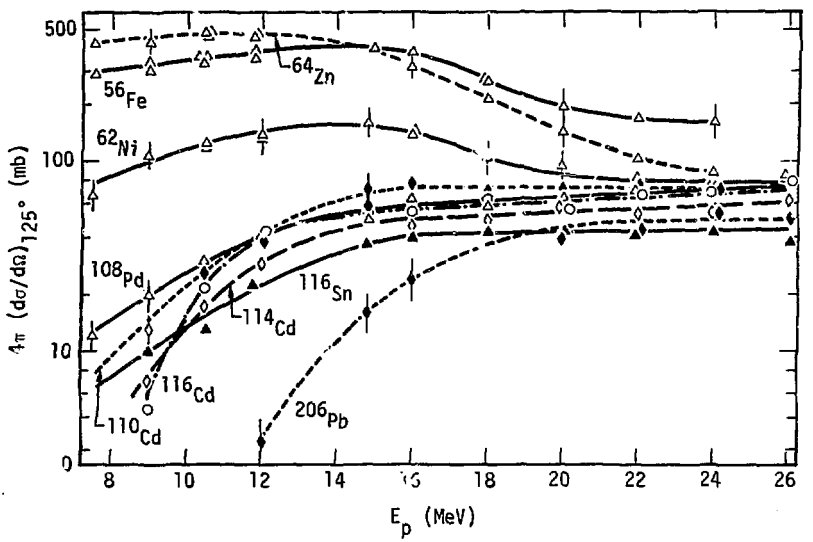

Fig. III-33b. A summary of the (p,p'γ) ($2^+ \rightarrow 0^+$) gamma transition excitation functions minus calculated direct.

all of the nuclei investigated. Fig. III-33b is similar except that the direct excitation calculated by the coupled channel code has been subtracted. The strength of the transitions systematically decreases with increasing mass of the nucleus. Because of the effect of the Coulomb barrier, the differences are greatest at low incident proton energy and become substantially smaller at high energy.

B.2 The (n,n'γ) Results

The (n,n'γ) reaction is similar to the (p,p'γ) reaction, and the discussion of the systematics of the reaction given at the beginning of Section III-B.1 is also pertinent here. The principal difference arises from the fact that the neutrons are not charged. The inelastic proton spectrum is cut off at low energies by the Coulomb barrier while the neutron spectrum is not, as can be seen from the data of Kammerdiener[24] and others[57,58] in Fig. III-34. Consequently, it is possible to observe rather clean (p,p') spectra, substantially uncontaminated by (p,2p) and (p,np) events, even when the incident energy is several MeV higher than the particle separation energy. This is not true for neutrons. When the incident neutron energy is several MeV above the neutron separation energy, as it was in these experiments, low energy neutrons from both (n,2n) events and (n,n') events are present. Consequently, the gamma data cannot be compared directly with the particle spectra as was done for the proton-induced reactions. Neutron, proton, and alpha separation energies are listed in Table III-2 for the relevant final nuclei. Neutron separation energies vary between 8 and 12-MeV for the nuclei investigated.

As was indicated by the proton experiments, the $2^+ \rightarrow 0^+$ gamma cross section is expected to be a good estimate of that portion of the inelastic neutron spectrum due to (n,n') events alone. For incident neutrons with energies below the neutron separation energy this would be essentially all of the inelastic cross section, but at 14-MeV it is only a part of it. For ^{56}Fe, for example, measurements of the

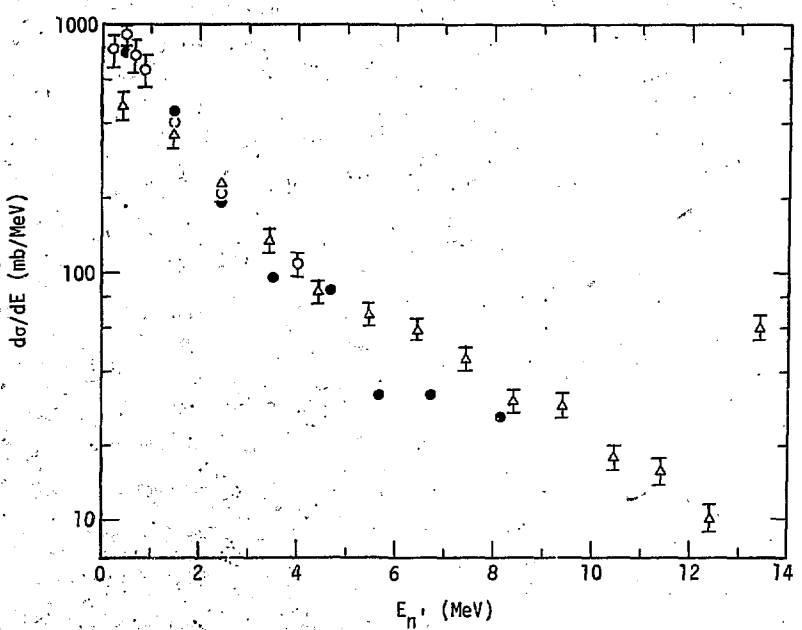

Fig. III-34. The Fe(n,n') data of Kammerdiener[24] (⋔), Mathur[58] (●), and Clayeaux & Voignier[57] (⋔), 14 MeV.

(n,2n) cross section (see Table III-5) indicate that about 60% of the non-elastic neutron production cross section is due to (n,n') events, at 14-MeV. This percentage varies considerably from nucleus to nucleus and with isotopic mass. A summary of the $(n,n'\gamma)$ data taken is given in Table III-4. Data were taken for all of the rings at about 50° and for some of them at about 80° and 124°. The data, at the various angles, are plotted in Fig. III-36, III-39, III-41, and III-43, along with experimental data from other sources. Table III-4 contains measured cross sections for all of the transitions of interest as well as coupled-channel calculations of the direct excitation of the various levels. All of the data in the table have been corrected for multiple scattering. These corrections ranged from 1% for Ni to 19% for Pb (see Table II-1).

Because of the ring geometry, changing the angle from 50° to 125° also changes the incident neutron energy from 14.8 to 13.6-MeV. In addition, there is some energy variation across the ring itself (about ± 50-keV) due to its finite angular dimension of about 3°.

If the incident particle energy is above the (n,2n) threshold, the (n,n') cross section will be reduced by the (n,2n) competition. This competition causes the (n,n') cross section to decrease rapidly with energy, just above this threshold, as the (n,2n) cross section rises rapidly. At 14-MeV, the (n,n') cross section for ^{56}Fe is still decreasing rapidly with increasing energy because of the (n,2n) threshold at 11.4 MeV. The $^{64}Zn(n,n')$ cross section behaves similarly due to an (n,2n) threshold at 12-MeV. The heavier nuclei, however, have somewhat lower (n,2n) thresholds, and it appears that the (n,2n) cross section has reached a

plateau by 14-MeV, leaving the (n,n') cross section also quite flat, at least over the few MeV of interest here. Consequently, if angular distributions are desired, it is necessary to correct the ^{56}Fe and Zn data, at different angles, to a common energy, but the Sn and ^{206}Pb data do not need such a correction for incident neutron energies around 14-MeV. The last few columns in Table III-4 give $2^+ \rightarrow 0^+$ differential cross sections corrected to 14.8-MeV, σ_{2^+}, and minus the direct contributions (statistical alone), σ_{2^+}". The last column contains the estimated percentage of direct reaction contribution to the various $2^+ \rightarrow 0^+$ transitions. The direct contribution has been calculated with the Oregon State coupled-channel code[17] and will be discussed in detail in Section IV.

Measurements of the $2_1^+ \rightarrow 0^+$ transitions were attempted, but these transitions were found to be very weak which, when combined with the low efficiency of the Ge(Li) detector for gammas of about 2-MeV, made these cross sections very difficult to determine. It appears that these cross sections are all less than 5 mb/sr.

Fe

Data for Fe were taken at about 50°, 80°, and 124°. A typical Fe (n,n'γ) spectrum for θ = 52° and 14.7-MeV incident neutrons is shown in Fig. III-35. As mentioned above, it was necessary to correct the angular distributions to a common energy. Dickens et al.[32] have made extensive (n,n'γ) measurements on Fe for 1 to 20-MeV incident neutrons. Using their data, the change in cross section as a function of neutron energy between 13.6 and 14.8-MeV was determined to be about -5.7 mb/sr MeV. This was used to correct our data to a common energy, 14.2-MeV. The corrected data were then plotted in Fig. III-36, as a

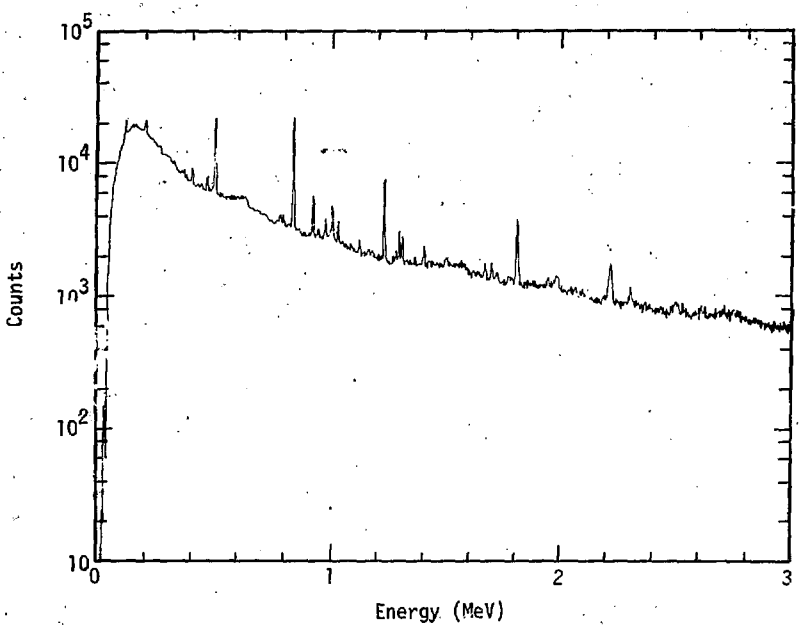

Fig. III-35. The Fe$(n,n'\gamma)$ gamma spectrum at 52° for 14.7 MeV neutrons

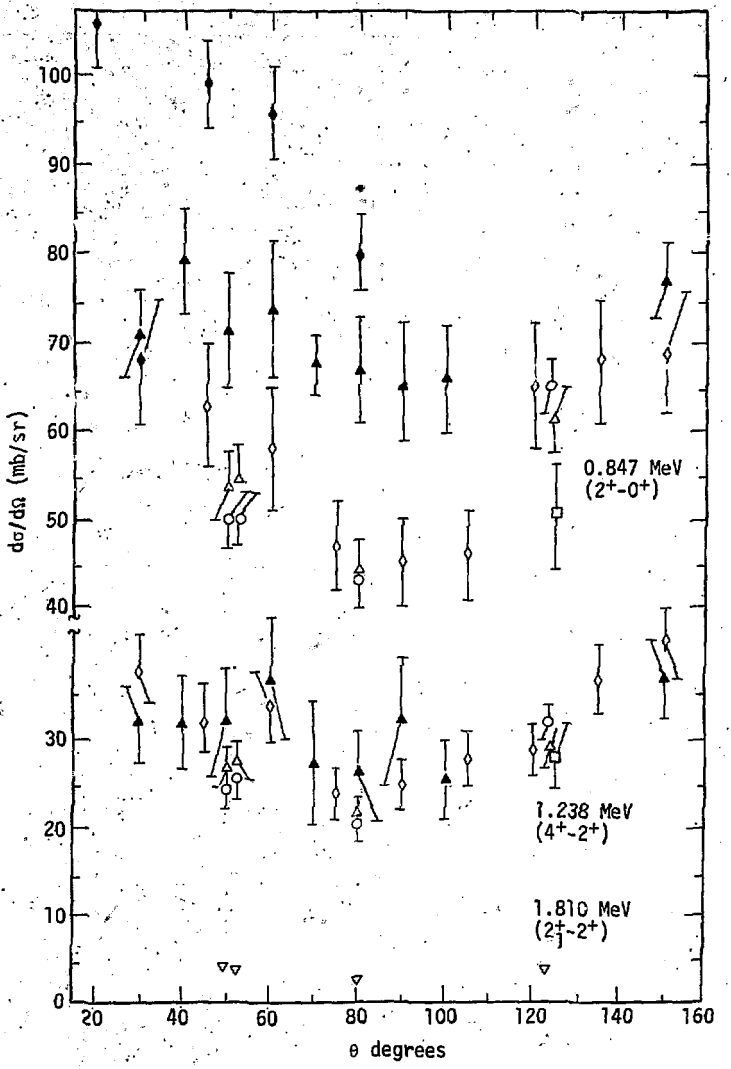

Fig. III-36. The $^{56}Fe(n,n'\gamma)$ gamma angular distributions of Lachkar[28] (▲), Abbondanno[30] (◇), Martin & Stewart[31] (◆), Dickens [32] (◇), present work (○), present work corrected to 14.2 MeV (△).

Table III - 4

A Summary of Measured (n,n'γ) Gamma Cross Sections
Corrected for Multiple Scattering, and Coupled-Channel Calculations*

$d\sigma/d\Omega$ (mb/sr)

Nucleus	θ	En (MeV)	$\sigma(2^+ \to 0^+)$	C.C Calc.	$\sigma(4^+ \to 2^+)$	C.C. Calc.	$\sigma(2_1^+ \to 2^+)$	C.C. Calc.	$\sigma(0_1^+ \to 2^+)$	C.C. Calc.	$\sigma(3^- \to 2^+)$	C.C. Calc.	$\Sigma\sigma_{direct}$*	σ_{2^+}' †	σ_{2^+}'' ††	Percent Direct
^{56}Fe	124°	13.6	65 ± 3		32 ± 2		3.4 ± 1		0		-			58 ± 4	48 ± 5	
	80°	14.3	43 ± 3	6.9	21 ± 2	0.6	2.6 ± 1	0.4	0	0.3	-	1.6	9.8 ± 2	40 ± 4	30 ± 5	
	50° 52°	14.76 14.73	50 50 ± 3		25 24 ± 2		4.1 3.8 ± 1		0		-			50 ± 4	40 ± 5	20
^{58}Ni	47°	14.8	23 ± 2		9.5 ± 1		1.7 ± 1		0		-			23 ± 2	12 ± 3	48
^{60}Ni	47°	14.8	56 ± 3				5.4 ± 1		2.8 ± 1		-			56 ± 3	45 ± 4	20
^{62}Ni	47°	14.8	>71	6.6	71 ± 8	0.6	0 ± 1	0.4	0	0.3	-	3.2	11.1 ± 2	>71	>60	<16
^{64}Zn	123°	13.6	48 ± 2		16 ± 1		11 ± 1		0		-			44 ± 3	29 ± 4	
	49°	14.8	40 ± 2	8.4	13 ± 1	0.9	7 ± 1	0.7	.5 ± .3	0.5	-	4.3	14.8 ± 2	40 ± 2	25 ± 3	37
^{66}Zn	123°	13.6	80 ± 3		30 ± 2		20 ± 2		5.2 ± 2		7.6 ± 2			76 ± 4	61 ± 5	
	49°	14.8	70 ± 3		25 ± 2		15 ± 2		11 ± 2		5.6 ± 2			70 ± 3	55 ± 4	21
^{110}Cd	49°	14.8	149 ± 6		75 ± 4		8.6 ± 2		0		-			149 ± 6	131 ± 7	12
^{112}Cd	49°	14.8	114 ± 6		59 ± 3		7.4 ± 2		7.9 ± 1		-			114 ± 6	96 ± 4	16

Table III - 4 (continued)

Nucleus	θ	En	$\sigma(2^+ \to 0^+)$	c.c. Calc.	$\sigma(4^+ \to 2^+)$	c.c. Calc.	$\sigma(2_1^+ \to 2^+)$	c.c. Calc.	$\sigma(0_1^+ \to 2^+)$	c.c. Calc.	$\sigma(3^- \to 2^+)$	c.c. Calc.	$\Sigma\sigma_{direct}$*	σ'_{2^+} †	σ''_{2^+} ††	Percent Direct
^{114}Cd	49°	14.8	45 ± 3	10.7	12 ± 2	2.0	10 ± 1	0.7	7.0 ± 2	0.4	-	4.3	18.1 ± 2	45 ± 3	27 ± 4	40
^{116}Cd	49°	14.8	38 ± 12		35 ± 7		1.8 ± 6		0		-			38 ± 12	20 ± 13	48
^{116}Sn	-123°	13.6	79 ± 5		31 ± 4		0 ± 1		0		23 ± 4			80 ± 5	68 ± 6	
	78°	14.3	55 ± 5	4.1	26 ± 4		6.1 ± 4		0		30 ± 4	5.8	~12 ± 3	55 ± 5	43 ± 6	
	51°	14.8	87 ± 5		32 ± 4		0 ± 1		0		20 ± 4			87 ± 5	75 ± 6	14
^{118}Sn	123°	13.6	62 ± 4		20 ± 4		3.6 ± 4		0		0 ± 2			62 ± 4	50 ± 5	
	78°	14.3	55 ± 4		17 ± 3		6.9 ± 2		0		2.5 ± 2			55 ± 3	43 ± 4	
	51°	14.8	64 ± 4		22 ± 2		0 ± 1		2.6 ± 1		3.6 ± 2			65 ± 3	53 ± 4	18
^{120}Sn	123°	13.6	28 ± 3		18 ± 2		0 ± 1		3.6 ± 2		12 ± 3			28 ± 3	16 ± 4	
	78°	14.3	24 ± 3		13 ± 2		6.3 ± 2		4.2 ± 2		8.0 ± 2			24 ± 2	12 ± 3	
	51°	14.8	31 ± 3		14 ± 2		3.3 ± 1		1.1 ± 2		8.7 ± 2			30 ± 3	18 ± 4	40
^{206}Pb	126°	13.6	88 ± 5		15 ± 1		9.5 ± 1		0 ± 1		-			88 ± 5	80 ± 6	
	78°	14.3	69 ± 5	2.1	14 ± 1	0.5	7.8 ± 1	0.1	0 ± 1	0.1	-	5.7	8.5 ± 2	69 ± 5	61 ± 6	
	46°	14.8	82 ± 5		17 1		5.7 ± 1		0 ± 1		-			82 ± 5	74 ± 6	10

*The c.c. calculated direct differential cross section, $d\sigma_I/d\Omega$, is actually $\sigma_I/4\pi$

† $\sigma'_{2^+} = \sigma_{2^+}$ corrected to 14.8 MeV

†† $\sigma''_{2^+} = \sigma'_{2^+} - \Sigma\sigma_{direct}$

function of angle, along with data from a number of other investigators.[28,30,31,32] There are substantial variations in both the angular distributions and the absolute cross sections determined by the various experimenters for the 0.847-MeV, $2^+ \rightarrow 0^+$ transition. Our data seem to agree quite well with those of Abbondanno et al.[30] and to be in substantial disagreement with the data of Lachkar et al.[28] and Martin and Stewart.[31] It appears that our correction to the cross section for energy variation with angle is not quite large enough, in that symmetry about 90° has been only marginally achieved, and our data point at 124° is somewhat higher than that of Dickens et al.[32]

The angular distribution of the 1.238-MeV, $4^+ \rightarrow 2^+$ transition appears to be somewhat flatter than that for the 0.847-MeV, $2^+ \rightarrow 0^+$ transition. The $4^+ \rightarrow 2^+$ data agree with those of Abbondanno et al.[30] and Lachkar.[28] Dickens'[32] point at 125° is also in excellent agreement with our data. The data have been corrected for multiple scattering, which is about a 10% effect for the Fe ring.

To obtain the total cross section from an angular distribution, one can least-squares-fit a series of Legendre polynomials to the data and integrate the resulting series over angle. For nuclear reactions which proceed through a state of well-defined parity, the angular distribution will be symmetric about 90° and will consequently be described by even Legendre polynomials.[29] If such a fit is made to the Abbondanno[30] data, the result is

$$\left.\frac{d\sigma}{d\Omega}\right|_{0.847} = 57.21\ (1 + 0.313\ P_2 - 0.230\ P_4)$$

This is somewhat different than the fit they make and yields a lower chi-square. If this function is integrated over solid angle, the P_2 and P_4 terms integrate to zero leaving only the constant term. The result is

$$\sigma_{0.847} = 4\pi \times 57.21 = 719 \text{ mb}$$

At $\theta = 125°$, the differential cross section is

$$\left.\frac{d\sigma}{d\Omega}\right|_{0.847}^{125°} = 57.21 \times 1.09 = 62.1 \text{ mb/sr}$$

Thus if the differential cross section measured at 125° were to simply be multiplied by 4π to yield an "integrated" cross section, the result would be 9% too large, because of the P_4 term. At 125° the P_2 term is essentially zero and the P_4 term is the only angle dependent contributor to the cross section. This term is small and somewhat uncertain at this angle, since the angular distribution tends to be dominated by the P_2 term. The P_4 coefficients determined by Lachkar et al.[28] and Martin and Stewart[31] are substantially less than that determined by Abboudanno et al.[30] and would induce errors of 4% or less in a cross section determined at 125°.

Although a complete statistical-model analysis of the angular distribution, which includes the effects of unobserved gammas in the cascade, has not been carried out, the overall shapes of these distributions are expected to be related to those observed at low energies without unobserved intermediate transitions. The review article by E. Sheldon and D. M. Van Patter[29] contains examples of these and sets forth a means of calculating them. The anisotropy at 14-MeV is in fact smaller than that observed at lower bombarding energies, probably because of the intermediate, unobserved radiations.

In general, then, one would not anticipate a large error (greater than 10%) from using $4\pi(d\sigma/d\Omega)_{125°}$ as an estimate of the integrated cross section at 14-MeV. It should be noted that the differential cross section at 55° should be identical to that at 125° for angular distributions which are symmetric about 90°. Most of our data was taken at about 50°, however, which introduces a slight additional error (not exceeding 5%) if this value is multiplied by 4π and used as a total cross section.

Ni

Ni data were taken only at 47°. A summary of the measured gamma cross sections is given in Table III-4 for the isotopes ^{58}Ni, ^{60}Ni, and ^{62}Ni, which constitute 67.9%, 26.2%, and 3.7%, respectively, of natural nickel. A typical (n,n'γ) spectrum from Ni is shown in Fig. IV-37. The 1.173-MeV ($2^+ \rightarrow 0^+$) transition in ^{62}Ni forms an unresolved doublet with the 1.173-MeV ($4^+ \rightarrow 2^+$) transition in ^{60}Ni. According to a previous measurement[39], the ^{62}Ni (n,n') cross section at 15.1-MeV is 75 $\pm$ 19 mb/sr. This is consistent with our observation that the $4^+ \rightarrow 2^+$ transition cross section in ^{62}Ni is about 71 mb/sr and is generally the principal contributor to the $2^+ \rightarrow 0^+$ strength. It can be concluded only that the $2^+ \rightarrow 0^+$ cross section in ^{62}Ni is larger than 71 mb/sr.

The 2^+ cross section increases from 23 mb/sr for ^{58}Ni to about 75 mb/sr for ^{62}Ni at 14.8-MeV. This effect is probably due to differences in neutron and proton separation energies among the various isotopes. From Table III-2 we see that the proton separation energy for ^{58}Ni is only 8.2-MeV, some 4-MeV lower than the neutron separation energy. As the isotopic mass increases, the proton separation energy increases to 11.1-MeV, nearly equal to the neutron separation energy for ^{62}Ni. This increase in proton separation energy causes more

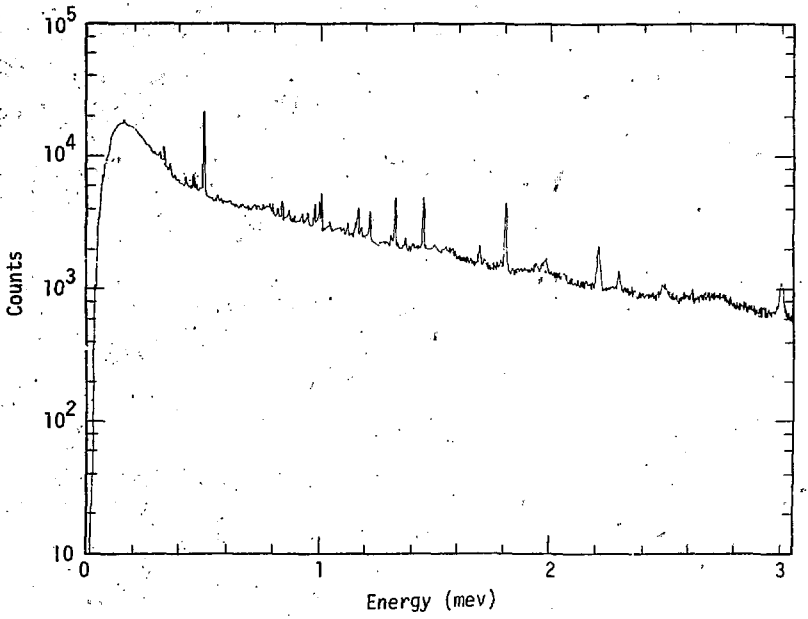

Fig. III-37. The Ni(n,n'γ) gamma spectrum at 47° for 14.8 MeV neutrons

of the non-elastic events to be (n,n') rather than (n,n'p) and hence the increasing (n,n'γ) cross section with increasing A. The same effect is observed for the Zn isotopes. For incident protons on the same nuclei, Rao et al.[1] have observed that the (p,p') cross sections go down with increasing isotopic mass, in contrast to the (n,n') cross sections.

The Ni data have been corrected for multiple scattering, which is only a 2% effect for the Ni ring. Zn shows the same behavior with isotopic mass as does Ni. Hence the 2^+ cross section at 14.8-MeV increases from 40 mb/sr for ^{64}Zn to 70 mb/sr for ^{66}Zn. As with Ni the proton separation energy for ^{64}Zn is small, only 7.7-MeV, substantially less than the neutron separation energy. The proton separation energy increases with isotopic mass, and we presume that this causes a larger (n,n'γ) contribution to the non-elastic cross section.

Zn

A typical (n,n'γ) spectrum for Zn is shown in Fig. III-38. The Zn data are plotted in Fig. III-39. Since the data were taken only at 49° and 123°, it is not possible to get any idea of what the angular distribution is like. The data do show that the cross section is changing rapidly with energy around 14-MeV, however. The cross section drops 8-10 mb/sr as the neutron energy changes from 13.6 to 14.8-MeV, assuming that the angular distribution is symmetric about 90°. The Zn data have been corrected for multiple scattering, which is about a 7% effect.

Cd

The Cd data were taken only at 49°. A summary of the measured gamma cross sections is given in Table III-4 for the isotopes ^{110}Cd, ^{112}Cd, ^{114}Cd, and ^{116}Cd which constitute 12.4%, 24.09%, 28.8%, and 7.6%, respectively,

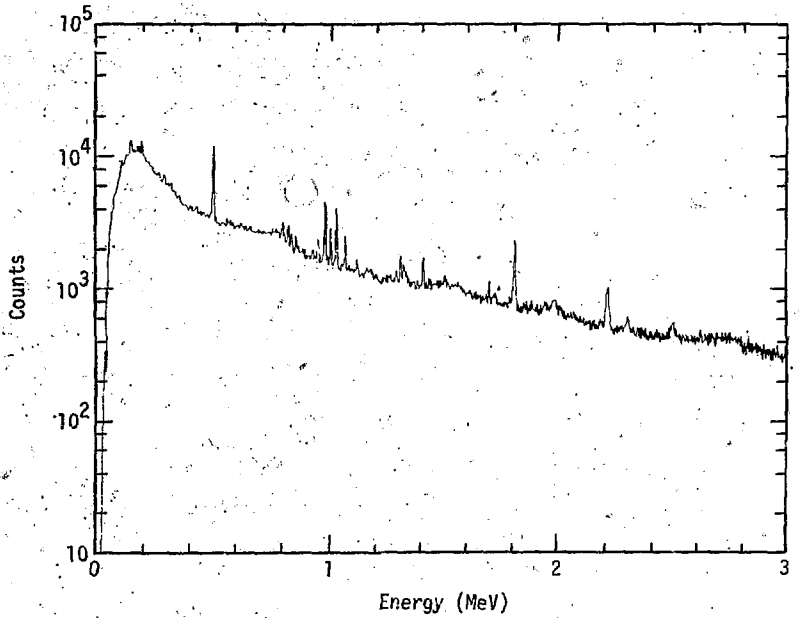

Fig. III-38. The Zn(n,n'γ) gamma spectrum at 49° for 14.8 MeV neutrons

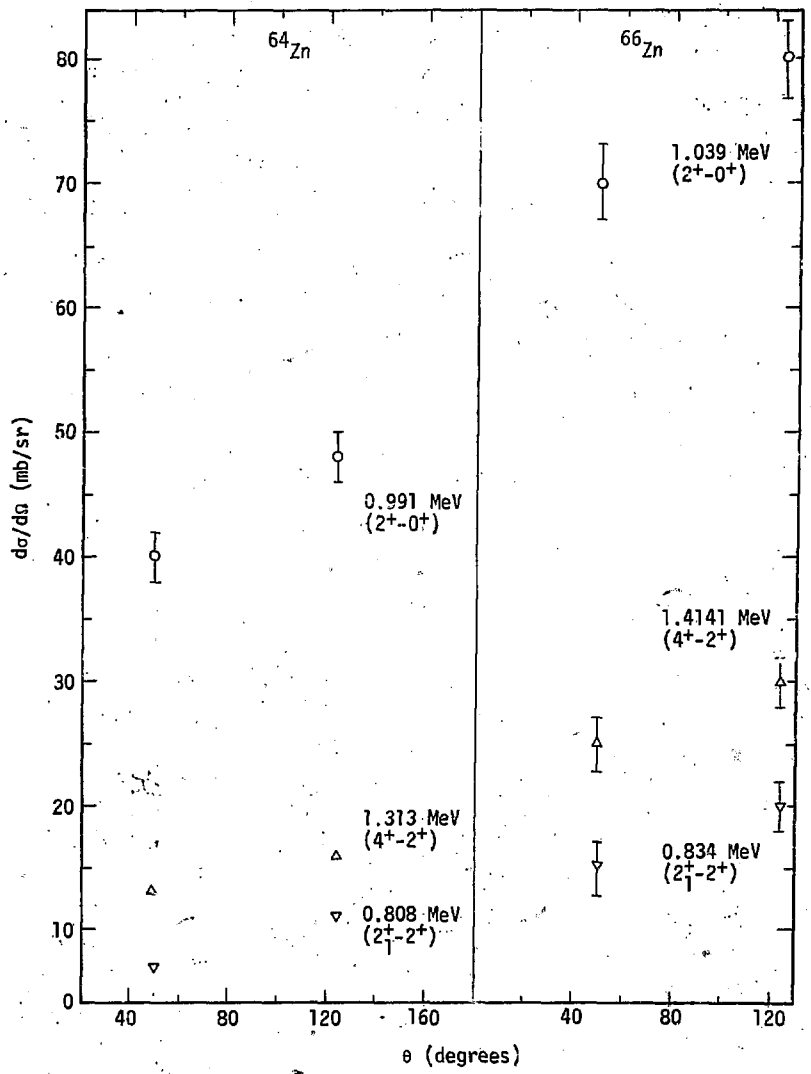

Fig. III-39. The Zn(n,n'γ) gamma angular distribution at 14 MeV.

of natural cadmium. A typical Cd(n,n'γ) spectrum is shown in Fig. III-40.

The $2^+ \rightarrow 0^+$ cross section decreases from 149 mb/sr for ^{110}Cd to 30 mb/sr for ^{116}Cd at 14.8-MeV. If only that part of the differential cross section which we estimate to be due to statistical processes, σ_{2^+}'', is considered, then the effect is even more significant, decreasing from 131 mb/sr for ^{110}Cd to only 20 mb/sr for ^{116}Cd. The cross section attributable to direct processes, given in the last column of Table III-4 as a percentage of the total (n,n') cross section, increases to about one-half of the total (n,n') cross section for ^{116}Cd. Rao et al.[1] have attributed all of the (p,p') cross section for ^{116}Cd and other heavy isotopes, which decay predominantly by neutron emission, to direct reactions. The coupled-channel approach puts most of the direct reaction strength into the one-quadrupole-phonon and one-octupole-phonon vibrational excitations (see Section IV-A). These have been included in our calculations along with the two-quadrupole-phonon excitations. If the collective picture of direct excitation is correct this should account for most of the direct excitation cross section. Thus, it would appear that even the heavy isotopes make a significant amount of statistical-type (compound plus pre-equilibrium) reaction contribution to the total (n,n') cross section at 14-MeV. The (p,p') results support this conclusion. The direct processes make up an increasingly larger percentage of the total (n,n') cross section as the isotopic mass increases, but do not account for all of it.

Sn

The Sn data were taken at three angles, 51°, 78°, and 123°. The data are listed in Table III-4 and plotted in Fig. III-41. A typical Sn(n,n'γ) spectrum for 14.8-MeV incident neutrons at 51° is shown in

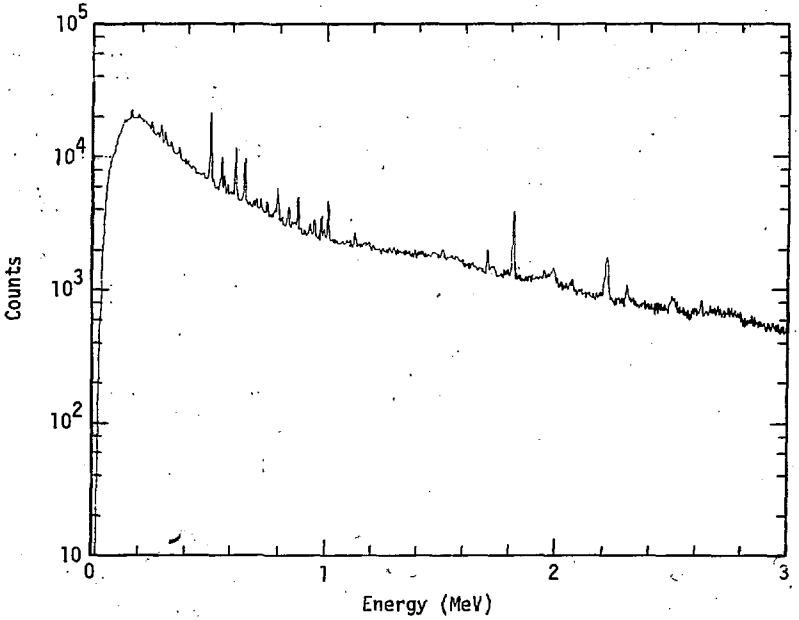

Fig. III-40. The Cd(n,n'γ) gamma spectrum at 49° for 14.8 MeV neutrons

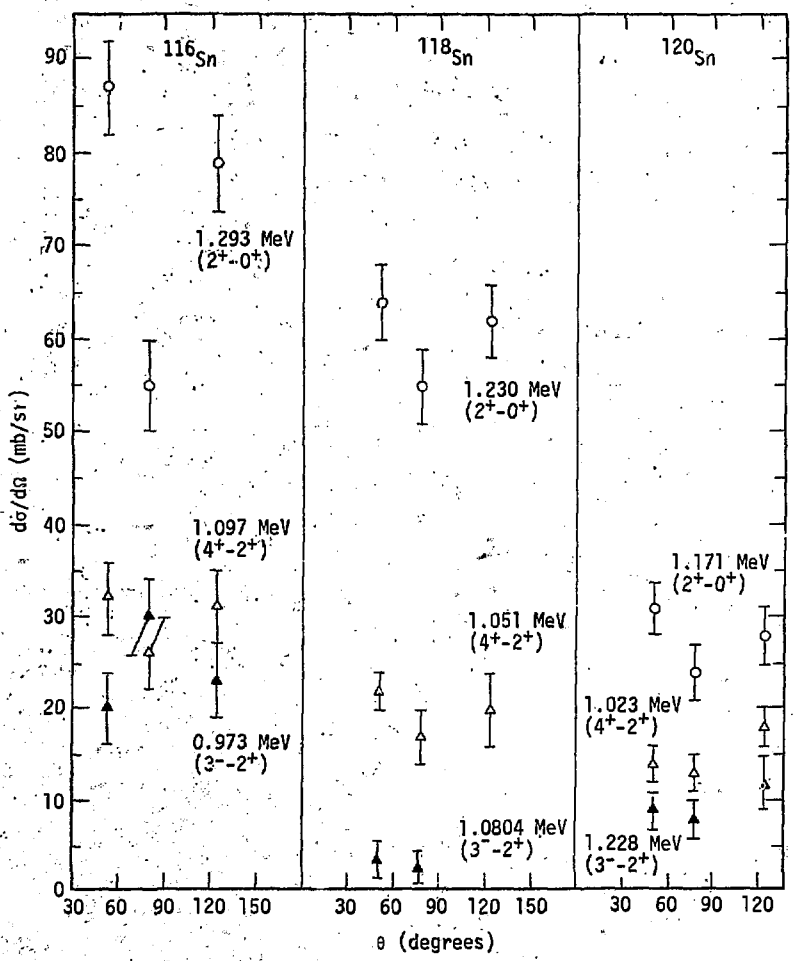

Fig. III-41. The Sn(n,n'γ) gamma angular distribution for 14 MeV neutrons.

Fig. III-42. As with Cd, the Sn(n,n'γ) cross section decreases rapidly with isotopic mass, from 87 mb/sr for ^{116}Sn to 31 mb/sr for ^{120}Sn. The estimated fraction of the cross section due to direct excitation increases with isotopic mass, rising from about 14% for ^{116}Sn to 40% for ^{120}Sn.

The angular distribution of the ^{116}Sn data is more anisotropic than that of the other isotopes, ^{118}Sn and ^{120}Sn, or any of the other nuclei investigated. All of the angular distributions are consistent with symmetry about 90°, and there is no indication from either the (n,n'γ) or the (p,p'γ) data that the cross section varies by more than 10% between 13.6 to 14.8-MeV. The data have been corrected for multiple scattering, which is about a 5% effect for the Sn ring.

Pb

The ^{206}Pb data are plotted in Fig. III-43. As with Sn, there is no indication, from either the (p,p') or (n,n') data, of a large change in the (n,n') cross section in the energy region between 13.6 and 14.8-MeV. Consequently, no correction for energy was made to the data. A typical (n,n'γ) spectrum for 14.8-MeV and θ = 46° is shown in Fig. III-44. Since the Pb ring was larger than the others and because of the high density of Pb, multiple scattering was a more significant problem. Monte Carlo calculations indicated that a 19% multiple scattering correction was necessary. Sheldon and Van Patter[29] present Pb(n,n'γ) data with an angular distribution, at 4.1-MeV, given by

$$\frac{d\sigma}{d\Omega} = C\ (1 + 0.1431\ P_2 - 0.0368\ P_4)\ .$$

This distribution is plotted in Fig. III-43 with arbitrary normalization, and though it appears to be somewhat less anisoptropic than our data, the two are not really inconsistent. The P_4 term contributes only 1% to the

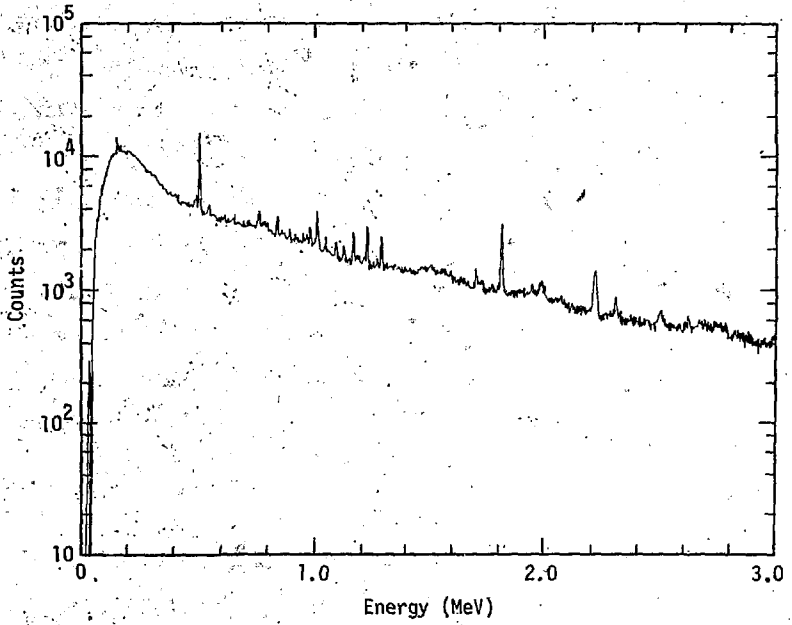

Fig. III-42. The Sn(n,n'γ) gamma spectrum at 51° for 14.8 MeV neutrons

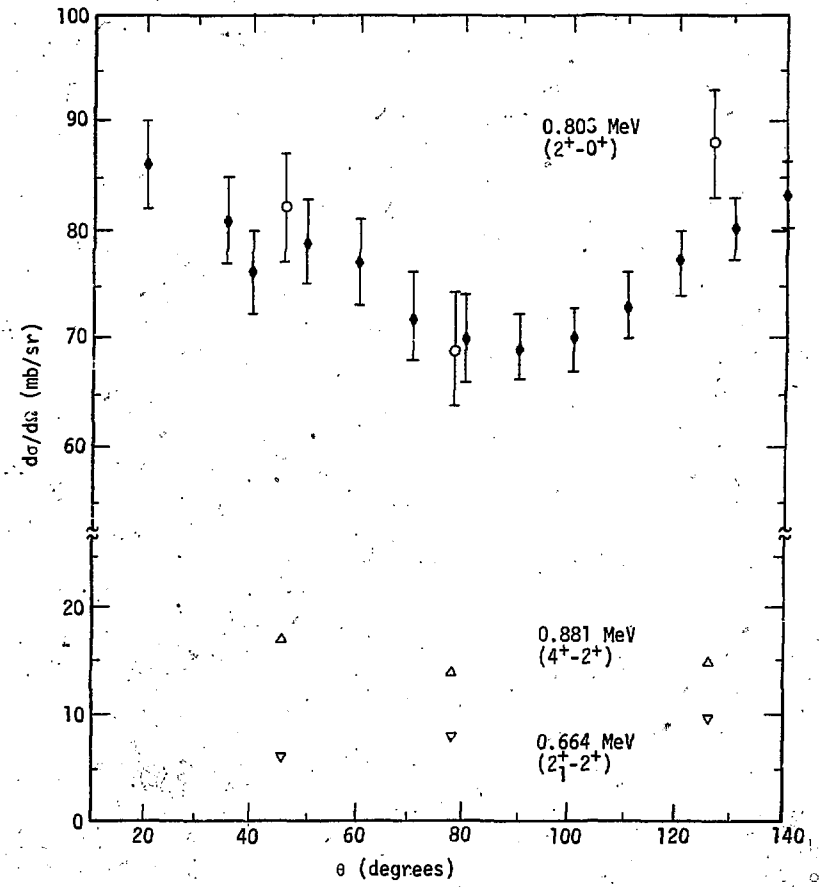

Fig. III-43. The $^{206}Pb(n,n'\gamma)$ gamma angular distributions at 14 MeV (○△▽), Sheldon & Van Patter[29] at 4.1 MeV, arbitrary normalization (◐).

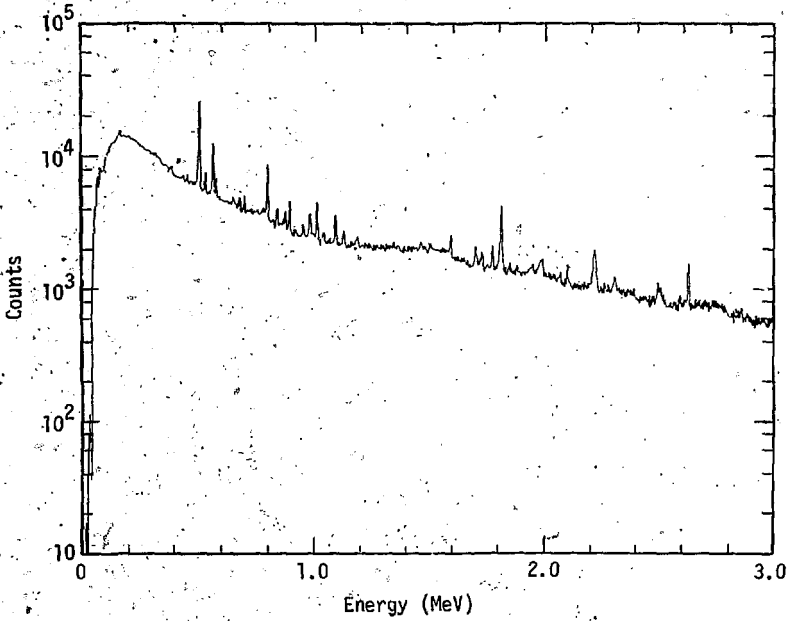

Fig. III-44. The Pb(n,n'γ) gamma spectrum at 46° for 14.8 MeV neutrons

cross section at 125° for this angular distribution. Direct excitation is not very significant, contributing only about 10% at 14.8-MeV, according to coupled-channel calculations.

The $(2^+ \rightarrow 0^+)$ gamma cross sections are also interesting because of the information that may be inferred from them about (n,n') cross sections. Table III-5 lists the $(2^+ \rightarrow 0^+)$ gamma cross sections, $\sigma(2^+ \rightarrow 0^+) = 4\pi(d\sigma/d\Omega)_{50°}$, and a series of neutron cross sections compiled from UCRL-50400, Vol. 8, Rev. 1 and ANL/NDM-11. These cross sections were evaluated at 14.8-MeV, when possible, except for Fe, which was evaluated at 14.2-MeV. The intent of the table is to compare the gamma cross section, $\sigma(2^+ \rightarrow 0^+)$, with an estimate of the (n,n') cross section drawn from the neutron measurements. In a few cases, other estimates of the (n,n') cross section have been made or inferred from gamma measurements or neutron data. These are listed in the third column under $\sigma(n,n')$. The agreement with our gamma data is fairly good except in the case of Cd. In order to estimate the (n,n') cross sections for comparison with the gamma data, it is necessary to extract the non-elastic scattering cross section, $\sigma_{\text{non el}}$, and subtract the cross sections for all competing reactions from it. This can be done only if all significant competing reactions and their cross sections are known accurately. The non-elastic cross sections compare favorably with the compound nucleus formation cross sections, σ_{cn}^{LOKI}, calculated with the optical model code LOKI,[34] using Wilmore-Hodgson[20] neutron parameters. At 14-MeV, the (n,2n) reaction is generally the only significant competitor with the (n,n') reaction, except for the lighter nuclei, especially Ni, where the production of charged particles is also significant.

Values for the cross sections for the production of protons and alphas, also taken from UCRL-50400, are listed under the headings $\sigma(n,x)p$ and $\sigma(n,x)\alpha$, respectively, in Table III-5. In the last column, the cross sections for all competing reactions are subtracted from $\sigma_{non.el}$, leaving an estimate of $\sigma(n,n')$ which can be compared with the gamma cross sections, $\sigma(2^+ \rightarrow 0^+)$. Within the uncertainties of the cross sections, the (n,n') estimates and the gamma measurements generally agree. However, the uncertainties are often large, and there are a few significant exceptions. The agreement is good for Fe, Ni, Zn and Sn, but Cd, particularly ^{110}Cd, and ^{206}Pb show serious discrepancies. Since the (n,2n) reaction is the only significant competitor with the (n,n') reaction at this energy and for these nuclei, the observed discrepancy indicates a problem with either the (n,2n) cross section or the gamma data. It is our conclusion that the (n,2n) cross sections for natural Cd, ^{110}Cd, natural Pb, and ^{206}Pb should be re-examined.

Table III - 5

A Comparison of the $(2^+ \rightarrow 0^+)$ Gamma Cross Section with Available Experimental Neutron Data[59,60] at 14-MeV

σ(mb)

Nucleus	$\sigma\left(2^+ \rightarrow 0^+\right)$	$\sigma_{(n,n')}$	$\sigma_{non\ el}$	σ_{CN}^{LOKI}	$\sigma_{(n,2n)}$	$\sigma_{(n,x)p}$	$\sigma_{(n,x)\alpha}$	$\sigma_{non}-\Sigma\sigma_i$
^{56}Fe	720 ± 60	660 ± 80		1396	440 ± 90	144 ± 12	2	774 ± 95
Nat Fe	~720	527 ± 53	1360 ± 30	1396	460 ± 40			754 ± 50
^{58}Ni	290 ± 25	360 ± 60		1409	35 ± 10	840 ± 60	125 ± 60	380 ± 90
^{60}Ni	700 ± 38	880 ± 130		1435	380	180 ± 12	78	742 ± 50
^{62}Ni	>890	940 ± 240		1465	~400	18 ± 2	17 ± 4	945 ± 60
Nat Ni	~420	~400	1380 ± 30	1418	140 ± 10	670 ± 50	139	431 ± 60
^{64}Zn	500 ± 25			1484	225 ± 25	590 ± 75	168 ± 16	597 ± 90
^{66}Zn	880 ± 25			1505	580 ± 50	117 ± 12	-	883 ± 60
Nat Zn	~640	470 ± 220	1580 ± 30	1492	550 ± 50	~420	~80	530 ± 70
^{110}Cd	1870 ± 75			1861	998 ± 115	27 ± 5	-	885 ± 120
^{112}Cd	1430 ± 75			1870	650 ± 40	19	4	1237 ± 60
^{114}Cd	565 ± 38			1880	-	~7	1	-
^{116}Cd	477 ± 150			1890	1650 ± 100	2	1	257 ± 110

Table III - 5 (continued)

Nucleus	$\sigma\left(2^+ \to 0^+\right)$	$\sigma_{(n,n')}$	$\sigma_{non\ el}$	σ_{CN}^{LOKI}	$\sigma_{(n,2n)}$	$\sigma_{(n,x)p}$	$\sigma_{(n,x)\alpha}$	$\sigma_{non}-\Sigma\sigma_i$
Nat Cd	~1063	250	1910 ± 40	1875	1580	14	-	316 ± 200
^{116}Sn	1090 ± 63			1890	-	22 ± 5	-	-
^{118}Sn	800 ± 50			1907	976 ± 120	12 ± 1	1	1040 ± 145
^{120}Sn	390 ± 38			1913	1444 ± 210	5 ± 1	-	581 ± 225
Nat Sn	~670		2030 ± 80	1904	1500	15	-	515 ± 200
^{206}Pb	1030 ± 63			2500	866 ± 77	-	1	1633 ± 90
^{208}Pb	~400*			2509	990 ± 120	1	2	1507 ± 130
Nat Pb	~600	460 ± 70 721 ± 94	2500 ± 50	2506	2240 ± 170	-	~2	258 ± 180

* $\sigma\left(3^- \to 0^+\right)$ not $\sigma\left(2^+ \to 0^+\right)$

IV. Computer Calculations and Models

A. Coupled-Channel Calculations

The direct, collective excitation of the spherical, even-even nuclei studied constitutes an important part of the nuclear reaction process and affects the gamma spectra in a fundamentally different way than it does the particle spectra. Direct, collective excitation is most important for the simple, low-lying collective levels found in vibrational and rotational nuclei. The scattered proton and neutron spectra from these direct reactions consist of strong, high energy peaks which are, in general, easily separable from the continuous, smoothly varying, and lower energy part of the spectrum due primarily to statistical reactions. These direct reactions were not included in the integrated proton spectra which were compared with the gamma data.

In the gamma spectra, direct excitation of the low-lying collective levels generally results in a decay of the first 2^+ level and contributes significantly to the total $2^+ \rightarrow 0^+$ gamma cross section. The coupled-channel calculations were performed to determine the direct contribution to the gamma cross section, so that it might be compared directly with the integrated particle spectra, and also to examine the contribution of the direct, collective reaction to the total inelastic scattering cross section as a function of incident particle energy.

The coupled-channel calculations were performed with the Oregon State Coupled-Channel Code.[17,56] This code is based on the coupled-channel formalism discussed by Tamura[18] and Madsen.[56] The strongly collective nature of the low-lying levels in even-even nuclei implies a strong coupling between the excited state and ground state channels in the reaction

process. The collective motions can be described by a hydrodynamic vibrating-drop model, with the coupling between the different channels derived explicitly in terms of an optical model with deformations which follow the shape vibrations of the liquid drop. Such a collective-model description of the interaction is assumed in the present work; however, the code also contains a microscopic model description of the nuclear levels and the interaction in terms of single particle states.

Because of the coupling of the various levels, the Schrodinger equation, which describes the scattering, becomes a set of coupled differential equations. The interaction is described by an optical model potential which is complex and includes the spin-orbit interaction as well as the Coulomb interaction. The radial dependence of the nuclear potential is described by the Saxon-Woods form and its derivative. The potential is

$$V_{opt.} = -(V_R + iW_v)\frac{1}{1 + \exp[(r-R)/a]}$$

$$- 4iW_{SF}\frac{\exp[(r-\bar{R})/\bar{a}]}{\{1 + \exp[(r-\bar{R})/\bar{a}]\}^2}$$

$$- V_{SO}(\bar{\sigma} \cdot \bar{\ell})\,\lambda_\pi^2 \frac{1}{a}\frac{\exp[(r-R)/a]}{\{1 + \exp[(r-R)/a]\}^2} + V_{coul.}$$

The Becchetti-Greenlees[19] global parameters for protons and the Wilmore-Hodgson[20] parameters for neutrons were used. The Becchetti-Greenlees parameters are

$V_R = 54.0 - 0.32E + 0.4 \frac{Z}{A^{1/3}} + 24.0 \frac{N-Z}{A}$ MeV, the real potential,

where $r_R = 1.17$ fm, the radius, and $a_R = 0.75$ fm, the "diffuseness";

$W_V = 0.22E - 2.7$ MeV or zero, the imaginary volume potential;

$W_{SF} = 11.8 - 0.25E + 12.0 \frac{N-Z}{A}$ MeV, the imaginary surface potential,

where $r_I = 1.32$ fm, and $a_I = 0.51 + 0.7 \frac{N-Z}{A}$ fm;

and $V_{SO} = 6.2$ Mev, the spin-orbit potential,

where $r_{so} = 1.01$ fm, and $a_{so} = 0.75$ fm.

The Wilmore-Hodgson parameters are

$V_R = 47.01 - 0.267E - 0.00118E^2$ MeV,

where $r_R = 1.322 - 7.6A \times 10^{-4} + 4A^2 \times 10^{-6} - 8A^3 \times 10^{-9}$ fm,

and $a_R = 0.66$ fm.

$W_{SF} = 9.52 - 0.053E$ Mev,

where $r_I = 1.266 - 3.7A \times 10^{-4} + 2A^2 \times 10^{-6} - 4A^3 \times 10^{-9}$ fm,

and $a_I = 0.48$ fm.

In order to describe the deformation of the optical potential for a spherically symmetric target nucleus which vibrates about a spherical equilibrium shape, R and $\bar{R}$ are expanded as a sum of spherical harmonics,

$$R = R_0 \left(1 + \sum_{\lambda\mu} \alpha_{\lambda\mu} Y_{\lambda\mu} (\theta,\phi)\right)$$

and $$\bar{R} = \bar{R}_0 \left(1 + \sum_{\lambda\mu} \alpha_{\lambda\mu} Y_{\lambda\mu} (\theta,\phi)\right);$$

where $R_0 = r_0 A^{1/2}$, the real radius, and

$\bar{R}_0 = \bar{r}_0 A^{1/3}$, the imaginary radius.

If these are inserted into the expression for the potential and the latter expanded in powers of $\sum_{\lambda\mu} \alpha_{\lambda\mu} Y_{\lambda\mu}$, one obtains an expression which consists of the usual optical-model potential plus the coupling potential between channels, $V_{coupl.}$ (see Tamura[18]).

The Hamiltonian is

$$H = T + H_o + V_{opt.} + V_{coupl.},$$

where the coupling between channels may be expressed as

$$V_{coupl.} = \sum_{t,\lambda} v_\lambda^{(t)}(r)(Q_\lambda^{(t)} \cdot Y_\lambda) .$$

The first term in this equation, $v_\lambda^{(t)}$, is, in the present case, proportional to the radial derivative of the optical potential.

When the coupled equations are written out in detail, the strength of the coupling between the channels can be expressed in terms of reduced matrix elements, $\langle I \| Q_\lambda^{(t)} \| I' \rangle$, taken between the states of the target nucleus which are described by the sets of quantum numbers represented by I and I'. In the case considered here, the general nuclear operator $Q_\lambda^{(t)}$ is simply related to the deformation operator α_λ introduced above. The superscript t refers to the order in the expansion in terms of α_λ.

It is customary to further express these reduced matrix elements in terms of a set of deformation parameters, β, which must be supplied to the calculation and which contain all of the necessary structural information about the target states. Coupling the ground state to a one-phonon state of angular momentum I, in the vibrational nucleus gives

$$\langle 0;0 \| Q_\lambda^{(1)} \| 1;I \rangle = \delta_{\lambda I}(-)^I \beta_{0\lambda}$$

Coupling the one-quadrupole-phonon state to the two-quadrapole-phonon states gives

$$\langle 1;2||Q_2^{(1)}||2;I\rangle = \beta_{02}\sqrt{2(2I+1)/5} \quad .$$

Coupling the ground state to the two-quadrupole phonon states gives

$$\langle 0;0||Q_\lambda^{(2)}(\lambda_1 = \lambda_2 = 2)||2;I\rangle = \beta_{02}^2\,\delta_{I\lambda}(2200|I0)/\sqrt{2\pi} \quad ,$$

where $\beta_{0\lambda}$ is the deformation parameter for the 2λ - pole state with respect to the ground state, and $(2200|I0)$ is a Clebsch-Gordon coefficient. Finally, coupling the one-quadrupole-phonon state to the one-octupole-phonon state gives

$$\langle 1;2||Q_\lambda^{(2)}(\lambda_1 = 2,\ \lambda_2 = 3)||1;3\rangle = \frac{\beta_{02}\beta_{23}(2300|\lambda 0)}{\sqrt{4\pi}} \quad ,$$

where β_{23} is the deformation parameter of the one-octupole phonon state with respect to the one quadrupole phonon state. Fig. VI-1 shows all of the deformation parameters relevant to this analysis.

The deformation parameters, β, are of central importance in these calculations because the cross sections are proportional to β^2. These parameters can be determined in a number of different ways, including fitting coupled-channel calculations to angular distributions of inelastic scattering data. In the past, they have been most commonly determined by DWBA calculations fitted to experimental angular distributions and by measurements of the electric quadrupole transition probability, B(E2), from Coulomb excitation experiments. In DWBA calculations, the coupling

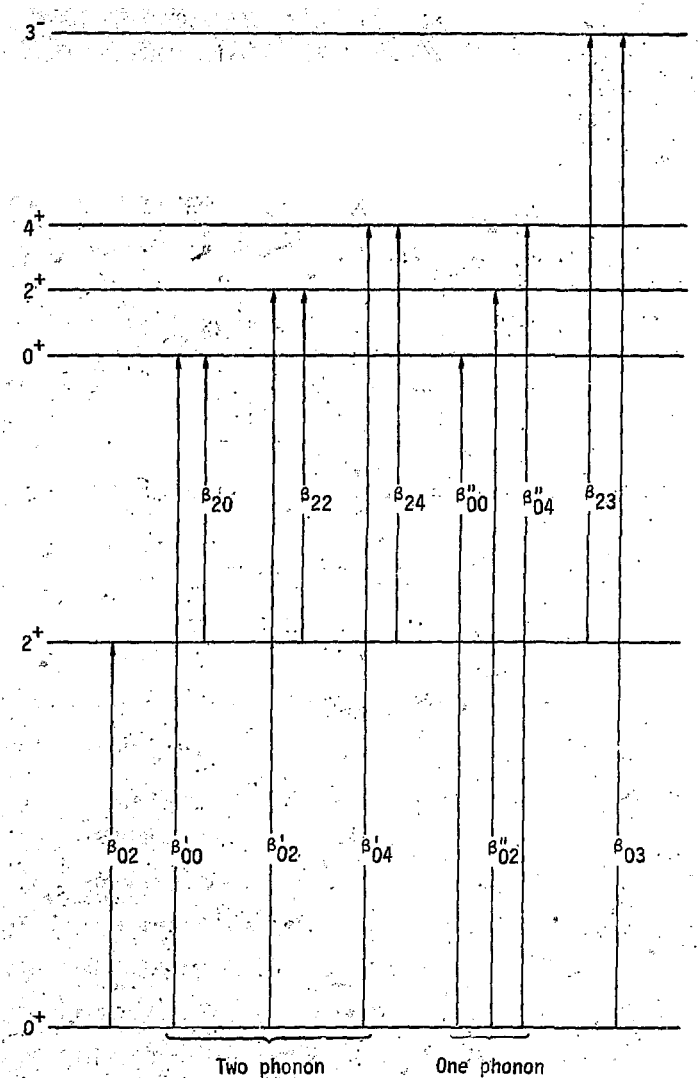

Fig. IV-1. The deformation parameters for the coupled-channel calculations.

between the different channels is treated only to first order in the interaction. To understand the Coulomb excitation measurements, consider the nucleus to be a spheroid with semi-major and semi-minor axes a and b, respectively, and with an average radius R_o, then,[21]

$$\beta_{02} = 1.06(a-b)/R_o .$$

Assuming a uniform charge distribution, and in the limit of small deformations,[21] then

$$\left(\beta_{02}\right)_{em} = \frac{\sqrt{B(E2,0^+\rightarrow 2^+)}}{3ZR_o^2/4\pi} ,$$

where $R_o = 1.2A^{1/3}$ fm .

In general

$$\left(\beta_{0\lambda}\right)_{em} = \frac{\sqrt{B(E\lambda,0^+\rightarrow\lambda)}}{3ZR_o^\lambda/4\pi}$$

where $B(E2)_{exp} = \frac{4.08 \times 10^{-61}}{E_\gamma^5(\text{MeV})\tau(\text{sec})(1+\alpha)}$,

E_γ is the energy of the gamma ray,

τ is the mean life, and α is the internal conversion coefficient.

Values of β_{02} and β_{03}, determined from these relations by Stelson and Grodzins,[21] are listed in Table IV-I as β_{em}. Quadrupole transition probabilities for one-quadrupole transitions from a lower state to an upper state can be written as[77]

$$B(E2) = \frac{1}{2J+1} (n_u I_u \| Q_{20} \| n_L I_L)^2 ,$$

$$\text{where } Q_{20} = \sqrt{\frac{Bo}{5}} (\alpha^+_{20} + \alpha_{20}) .$$

Here Bo is just B(E2) for the $2^+ \rightarrow 0^+$ transition and the α's are raising and lowering operators. The result of evaluating this expression for the one-phonon to two-phonon transitions in a pure vibrational model is:

$$B(E2, 0 \rightarrow 2^+) = Bo$$

$$B(E2, 2^+ \rightarrow 0^+) = \frac{2}{25} Bo$$

$$B(E2, 2^+ \rightarrow 2^+_1) = \frac{2}{5} Bo$$

$$B(E2, 2^+ \rightarrow 4^+) = \frac{18}{25} Bo$$

Also tabulated in Table IV-1 are values of β_{02} and β_{03}, extracted from the literature, which were obtained from fitting angular distributions of (p,p'), (α,α'), (d,d'), and (n,n') data. According to Madsen et al.,[22] a microscopic description, with isospin included properly, shows that β is actually a function of the external field producing the transition. Differences of as much as 20% are expected between β(n,n') and β(p,p') with β(n,n') being closer to β_{em}. If values for β_{em} and β(p,p') are known, it is then possible to estimate a value for β(n,n') from the expression

$$\beta_{n,n'} = \beta_{p,p'} \left[1 + \frac{2}{3} \left(\frac{\beta_{em}}{\beta_{p,p'}} - 1 \right) \right] ,$$

which was derived by Hansen et al.[48] from the expressions in Table II of Madsen et al.[22] Values for $\beta_{n,n'}$ calculated from this expression are listed in Table IV-1 and were used to calculate the direct, collective

Table IV - 1

Deformation Parameters from Various Reactions

Nucleus	β_{em}	$\beta_{p,p'}$	$\beta_{\alpha,\alpha'}$	$\beta_{d,d'}$	$\beta_{n,n'}$ (calc.)	$\beta_{n,n'}$ (exp.)	β'_{0I}	I	β_{2I}	I
^{56}Fe β_{02}	0.22	0.25		0.24	0.23		0.10	0,2,4	0.24	0,2,4
β_{03}	0.17	0.19		0.20	0.18					
^{62}Ni β_{02}	0.193	0.24	0.16	0.22	0.21	0.19	0.11	0,2,4	0.24	0,2,4
β_{03}	0.20	0.21	0.12	0.175	0.20	0.13				
^{64}Zn β_{02}	0.250	0.29	0.25		0.26	0.23	0.06	0,2,4	0.25	0,2,4
β_{03}	0.23	0.24			0.23					
^{108}Pb β_{02}	0.243	0.24			0.24		0.06	0,2,4	0.16 0.22 0.24	0 2 4
β_{03}	0.15	0.14			0.15					
^{110}Cd β_{02}	0.183	0.19	0.20		0.19		0.04	0,2,4	0.13	0,2
β_{03}	0.15	0.17	0.17		0.16				0.16	4
^{114}Cd β_{02}	0.193	0.19	0.21	0.19	0.19		0.12 0.14 0.16	0 2 4	.09 .10 .14	0 2 4
β_{03}	0.14	0.16	0.16		0.15					
^{116}Cd β_{02}	0.201	0.20			0.20		0.04	0,2,4	0.13 0.11 0.18	0 2 4
β_{03}	0.12	0.15			0.13					

Table IV - 1 (continued)

Nucleus	β_{em}	$\beta_{p,p'}$	$\beta_{\alpha,\alpha'}$	$\beta_{d,d'}$	$\beta_{n,n'}$ (calc.)	$\beta_{n,n'}$ (exp.)	β'_{0I}	I	β_{2I}	I
^{116}Sn β_{02}	0.113	0.14	0.115		0.12	0.12				
β_{03}	0.196	0.185	0.130		0.19					
^{120}Sn β_{02}	0.112	0.12	0.11	0.12	0.11	0.12				
β_{03}	0.14	0.14	0.12	0.14	0.14	0.17				
^{206}Pb β_{02}	0.04	0.06	0.052		0.05	0.07	.02	0,2	.04	0,2,4
β_{03}	0.11	0.12			0.11		.04	4		

contribution to the (n,n') gamma cross sections. The values for $\beta_{p,p'}$ listed in the table were used to make similar calculations for the (p,p') experiments. In general, the differences between experimental values of β were greater than any differences due to reaction type. Also tabulated in Table IV-1 are deformation parameters describing the coupling of the one-phonon vibrational state to the two-phonon vibrational states. Experimental values were used when available, otherwise it was assumed that

$$\beta'_{0I} = \beta_{02} \times \beta_{2I} \approx \beta^2_{02} ,$$

where the subscript refers to the level spin, I, a member of the two-phonon triplet, 0, 2, or 4. Curtis et al.[23] have found that $\beta_{2I} \approx \beta_{02}$ to within 15% in the even Ge isotopes.

The absorptive, imaginary part of the global optical potentials used in these calculations were determined without regard to explicitly described inelastic scattering channels. The coupled-channel formalism consists of such an explicit description of these channels; consequently, it is necessary to reduce the global imaginary potential by an amount which just compensates for the effect of these coupled-channels. Curtis et al.[23] found that the imaginary potential should be reduced by about 0.5-MeV for each 10 mb of inelastic cross section explicitly described by the coupled-channels formalism. Following the perscription of Madsen,[67] coupled-channel calculations were performed with the coupling constants (β) reduced by a factor of 10^3. This was the "weak coupling" approximation and was equivalent to a DWBA calculation. The calculation was then repeated with the coupling constants at their nominal values and a ratio formed

between the "weak coupling" inelastic cross section multiplied by 10^6 and this inelastic cross section. The imaginary potential was then reduced by this ratio, which was about 0.79 for the couplings considered here, and all further calculations were performed with this reduced potential.

The standard calculation included the one-phonon coupling of the ground state to the first excited state, β_{02}, the one-phonon coupling of the first excited state to the two-phonon triplet of states, β_{21}, and the two-phonon coupling of the ground state directly to the two-phonon states, β'_{01}. The one-phonon contribution to the two-phonon states, β''_{01}, was ignored. A separate calculation was done including the coupling between the ground state, the one-quadrupole-phonon 2^+ state, and the one-octupole-phonon 3^- state, β_{02}, β_{23} and β_{03}, with the appropriate reduction in the imaginary potential. The contributions from the one-quadrupole-phonon and one-octupole-phonon excitations together accounted for most of the direct excitation cross section calculated. The contribution from the two-phonon states was relatively unimportant.

Experimental measurements, performed by other workers, of (p,p') angular distributions for the strong collective levels in the nuclei of interest were generally available. Whenever possible, the calculations were compared with the experimental data and adjustments in the deformation parameters were made to minimize the difference between the data and the calculation. In general, this allowed us to select the best value of β from among several published values, although many of the β's listed in Table IV-1 are averages of several published values. Figs. IV-2 through IV-4 show comparisons between data and coupled-channel calculations for ^{56}Fe, ^{62}Ni, ^{64}Zn, ^{110}Cd, ^{114}Cd, ^{116}Cd, and ^{206}Pb.

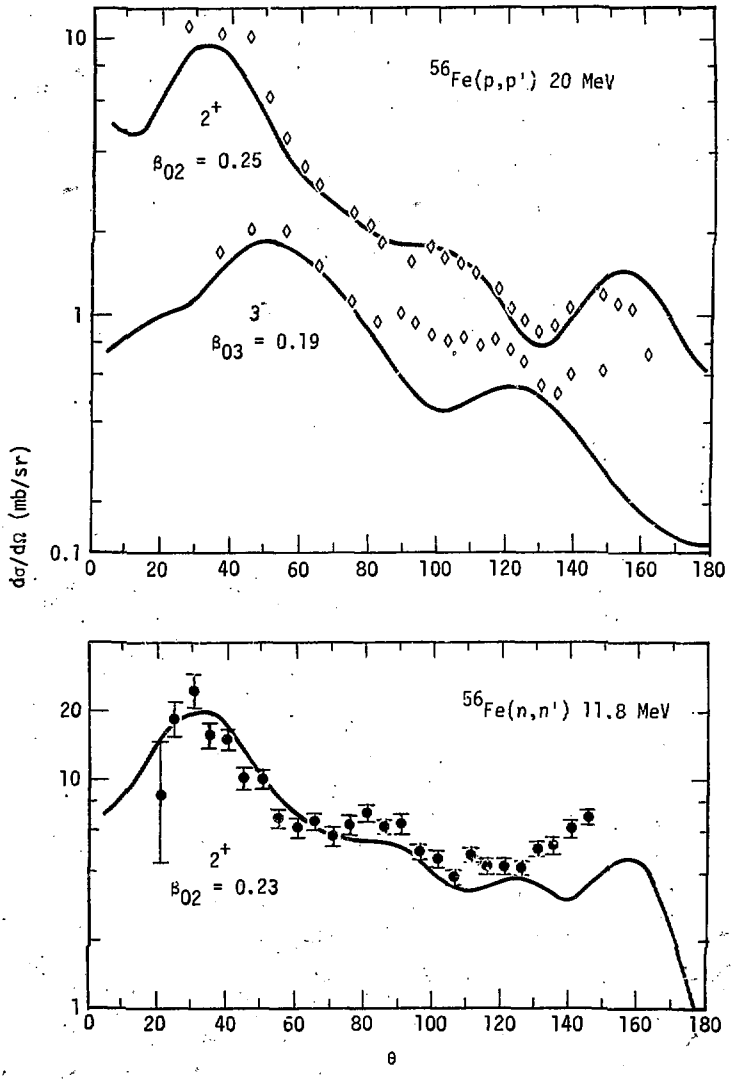

Fig. IV-2. Coupled-channel calculations for ^{56}Fe(p,p') at 20 MeV and ^{56}Fe (n,n') at 12 MeV for 2^+ (0.847 MeV) and 3^- (4.45 MeV) levels; data of Eccles et al.[7] (◊) and Beneveniste[36] (●).

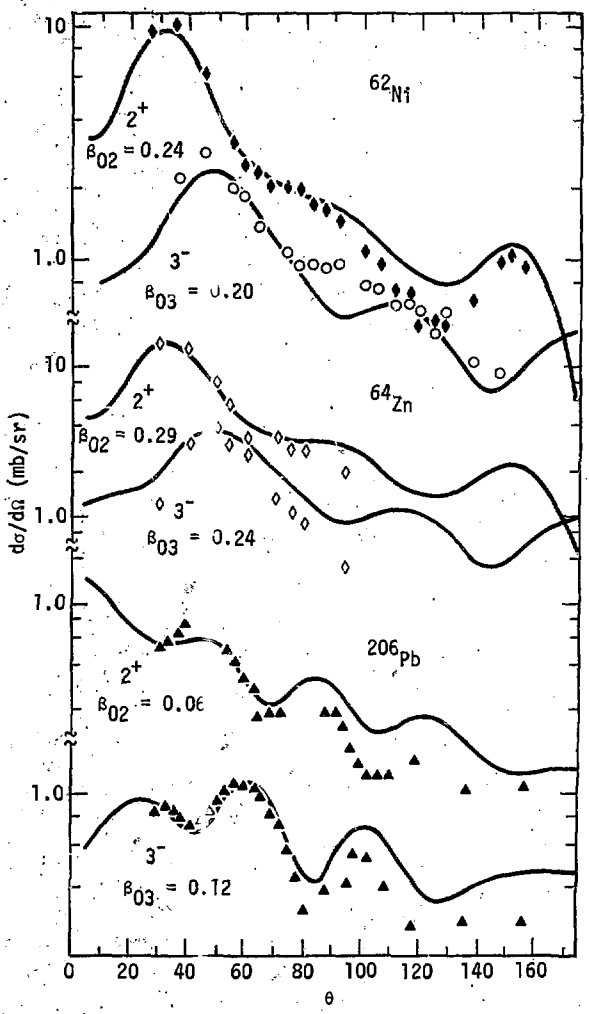

Fig. IV-3. Coupled-channel calculations for 20 MeV protons on ^{62}Ni for 2^+ (1.173 MeV) and 3^- (3.750 MeV) levels, data of Eccles et al.[7] (♦, ○); ^{64}Zn for 2^+ (0.991 MeV) and 3^- (2.99 MeV) levels, data from Tamura[18] (◊); and ^{206}Pb for 2^+ (0.803 MeV) and 3^- (2.648 MeV) levels, data of Glashausser et al.[38] (▲).

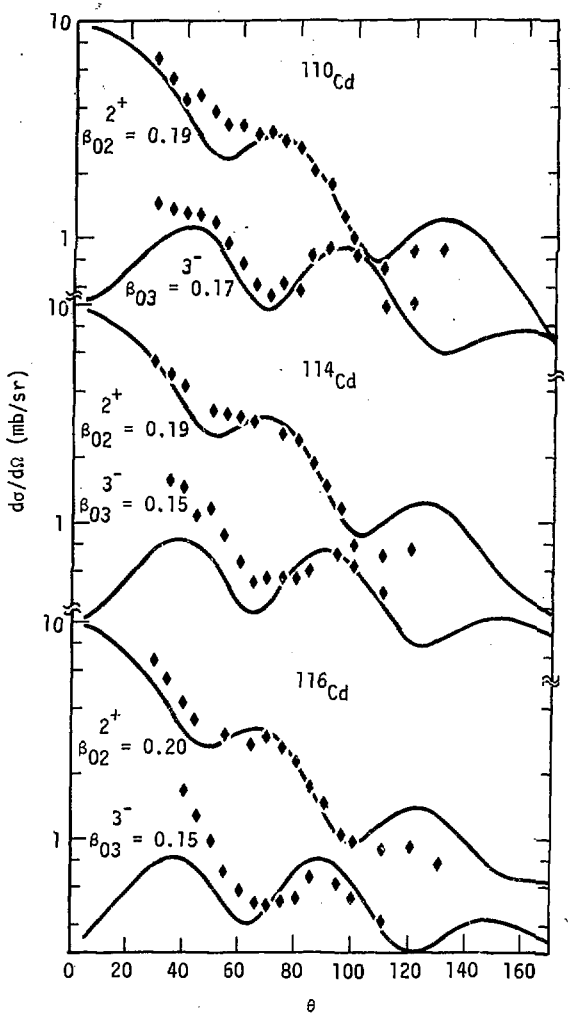

Fig. IV-4. Coupled-channel calculations for 14 MeV protons on ^{110}Cd for 2^+ (0.658 MeV) and 3^- (2.079 MeV) levels; ^{114}Cd for 2^+ (0.558 MeV) and 3^- (1.957 MeV) levels; and ^{116}Cd for 2+ (0.514 MeV) and 3^- (1.920 MeV) levels; data of Lutz et al.[37] (♦).

The results of these calculations, the cross sections for the direct excitation of the collective vibrational levels, are summarized in Tables III-3 and III-4. One can see that direct excitation of the collective levels accounts for a significant percentage of their strength. Up to about 50% of the strength of the $2^+ \rightarrow 0^+$ transition is due to direct excitation, and for transitions from some of the two-phonon levels (0^+ in particular), essentially all of their strength, at some energies, may be due to direct excitation.

B. Statistical and Pre-Equilibrium Model Calculations

It has been known since the 1930's that most particles from nuclear reactions are emitted with low energies and with spectra resembling those of molecules evaporated from a hot body. This observation formed the basis for the statistical model of the nucleus, two versions of which have been used in this work. First, the simple Weisskopf[61,41] evaporation model, which constitutes the compound nuclear, or equilibrium, part of the HYBRID calculation was considered, followed by the Hauser-Feshbach[65] model, used in the STAPRE calculations.

The Weisskopf model produces emitted particle spectra of the form[62]

$$S(E) \sim \sigma(E)E\rho(U\text{-}B\text{-}E),$$

where $\rho(U\text{-}B\text{-}E)$ is the level density of the residual nucleus and U is the excitation energy just before particle emission. The quantities B and E are the binding and kinetic energies of the emitted particle. The cross section, $\sigma(E)$ is that which the excited nucleus would present to the emitted particle for forming a compound nucleus, i.e., the inverse cross section. Values of this quantity for the nucleus in its ground state are generally used in these calculations. At its simplest, the level density, ρ, can be characterized by a single parameter, U, such that

$$\rho(U) \sim \exp(U/T) \quad ,$$

where T is the nuclear temperature and U the excitation energy. This characteristic temperature may be extracted from the slope of particle emission spectra and is commonly used to describe level densities at low excitation.[43] At higher excitation energies, the Fermi gas descrip-

tion of the nuclear level density, given by

$$\rho(U) \sim \frac{\exp 2\sqrt{aU}}{U^{3/2}},$$

becomes more applicable. Here a is the level density parameter, which has been determined to be about A/8 MeV^{-1}, from fitting evaporation spectra from heavy nuclei.[62] In general, the level density parameter is more complicated than A/8, and shows striking nuclear shell effects,[63] even after the pairing energy shift determined by Gilbert and Cameron[43] is applied, or the "back shifted"[74,75] formalism is used.

The inverse cross sections necessary for this model can be determined by optical model calculations. These calculations depend on optical potentials which are largely determined by fitting elastic scattering data over a wide range of nuclei. The compilation by Perey and Perey[64] lists many of these sets of potentials and the conditions for which they are appropriate. Among the more successful "global" potential sets are those of Becchetti and Greenlees[19] for incident protons and of Wilmore and Hodgson[20] for incident neutrons. These potential sets are listed in Section IV-A.

A major shortcoming of the Weisskopf model is that it does not include angular momentum. Angular momentum related effects become increasingly important as the bombarding energy increases and as the mass of the projectile increases. They are important if one is interested in the emission of gamma radiation. Angular momentum values influence the emission probabilities of the various particles relative to gamma radiation at the end of the evaporation cascade. The Hauser-Feshbach model[65] is

basically the evaporation model with conservation of angular momentum and parity added. The compound nuclear scattering cross section for an entrance channel β and an exit channel α can be written schematically as[66]

$$\sigma_{\alpha\beta} = \pi\lambda_\beta^2 \frac{T_\beta T_\alpha}{\sum_\gamma T_\gamma} ,$$

where the T's are transmission coefficients for the entrance and exit channels. The sum over γ is over all possible exit channels. The transmission coefficients are related to the collision matrix elements, $U_{\alpha\beta}$, which are determined from solving the radial part of the Schrodinger equation with the complex optical potential, by the expression[66]

$$T_\beta \equiv 1 - \sum_\alpha \left|\bar{U}_{\alpha\beta}\right|^2 .$$

The transmission coefficients not only vary with energy but depend upon channel characteristics such as the nature of the particle and its orbital angular momentum, ℓ_β, and total angular momentum, $j_\beta = \left|\vec{\ell}_\beta + \vec{s}_\beta\right|$. When this is taken into account, the angular momentum and parity conservation restrictions applied, and provision made for spin-orbit coupling, the result is:

$$\sigma_{\alpha\beta} = \pi\lambda_\beta^2 \sum_{J_i, j_\beta, \ell_\beta} \frac{(2J_i + 1)}{(2J_0 + 1)(2s_\beta + 1)} \frac{T_{\ell_\beta j_\beta}(E_\beta) T_{\ell_\alpha j_\alpha}(E_\alpha)}{\sum_{\ell_\gamma, j_\gamma, E_\gamma} T_{\ell_\gamma j_\gamma}(E_\gamma)} ,$$

where J_0 is the spin of the target nucleus and J_i is the spin of the compound state formed via channel β.

The effect of isospin conservation in the entrance channel may be included by following the procedure detailed by Grimes et al.[49] For incident protons this involves considering the formation of $T_> = T_0 + 1/2$ and $T_< = T_0 - 1/2$ states in the incoming channel β, where $T_0 = (N-Z)/2$ is the isospin of the ground state of the target nucleus. The compound nucleus formation cross section can then be expressed as

$$\sigma_\beta = \frac{1}{2T_0 + 1}\,\sigma_\beta^> + \frac{2T_0}{2T_0 + 1}\,\sigma_\beta^<$$

where $\sigma_\beta^>$ and $\sigma_\beta^<$ are each calculated via the Hauser-Feshbach formalism using transmission coefficients which are assumed to be independent of the isospin channel.

B.1 The HYBRID Model and Calculations

The hybrid pre-equilibrium model of Blann[40] together with the Weisskopf evaporation model[41] constitute the HYBRID code of Blann[40] and Grimes et al.,[42,48] which was used to perform these calculations. As was mentioned above, the Weisskopf formalism does not include angular momentum. The optical model proton parameters of Becchetti and Greenlees[19] and the neutron parameters of Wilmore and Hodgson[20] were used in the optical model code, LOKI,[34] to calculate the inverse cross sections needed by HYBRID. The level densities used in the calculation corresponded to the Fermi gas model of the nucleus, with a pairing energy correction, given by

$$\rho(U) = \frac{\sqrt{\pi}\,\exp\,2[a(U-\delta)^{1/2}]}{12a^{1/4}[U-\delta]^{3/2}}\,.$$

A value for the level density parameter a of $(A/8)$[44,62] was used, and the pairing energy δ was taken from Gilbert and Cameron.[43] At low energies, $0 < U < 4$-MeV, the level density was assumed to have a constant temperature form with the magnitude and slope obtained by matching the magnitude and slope of the Fermi gas level density at 4-MeV. Because the Weisskopf formalism does not include angular momentum, gamma-ray competition cannot be included in a satisfactory manner.

The pre-equilibrium part of the calculation was based on the exciton model (where exciton refers to a particle or hole) of Griffin[45] as modified by Blann.[40] This approach assumes that the compound nucleus reaches equilibrium through a series of two-body interactions. At each stage a small but finite width for particle decay is assumed in addition to the width for decay to more complicated states. This adds a non-equilibrium component to the spectrum. The fraction of states, containing n-excitons, with one particle unbound is a rapidly decreasing function of n. Particle decay occurs either early in the equilibration process, or after equilibrium has been reached, but not in between. Pre-equilibrium emission is nearly independent of target nucleus. It does, however, depend on the type of projectile and its energy.

For the hybrid model, the probability, $P_x(E)dE$, of emission of a particle of type x with energy between E and E+dE is given by[40]

$$P_x(E)dE = \sum_{\substack{n=no \\ \Delta n=2}} \left[{}^nP_x \frac{\rho_n(U,E)}{\rho_n(E^*)} gdE \right] \left[\frac{\lambda_c(E)}{\lambda_c(E) + \lambda_+(E)} \right] D_r$$

In this expression ${}_nP_x$ is the number of particles of type x in an n-exciton state; $\rho_n(E^*)$ is the density of n-exciton states at excitation energy E^*; $\rho_n(U,E)$ is the density of n-exciton states such that a particle, if emitted into the continuum, would have channel energy E and the remaining (n-1) excitons would share an energy U, where $E^* = E + B_x + U$, with B_x being the binding energy of the emitted particle; and g is the density of single particle states per MeV. And $\lambda_c(E)$ and $\lambda_+(E)$ are the rates at which particles of energy $B_x + E$ are emitted into the continuum or scattered with the formation of an additional particle-hole state, respectively. Blann[40] has suggested that this damping width, $\lambda_+(E)$, be determined from the imaginary component of the optical potential. Hence

$$\lambda_+(E) = \frac{2W}{\hbar}$$

The continuum decay width is given by

$$\lambda_c(E) = \frac{\sigma_v v \rho_c(E)}{gV} ,$$

where σ_v is the inverse cross section, v is the velocity of a particle having ρ_c states in the continuum. The parameter V is an arbitrary volume and cancels the same volume in ρ_c. D_n is a depletion factor, which gives the relative flux reaching an n-exciton state before decay occurs.

The cross section is obtained by summing $P_x(E)$ over angular momentum ℓ with the result

$$\frac{d\sigma_x(E)}{dE} = \pi\lambda^2 \sum_{\ell=0} (2\ell+1)T_\ell P_x(E)$$

where T_ℓ is the transmission coefficient for angular momentum ℓ in the entrance channel. The emission probability, $P_x(E)$, is implicitly dependent on angular momentum through $\lambda_+(E)$, which is determined by the optical model potential, W, and λ_c, which is angular momentum dependent through the inverse cross sections which are determined by LOKI[34] optical model calculations. Grimes[42,49] has modified the code to include a pairing correction and isospin. The inclusion of isospin is particularly important for the (p,p') reactions.

Calculations done with this model have been compared with (p,p'), (p,n), and (n,n') spectra in a number of papers,[40,42,47,48] and the agreement has been reasonably good considering the simplified nature of the model. In the present work, calculations were performed to try to reproduce a selected set of (p,p') and (n,n') spectra as well as the gamma cross sections. For the protons, the data consist of full (p,p') spectra for most of the nuclei investigated but at only a few energies, generally around 14-MeV. For the neutrons, complete spectra at 14-MeV for Fe, Ni, and Pb were available. After evidence was obtained that the calculations could reasonably reproduce the (p,p') data at a few energies, they were then performed over the energy range 9 to 26-MeV and compared with the $(2^+ \rightarrow 0^+)$ gamma cross sections.

Inelastic proton scattering is strongly influenced by isospin considerations. Fig. IV-5 is a schematic representation of the reaction processes involved for 14-MeV protons incident on ^{62}Ni, with the isospin possibilities shown. The isospin of the ground state

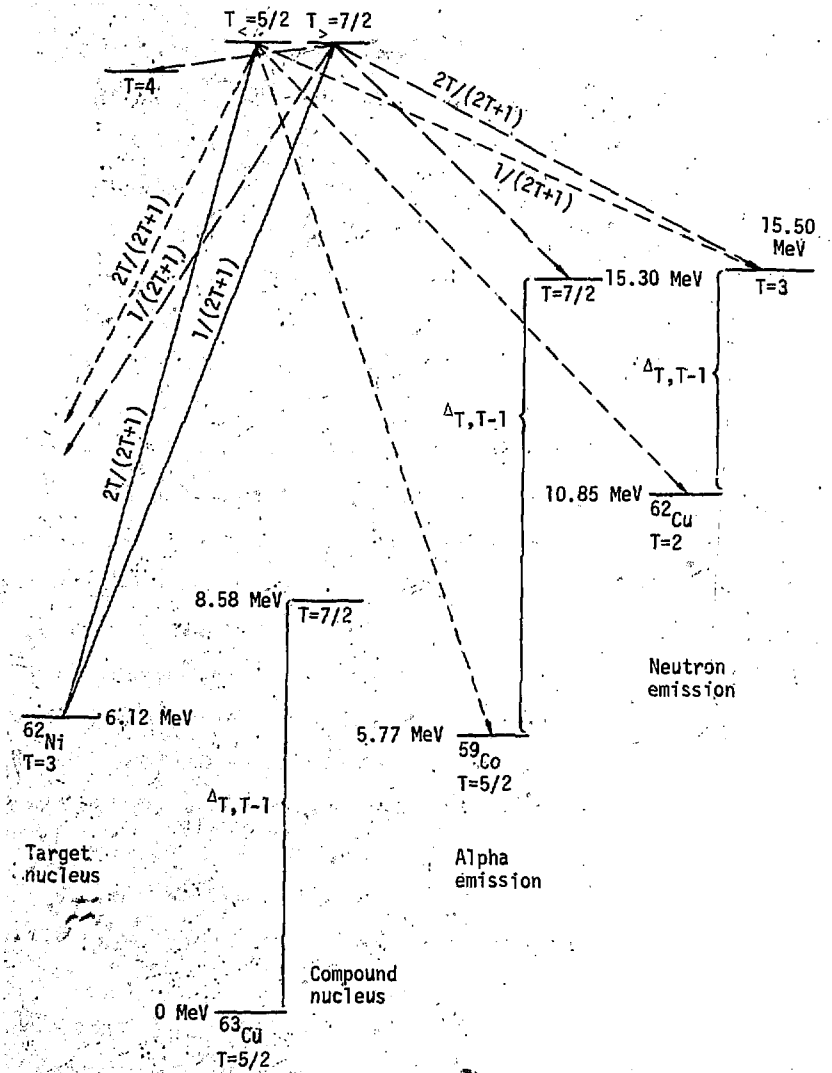

Fig. IV-5. A schematic representation of isospin details for 14 MeV protons incident on ^{62}Ni.

of the target nucleus, T_0, is equal to 3 for ^{62}Ni. The incident proton carries isospin 1/2 with z component -1/2, and can couple to the target nucleus isospin to form either a $T_< = T_0 - 1/2 = 5/2$ or a $T_> = T_0 + 1/2 = 7/2$ state with probability $2T_0/(2T_0 + 1) = 6/7$ or $1/(2T_0 + 1) = 1/7$, respectively, in the compound system. The reaction cross section can be expressed as

$$\sigma_R = \frac{1}{2T_0 + 1}\sigma_R^> + \frac{2T_0}{2T_0 + 1}\sigma_R^<$$

in terms of the reaction cross sections for the $T_<$ and $T_>$ states. The energy of the $T_<$ state, in the compound system, is equal to the kinetic energy of the proton plus the proton binding energy. The ground state of the $T_>$ compound nucleus is shifted with respect to the $T_<$ by the symmetry energy, $\Delta_{T,T-1}$, which for ^{63}Cu is 8.85-MeV. This means that the effective excitation in the $T_>$ channel is 8.58-MeV less than it is in the $T_<$ channel.

Isospin selection rules help determine how the compound system will decay. For nucleon emission the change in isospin, ΔT, must be $\pm$ 1/2, while for alpha emission $\Delta T = 0$. The $T_<$ states can decay by proton emission back to the target nucleus with a weight factor of $2T_0/(2T_0 + 1)$, by neutron emission to the $T_>$ states in the (p,n) nucleus with weight factor $1/(2T_0 + 1)$, or by neutron emission to the $T_<$ states in the (p,n) nucleus with weight factor 1. These decays are shown by dotted lines in Fig. IV-5. The $T_>$ states can decay by proton emission back to the target nucleus with a weight factor $1/(2T_0 + 1)$, or to the $T_>$ states in the (p,n) nucleus with a weight factor $2T_0/(2T_0 + 1)$ but <u>not</u> to the $T_<$ states in the (p,n)

nucleus. These decays are shown by dashed lines in Fig. IV-5. The fact that (p,n) decay from the $T_>$ compound states to the $T_<$ states is isospin forbidden effectively forces these states to decay by proton emission. For many of the nuclei examined, the decay of the $T_>$ compound states was the dominant source of scattered protons. The $T_<$ states can α-decay only to $T_<$ states in the (p,α) nucleus, and the $T_>$ states can decay only to $T_>$ states. The HYBRID calculations do not presently include alpha decay, so these channels were ignored.

Comparison with (p,p') Data

The scattered proton data of Sprinzak et al.,[5] integrated over angle, for 14-MeV incident protons on ^{56}Fe, ^{62}Ni, and ^{64}Zn is shown in Fig. IV-6. Superimposed on these data are the HYBRID calculations. These calculations were done with the Fermi gas level density parameter, a, equal to A/8. The imaginary potential of Beechetti-Greenlees[19] was built into the code and used to calculate the pre-equilibrium damping width. The calculations were done initially with pairing energies from Gilbert and Cameron,[43] which were then changed slightly in later calculations in order to get better agreement between calculation and measurements. It is thought that this was necessary partly because the alpha decay channel was neglected in the calculations and alpha competition is significant in these nuclei. In addition there are uncertainties in the values of the pairing energies and uncertainties as to the extent to which "shell shifts" should be included in the energy shifts of the level densities around closed shells. The pairing energies of Nemirovsky and Adamchuk[50] are slightly larger, in general, than those of Gilbert and Cameron and

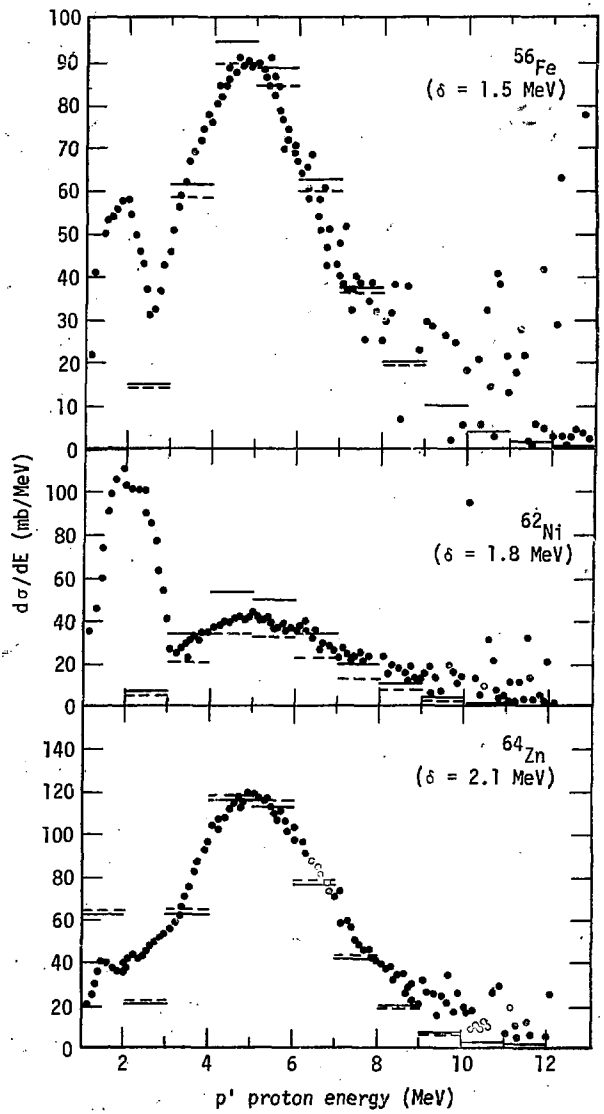

Fig. IV-6. The (p,p') data of Sprinzak[5] at 14 MeV and the HYBRID calculations for isospin conserved (——) and no isospin (---).

consequently give better agreement between measurement and calculation for the lighter nuclei. For ^{64}Zn at 14-MeV, it is estimated that the inclusion of an alpha channel would reduce the strength in the (p,p') channel by about 10-20%, which is not enough for agreement between calculation and measurement without adjusting the pairing energy.

The calculation for isospin conserved is given by the solid line and for no isospin by the dashed line in Fig. IV-6. The importance of isospin in describing the (p,p') reaction is not so apparent for the lighter nuclei, Fe, Ni, and Zn, but will be for the heavier nuclei.

The ^{110}Cd (p,p') proton data, at 16-MeV, of Lux, Porile, and Grimes[16] are shown in Fig. IV-7, along with the HYBRID calculations for isospin conserved, no isospin (isospin mixed) and pre-equilibrium events alone. As was first demonstrated by Fluss et al.,[51] isospin conservation leads to a relative enhancement in the (p,p') cross section, since this is the only reaction that can proceed via the $T_>$ state in the compound nucleus. This may be seen in Fig. IV-7 where the HYBRID calculation without isospin produces too few (p,p') events. If the calculation is done with isospin completely conserved, too many (p,p') events are predicted. The decay of the isospin conserved $T_>$ states competes with the mixing of these states into the $T_<$ states of the compound nucleus by the Coulomb interaction. Lux et al.[16] have determined the isospin mixing fraction, for ^{110}Cd(p,p') at 16-MeV, to be 0.68 $\pm$ 0.15, using a formalism developed by Grimes et al.[49] Mixing the two HYBRID calculations by this amount produces good agreement with the data, as can be seen in Fig. IV-7. It should

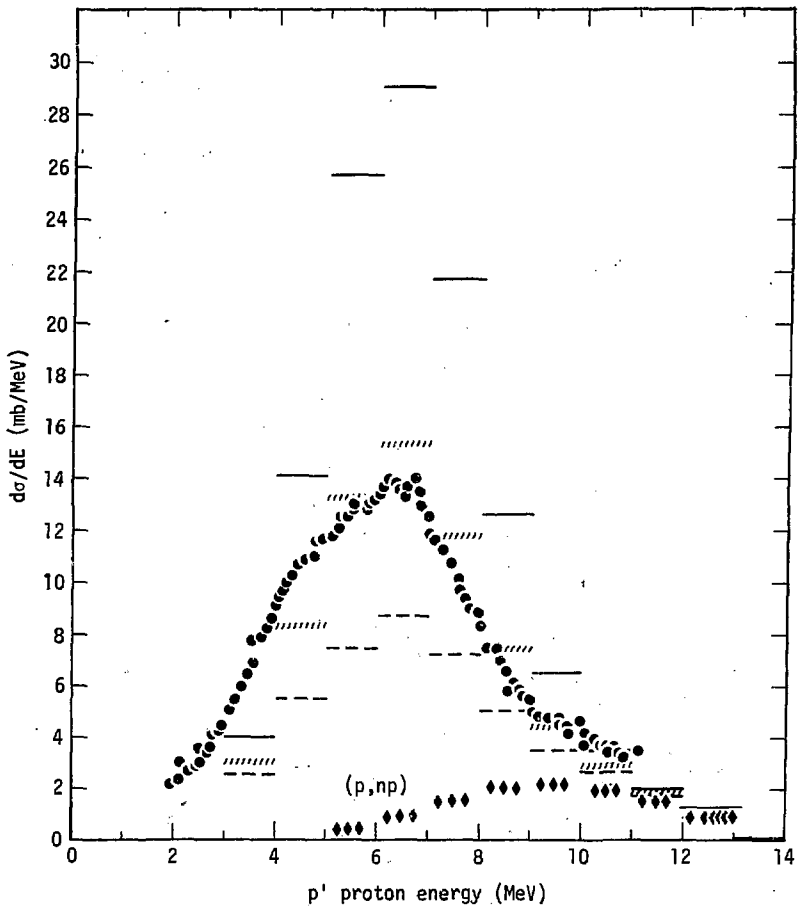

Fig. IV-7. The $^{110}Cd(p,p')$ data of Lux[16] at 16 MeV and HYBRID calculations for isospin conserved (——), no isospin (---), 68% isospin mixing (////////), and pre-equilibrium alone (♦♦♦); δ = 1.3 MeV.

be pointed out that the isospin mixing fraction was not determined simply by fitting the (p,p') spectrum, since there are too many relatively uncertain parameters, such as the pairing energy, δ, and the level density parameter, a, involved in the calculation. Rather, a series of experiments, involving formation of the same compound nucleus, ^{111}In, with protons and alpha particles, was performed. These data were used to determine δ and a, which were then used to calculate the ^{110}Cd(p,p') spectra. The actual mixing fraction was determined from the quantity

$$R_{exp} = \frac{\sigma(p,p')}{\sigma(p,\alpha)} \frac{\sigma(\alpha,\alpha')}{\sigma(\alpha,p)}$$

which, in the absence of isospin conservation, would be equal to unity. It was necessary to apply an angular momentum correction since the angular momentum distributions in the proton and alpha entrance channels were different. The maximum possible value of R, corresponding to conserved isospin, was determined from statistical model calculations. Comparison of R_{exp} and R_{max} yields μ, the mixing fraction.

Isospin mixing fractions have been determined only in a few isolated instances.[52,53] Values from Lux, Porile, and Grimes[16] for the nuclei of interest are plotted in Fig. IV-8, and are seen to scatter between 0.3 and 0.7 for a compound nuclear excitation ranging from 17 to 24-MeV. If one looks at the values for ^{64}Zn and ^{69}Ga, which were determined at several energies, it appears that in this energy range, at least, μ is decreasing with energy. It has been predicted that isospin mixing should be minimal at both low and high

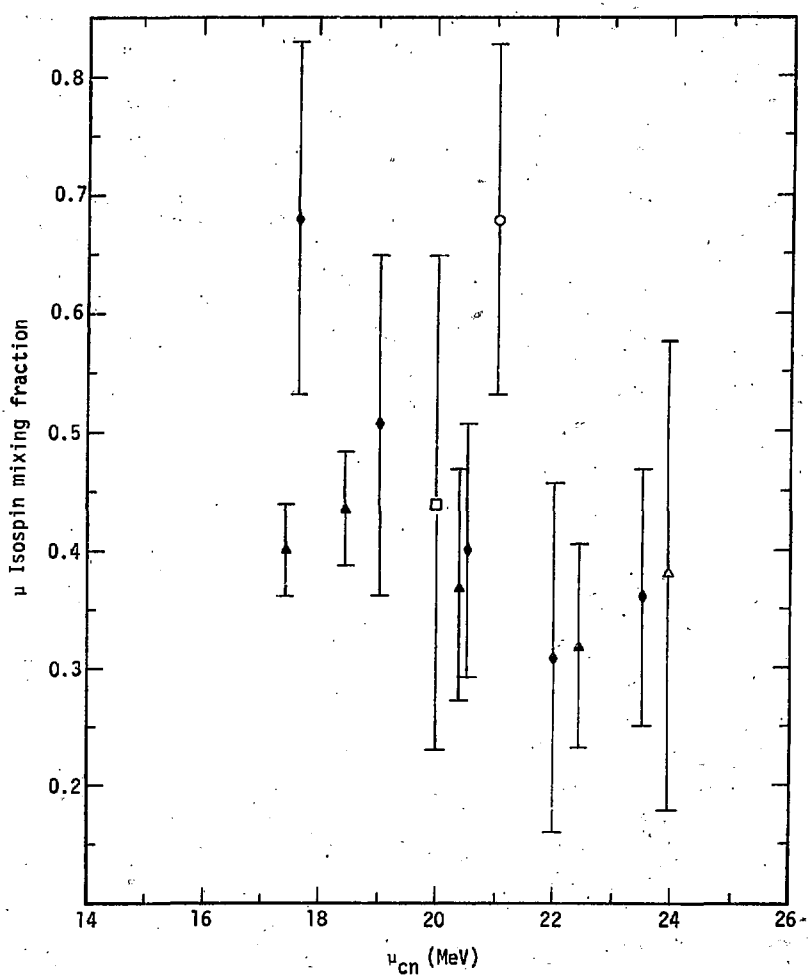

Fig. IV-8. Isospin mixing fraction vs. compound nuclear excitation energy for ^{111}In (Φ), ^{69}Ga (Φ), ^{64}Zn (Φ), ^{63}Cu (Φ), ^{56}Fe (Φ)

excitation energies of the compound nucleus, but substantial at intermediate energies.[52,54,55] One therefore expects to see changes with energy in the intermediate energy region.

The ^{120}Sn(p,p') proton data, at 17.8-MeV and 90°, of Kalbach-Cline, Huizenga, and Vonach[8] are shown in Fig. IV-9 along with the HYBRID calculation for isospin conserved, no isospin, and 68% isospin mixing. The calculation adequately reproduces the low energy evaporation peak at about 7-MeV, but fails to reproduce the sizable strength above 9-MeV. Angular distributions[8] of the events in this region show them to be forward peaked as would be expected in pre-equilibrium events. Kalbach[8] does in fact reproduce the spectral shape by including much more of a pre-equilibrium contribution than that obtained from HYBRID.

Comparison With (n,n') Data

Inelastic neutron scattering reactions have also been calculated and compared with data. Isospin effects do not play a role in these reactions. The 14-MeV Fe(n,n') data of Kammerdiemer[24] and several others,[57,58] plus the HYBRID calculation, with direct contributions to the low energy discrete states added, are shown in Fig. IV-10. The agreement between measurement and calculation is quite good although it appears that the coupled-channel calculations yield slightly too much direct collective strength for the first 2^+ level and not quite enough for some of the higher-lying levels. Similar calculations were performed for 14-MeV neutrons on ^{62}Ni and ^{206}Pb. The results are compared with the inelastic neutron data of Kammerdiemer[24] and others[57,58] in Fig. IV-11 and IV-12, respectively. Again, the direct

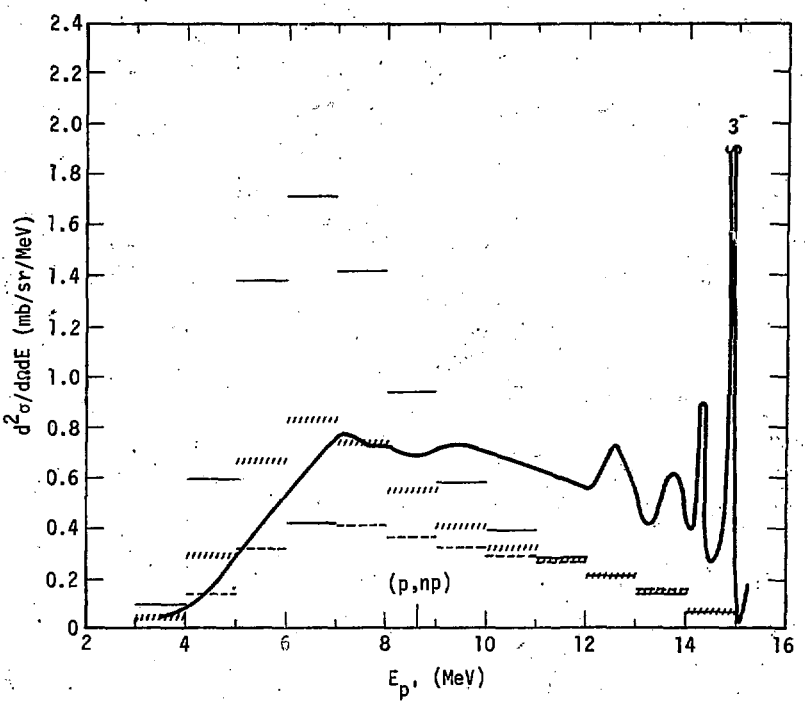

Fig. IV-9. The ^{120}Sn(p,p') data of Kalbach at 17.8 MeV and 90° plus the HYBRID calculations for isospin conserved (——), no isospin (---), and 68% isospin mixing (////////) with δ = 1.2 MeV.

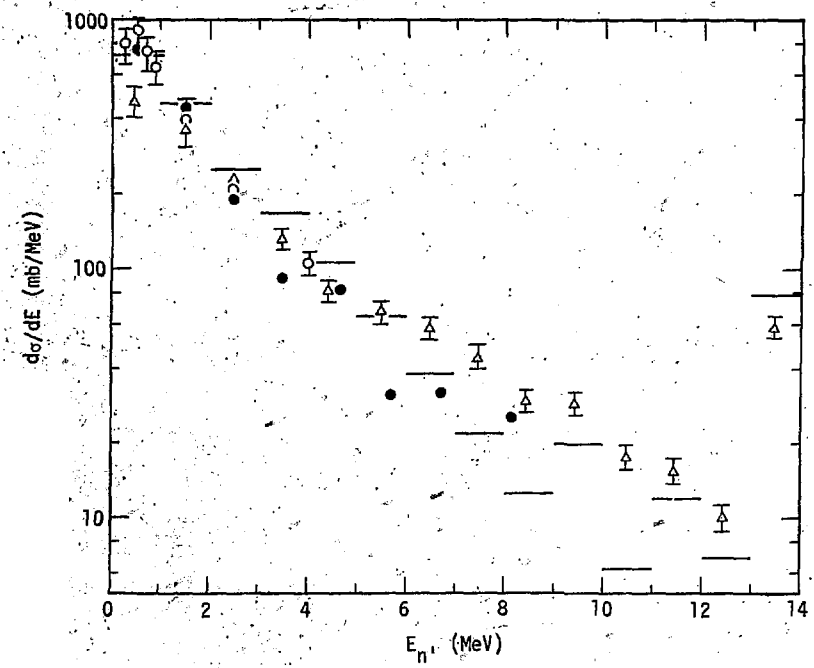

Fig. IV-10. The Fe(n,n') data of Kammerdiener[24] (Δ), Mathur[58](●), and Clayeaux & Voignier[57] (◇) and HYBRID calculations with direct (from coupled-channel calculations) added, for 14 MeV neutrons.

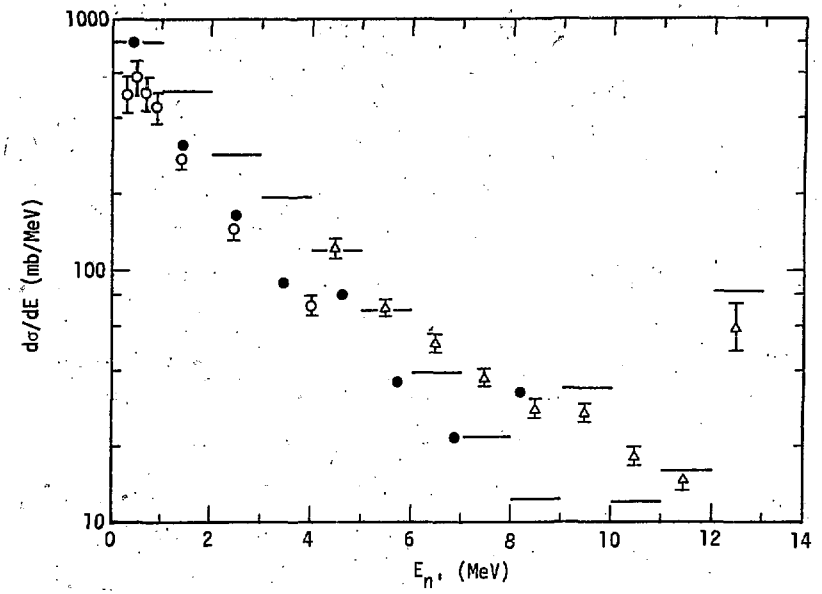

Fig. IV-11. The Ni(n,n') data of Kammerdiener[24] (⊼), Mathur[58] (●), and Clayeaux & Voignier[57] (○) and HYBRID calculations with direct (from coupled-channel calculations) added, for 14 MeV neutrons.

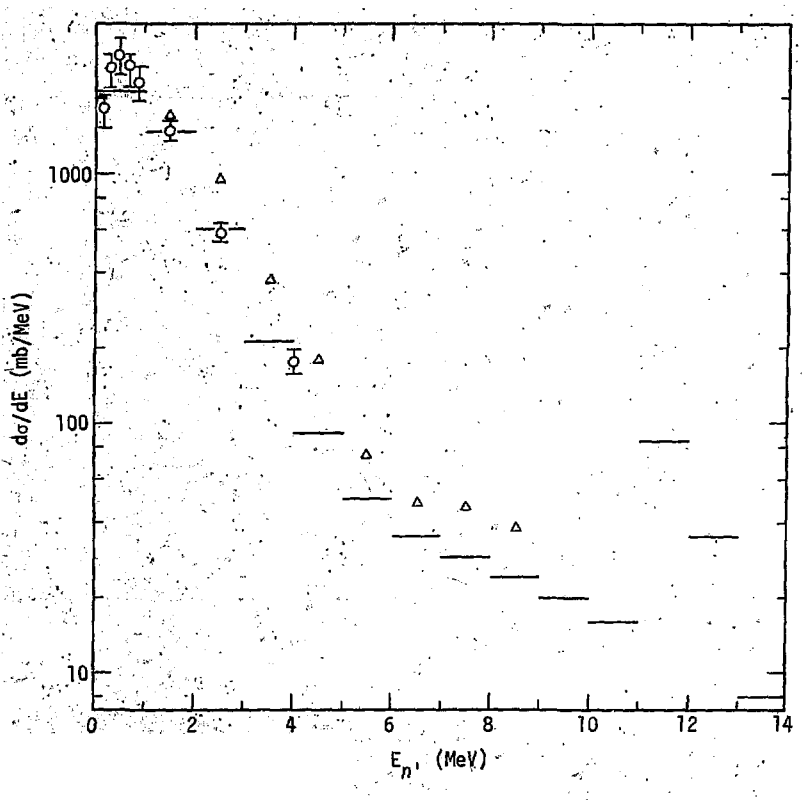

Fig. IV-12. The Pb(n,n') data of Kammerdiener[24] (△), Clayeaux & Voigneir[57] (○), and HYBRID calculations with direct (from coupled-channel calculations) added, for 14 MeV neutrons.

contribution, as calculated by the coupled-channel code for the discrete low-lying collective levels, has been added to the HYBRID calculation. The agreement between calculation and data is quite good for Ni and fair for Pb. The Pb data are systematically higher than the calculation at high energies. Since the calculations were done for the isotopes ^{62}Ni and ^{206}Pb and the spectra were obtained from natural targets, it is possible that the discrepancies between data and calculation are due to our failure to make the calculations for all the isotopes present and to take into account their different particle separation energies. More likely, however, is the possibility that multiple scattering events have contributed to the experimental spectrum.

Comparison with (p,p'γ) Data

The HYBRID calculations relevant to the gamma measurements in the present work are best summarized by presenting them, as a function of incident particle energy, in comparison with the $2^+ \rightarrow 0^+$ gamma cross sections. Fig. IV-13 shows the calculations and data for ^{56}Fe(p,p'γ). The upper curve is the calculation for isospin conserved and the lower curve for no isospin (isospin mixed). The calculated curves converge as incident proton energy increases. After the (p,pn) threshold is passed, at 11.4-MeV, protons from this reaction become increasingly important in the calculated spectrum until it becomes necessary, above 14-MeV, to cut the spectrum off at the neutron separation energy (B_n) plus 1-MeV (one bin above the separation energy), to estimate that part due to (p,p') events alone. This is indicated by the dashed

line in Fig. IV-13, and is equivalent to assuming that the gamma-ray widths are such that neutron decay does not occur if only 1-MeV or less is available. Also, as energy increases, the pre-equilibrium contribution to the total proton spectrum, shown in the lower right in Fig. IV-13, becomes increasingly important. Isospin effects do not strongly influence the reaction cross section for this nucleus, since proton decay from $T_<$ states is significant.

The HYBRID calculations and $(p,p'\gamma)$ data for ^{62}Ni are shown in Fig. IV-14. For this nucleus, the calculations with isospin conserved (upper curve) yield substantially larger values for the integrated cross section than do the calculations for isospin mixed (lower curve), probably due to a relatively small (p,n) Q value. The gamma data and the integrated proton data lie between the extremes of complete isospin conservation and mixing, indicating that there is a net damping of $T_>$ states into $T_<$ states during the reaction process. The average mixing for the three integrated (p,p') cross sections shown is 32%, and a curve representing 32% mixing is shown by the dotted line. It is not expected that the amount of mixing remains constant with incident energy, but neither the data nor the calculations are precise enough to determine changes in the amount of mixing with energy. Above 14-MeV, the spectra are cut off at the neutron separation energy, B_n, plus 1-MeV, with the result shown by the dashed curve in Fig. IV-14. As with the ^{56}Fe calculations, it is clear that at high energies, simply cutting the spectrum at B_n + 1 MeV is an oversimplification and results in cross sections which are too low. There is possibly a tail of (p,p')

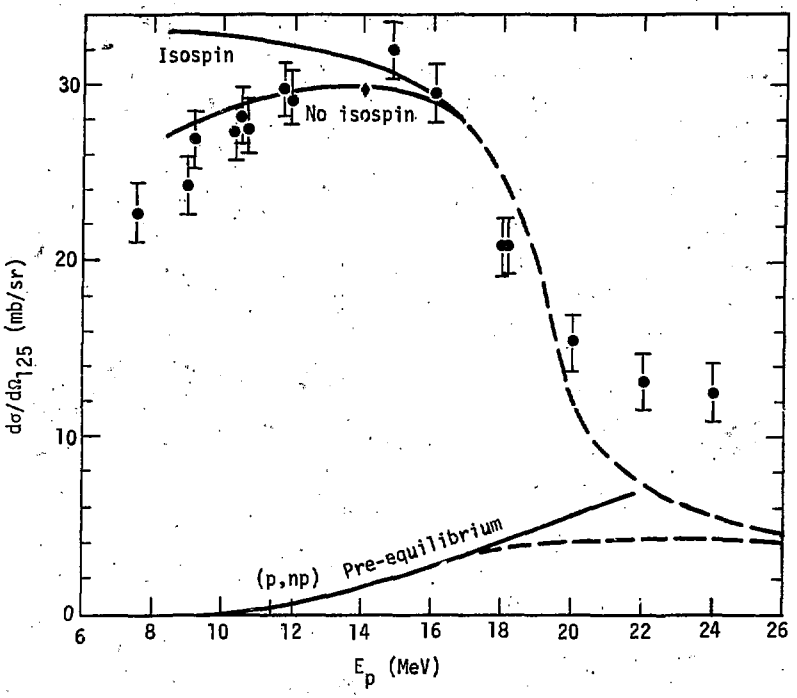

Fig. IV-13. The $^{56}Fe(p,p'\gamma)$ 0.847 MeV ($2^+ \rightarrow 0^+$) gamma cross section minus direct (♦) and HYBRID calculations (——), cutoff at Bn+1 (---), and integrated proton data (♦); δ = 1.5 MeV.

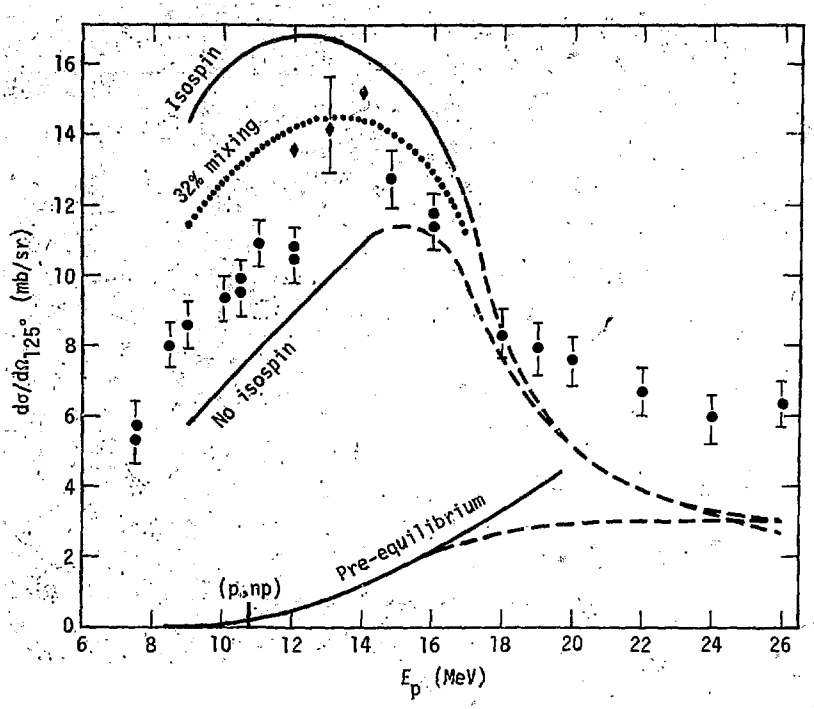

Fig. IV-14. The ^{62}Ni(p,p'γ) 1.173 MeV ($2^+ \rightarrow 0^+$) gamma cross section minus direct (Φ) and HYBRID calculations (——), cut off at Bn+1 (---), and integrated proton data (♦); δ = 1.8 MeV.

events extending substantially above the (p,np) threshold which is being cut off by this procedure. This would be expected if the ratio of particle width to gamma width decreases with increasing angular momentum, since at higher bombarding energies the (p,p') reaction would tend to populate higher angular momentum states.

The $(2^+ \rightarrow 0^+)$ gamma cross sections, integrated (p,p') data, and HYBRID calculations for $^{64}Zn(p,p')$ are shown in Fig. IV-15. The first calculation is shown at 12.5-MeV, since the low energy calculations show anomalies due to the omission of the alpha decay channel in the calculation. This nucleus has unusually high (p,n) and (p,p'n) thresholds, and neglecting alpha decay forces too much strength into the (p,p') channel at low energies. Isospin effects are practically non-existent, consistent with the high (p,n) Q value. If the alpha decay channel is important, however, it would decrease the proton flux from the $T_<$ channel much more than from the $T_>$ channel, thus increasing the effect of isospin conservation. The calculation very closely tracks the data with increasing proton energy. Pre-equilibrium events are important only at the highest energies. As in the other calculations, it became necessary, above 14-MeV, to cut the emitted proton spectrum off at B_n + 1-MeV to eliminate protons from (p,p'n) events.

Fig. IV-16 shows the $(2^+ \rightarrow 0^+)$ gamma cross sections for ^{110}Cd with the integrated (p,p') data and the HYBRID calculations as a function of incident proton energy. The upper curve is the calculation with isospin conserved in the reaction, while the lower curve is for isospin completely mixed (no isospin). Lux et al.[16]

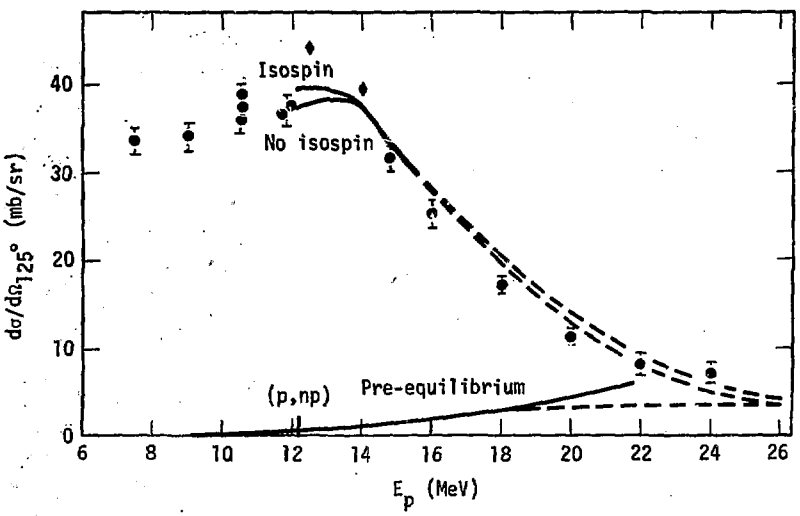

Fig. IV-15. The $^{64}Zn(p,p'\gamma)$ 0.991 MeV ($2^+ \rightarrow 0^+$) gamma cross section minus direct (⧫) and HYBRID calculations (——), cut off at Bn+1 (---), and integrated proton data (♦); δ = 2.1 MeV.

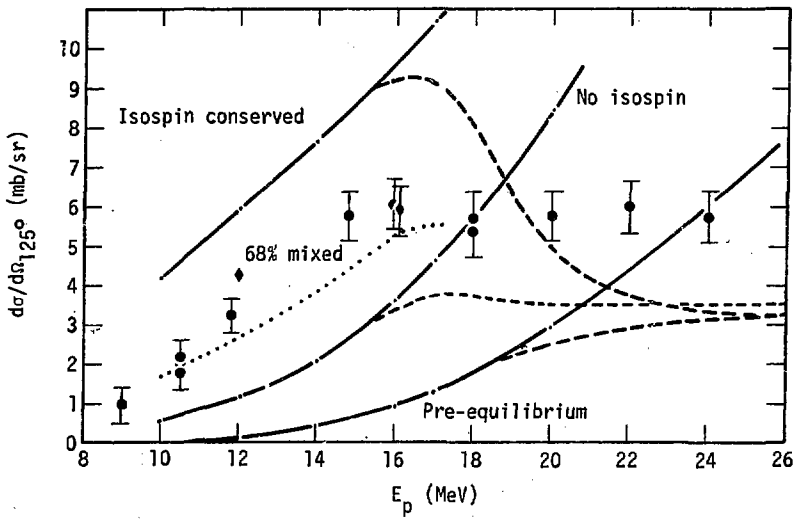

Fig. IV-16. The $^{110}Cd(p,p'\gamma)$ 0.658 $(2^+ \rightarrow 0^+)$ gamma cross section minus direct (♦) and HYBRID calculations (—·—), cut off at Bn+2 (———), and integrated proton data (♦); δ = 1.3 MeV.

have determined the isospin mixing to be 68% at 16-MeV, and the dotted curve represents 68% mixing for the HYBRID calculations. It is in reasonably good agreement with the gamma data. The pre-equilibrium contribution to the calculation is shown by the lowest curve. It rises from essentially zero around 12-MeV to account for most of the calculated cross section above 24-MeV. For incident proton energies of 16-MeV and above, it was necessary to cut off the emitted proton spectrum at the neutron binding energy plus 2-MeV, for the heavier nuclei. This assumes that above B_n + 2-MeV, all protons come from the (p,np) reaction, which is obviously an oversimplification for ^{110}Cd. The calculated curves converge to a cross section, at 24-MeV, which is about half of the measured value.

The measured ($2^+ \rightarrow 0^+$) gamma cross sections for ^{114}Cd(p,p'γ) reactions (with direct subtracted), the integrated (p,p') proton cross sections, and the HYBRID calculations, as a function of incident proton energy, are shown in Fig. IV-17. The upper curve is the calculation for isospin conserved and the lower curve is for isospin mixed (no isospin) reactions. The calculated proton emission spectra are cut off at B_n + 2-MeV for proton energies of 16-MeV and above and are shown by the dashed curve. The dotted line represents about 40% isospin mixing and appears to agree quite well with the data. The pre-equilibrium contribution is shown by the lowest curve. Essentially all of the no isospin (isospin completely mixed) cross section is due to pre-equilibrium processes. As with ^{110}Cd, the cut-off calculations converge to a cross section at 26-MeV which is too low, indicating that some of the low energy protons (below B_n + 2 MeV) are probably due to (p,p') events.

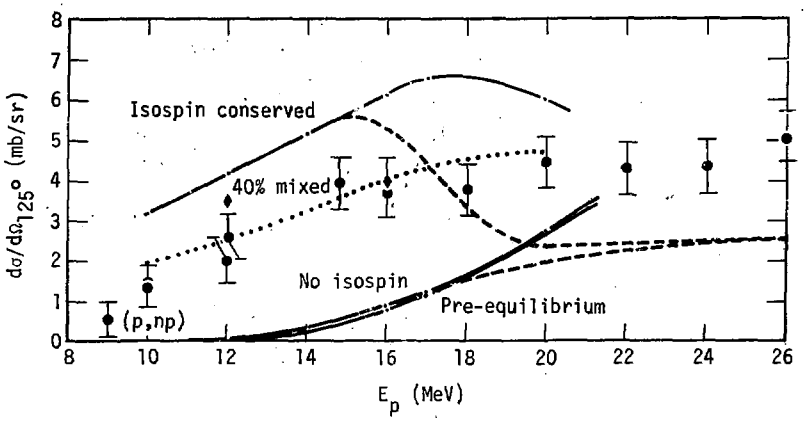

Fig. IV-17. The $^{114}Cd(p,p'\gamma)$ 0.558 MeV ($2^+ \rightarrow {}^+$) gamma cross section minus direct ( ), HYBRID calculations (-•-), cut off at Bn+2 (---), and integrated proton data ( ); δ = 1.3 MeV.

Fig. IV-18 shows the HYBRID calculations superimposed on the $2^+ \rightarrow 0^+$ gamma cross sections for $^{116}Cd(p,p'\gamma)$. The results are very similar to those observed for ^{114}Cd in Fig. IV-17 except that, in this case, the calculation with isospin conserved is somewhat closer to the data. Looking back at ^{110}Cd in Fig. IV-16, one can see what appears to be a systematic decrease in isospin mixing with increasing isotopic mass. This may simply reflect the systematic decrease in (p,n) Q values with increasing isotopic mass or the increase in symmetry energy. Alternatively, it might simply be a consequence of the global parameters (particularly the level density parameter) not being sensitive enough to changes in isotopic mass.

Gamma data and HYBRID calculations for $^{116}Sn(p,p'\gamma)$ are shown in Figs. IV-19 and IV-20, respectively. The calculated ^{116}Sn (p,p') spectra were cut off at B_n + 1 MeV rather than B_n + 2 MeV as was done for ^{120}Sn and the other heavy nuclei. The calculations bracket the data at low energies, where mixing is important, and show good agreement with the data at high energies, where the procedure of cutting off the spectra at one or two MeV above the separation energy has failed for the other reactions considered. For ^{116}Sn, the data lie very close to the no-isospin calculation, substantially closer than do the ^{120}Sn data, showing the same behavior with isotopic mass as did the Cd isotopes.

The $(2^+ \rightarrow 0^+)$ gamma cross sections and HYBRID calculations for $^{206}Pb(p,p'\gamma)$ reactions, as functions of proton energy, are shown in Fig. IV-21. The data generally lie between the isospin conserved and the isospin mixed calculation. No attempt was

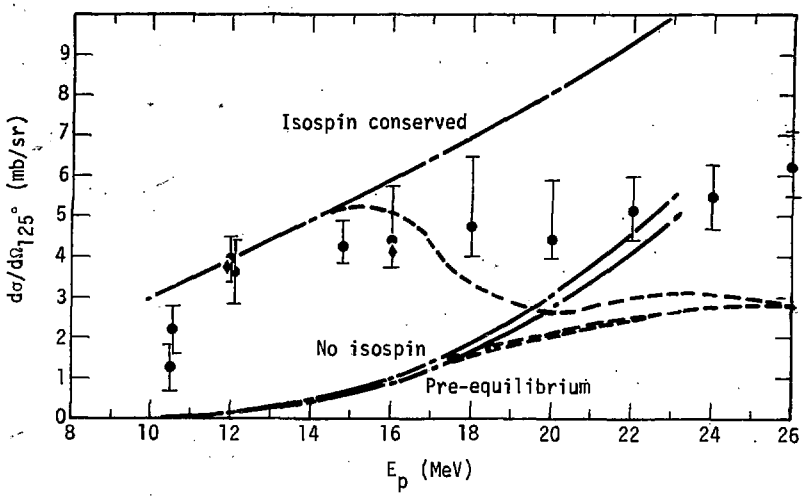

Fig. IV-18. The $^{116}Cd(p,p'\gamma)$ 0.514 MeV ($2^+ \rightarrow 0^+$) gamma cross section minus direct (♦), HYBRID calculations (—·—), cut off at Bn+2 (— — —), and integrated proton data (♦); δ = 1.3 MeV.

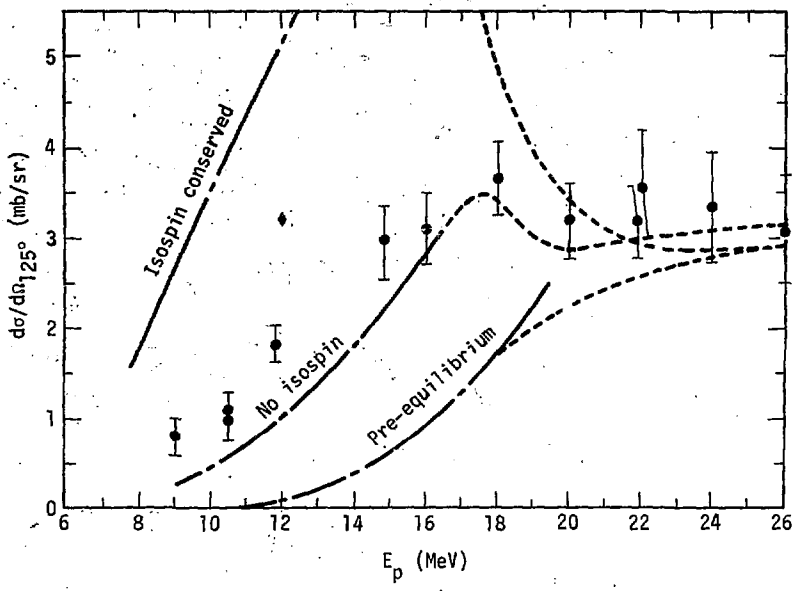

Fig. IV-19. The $^{116}Sn(p,p'\gamma)$ 1.293 MeV $(2^+ \rightarrow 0^+)$ gamma cross section minus direct (♦), HYBRID calculations (—·—), cut off at Bn+1 (— — —), and integrated proton data (♦); $\delta \approx 1.3$ MeV.

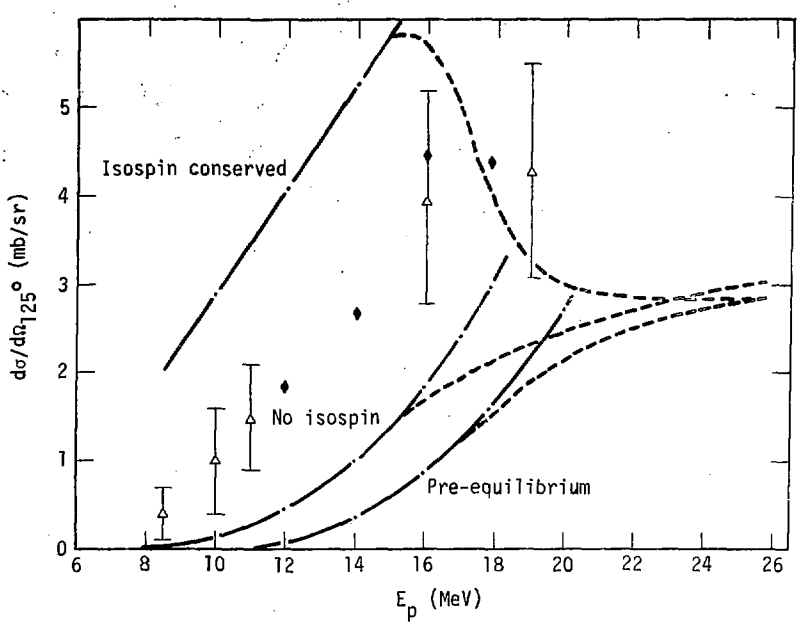

Fig. IV-20. The $^{120}Sn(p,p'\gamma)$ 1.172 MeV ($2^+ \rightarrow 0^+$) gamma cross section minus direct ($\hat{\Delta}$), HYBRID calculation (—·—), cut off at Bn+2 (— — —), and integrated proton data ($\diamond$); δ = 1.2 MeV.

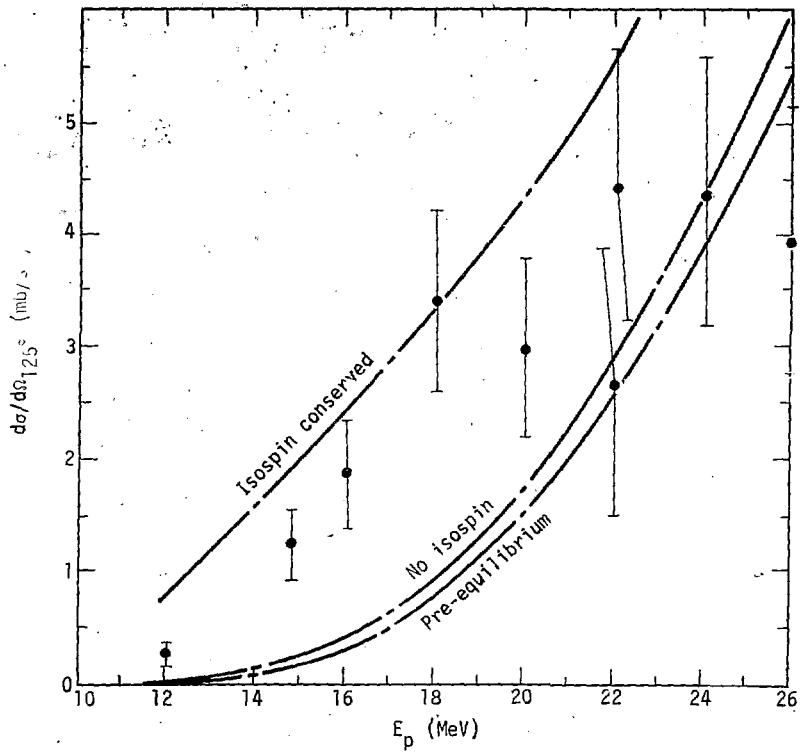

Fig. IV-21. The $^{206}Pb(p,p'\gamma)$ 0.803 MeV $(2^+ \rightarrow 0^+)$ gamma cross section minus direct (Φ), HYBRID calculation (——).

made to cut off the spectra above the neutron separation energy because of the limited applicability of the approach and the limited range of the data.

Comparison with (n,n'γ) Data

A comparison between (n,n'γ) $2^+ \rightarrow 0^+$ gamma cross sections and HYBRID calculations is made for Fe, Ni, Sn, and Pb in Table IV-1, for 14.8 incident neutrons. The table lists the HYBRID calculated cross section as a function of the energy above the neutron separation threshold at which the spectrum was cut off. Cutting the spectrum off at B_n + 1-MeV is a reasonable approximation to the Fe cross section while for Ni, a better approximation would be B_n + 2 MeV. For Sn, B_n + 3 MeV looks good while for Pb it is necessary to go all the way to B_n + 5 MeV. This behavior is identical to that observed with the (p,p') reactions. Clearly, trying to cut off the emission spectrum sharply just above the neutron separation threshold, i.e. the (n,2n) threshold in this case, does not yield very consistent or easily understood results. It is too much of a simplification, and one must actually calculate the two particle emission contribution to the total spectrum if accurate results are required.

TABLE IV - 1

HYBRID Calculations of (n,n') Reactions Compared With $(2^+ \rightarrow 0^+)$ Gamma Cross Sections at 14.8-MeV, Minus Direct

Nucleus	$\sigma(2^+ \rightarrow 0^+)$ (mb)	HYBRID Calculation Cut Off At (MeV) $B_n + 1$	$B_n + 2$	$B_n + 3$	$B_n + 4$	$B_n + 5$
^{56}Fe	503	443	737	1316	2054	-
^{62}Ni	>750	473	809	1464	2333	-
^{116}Sn	942	227	441	910	1932	3517
^{206}Pb	930	154	204	295	511	1116

B.2. The STAPRE Model and Calculations

The computer code STAPRE[68] is designed to calculate energy-averaged cross sections for particle-induced nuclear reactions with several emitted particles and gamma rays, under the assumption of sequential evaporation. Each evaporation step is treated within the framework of the statistical model and, unlike the HYBRID code, includes angular momentum and parity conservation explicitly. Pre-equilibrium emission is considered only in the first stage of the reaction. For that fraction of the population of the composite system that survives pre-equilibrium decay, the Hauser-Feshbach[65] formalism is applied, combined with the Brink-Axel[69] model of the gamma-ray strength functions.

The pre-equilibrium calculation is based on the exciton model of Griffin[45] as modified by Cline and Blann.[46] This is the master equation approach to pre-equilibrium calculations. Starting from a single initial configuration, the system approaches equilibrium through a series of two-body collisions, with a chance for particle emission occurring at each step in the equilibration process. From perturbation theory, the transition rate between states may be written as

$$\lambda_{\Delta p} = \frac{2\pi}{\hbar} |M|^2 W_{\Delta p}(p,h,E) \quad ,$$

where $W_{\Delta p}(p,h,E)$ is the particle-hole state density for a state with p particles, h holes, and energy E. The quantity Δp refers to the change in particle number of the system during the interaction and takes on values of +1, 0, -1. The parameter M is the average effective

two-body matrix element. It has been evaluated from a global search by Kalbach-Cline[70] and Kalbach et al.[71] The result of this search is that $|M|^2$ is found to have the form

$$|M|^2 = FM \cdot A^{-3} \cdot E^{-1} ,$$

where A is the mass number, E is the excitation energy and FM has been determined to be

$$FM = \begin{cases} 95 \pm 30 \text{ (ref. 70)} \\ 190 \quad \text{(ref. 71)} \\ 150 \pm 50 \text{ (ref. 72)} \end{cases} \quad \text{for nucleon induced reactions}$$

$$725 \pm 260 \text{ (ref. 70)} \quad \text{for alpha induced reactions}$$

The basic difference between the pre-equilibrium calculations in HYBRID and STAPRE is simply that the optical model is used to determine λ^+ in HYBRID and the parameter $|M|^2$ is used in STAPRE. The decays are treated similarly by the two methods.

The Hauser-Feshbach[65] evaporation model is applied to that fraction of reactions which survive pre-equilibrium emission. This fraction decreases with increasing incident particle energy. If a particle is emitted in a pre-equilibrium event, it is added to the Hauser-Feshbach cross section later. Moldauer[73] level width fluctuation corrections are also available for calculations at low energies, but were not used in this work. Gamma decay forms an additional emission channel and may be included at each step in the sequence of particle decays, starting with the compound system. In the calculations done for this work, the gamma cascade was calculated

only after the first particle emission. Since this pre-equilibrium model does not consider angular momentum and parity, it is assumed that the pre-equilibrium population is distributed among the levels with different spin and parity in the same proportion as the equilibrium contribution. This is undoubtedly a poor assumption and might be important in those cases in which pre-equilibrium emission is dominant.

The population of levels (E', I', π') by gamma emission from levels (E, I, π), where E, I and π represent energy, spin, and parity, respectively, is determined by the ratio of the partial width, $\Gamma_\gamma(E,E')$, to the total decay width $\Gamma(E)$, given by the expression

$$\frac{\Gamma_\gamma(E,E')}{\Gamma(E)} = \frac{1}{N} \sum_{XL} T_{\gamma XL}(E-E') \quad ,$$

where N is the Hanser-Feshbach denominator which consists of a sum of transmission coefficients for all open channels consistent with angular momentum and parity selection rules. The sum over XL is restricted by the multipole selection rules. The gamma-ray transmission coefficients, $T_{\gamma XL}$, are related to the strength functions, $f_{\gamma XL}$, by

$$T_{\gamma XL}(E_\gamma) = 2\pi E_\gamma^{2L+1} f_{\gamma XL}(E_\gamma) \quad ,$$

where the electric dipole strength function, $f_{\gamma E1}$, may be expressed in terms of E1 giant resonance parameters with an energy dependence given by the Lorentz form (Brink-Axel[69] model).

Two level density formulations were tried, both based on the Fermi gas model. These were the "back shifted" formalism[74] with

parameters determined by Dilq[75] and by Lu et al.,[12] and the Gilbert and Cameron[43] formalism with the constant temperature approximation at low energies.

Isospin-conserving (p,p') reactions to analog states have been found to be very important contributors to (p,p') cross sections. The STAPRE code was designed primarily for neutron induced reactions and consequently does not treat isospin conservation. Isospin conservation has been added to the Hauser-Feshbach formalism by Gardner,[76] following the perscription of Grimes et al.,[49] so that these calculations might be performed.

The STAPRE calculations for protons incident on ^{62}Ni were done with the "back shifted" level density parameters of Lu et al.,[12] which were determined from fitting experimental data in the A = 62 region. Gamma cascades were considered in the final nucleus, ^{62}Ni, only. Some 12 discrete levels in ^{62}Ni, up to about 4-MeV of excitation, were included in the calculation, and experimentally determined gamma branching ratios were used in this region. The initial state in the pre-equilibrium calculation was a two-particle, one-hole state and the effective two-body matrix element was FM = 195.

Comparison with (p,p') and (n,n') Data

First the calculated (p,p') and (n,n') spectra will be compared with experimental (p,p') and (n,n') spectra to see if the calculated results are reasonable. This is done in Fig. IV-22 and IV-23 for ^{62}Ni(p,p') spectra, where the Rao et al.[1] data (the ^{62}Ni cross sections appear to be all right) at 12 and 17-MeV and the Sprinzak et al.[5] data

at 14-MeV, are shown with the superimposed STAPRE calculations for the isospin conserved and no isospin (isospin mixed) cases. As the HYBRID calculations, the indication is that some isospin mixing occurs, but uncertainties in level density parameters do not permit a good estimate of the amount. The calculations are in reasonable agreement with the data. For 14-MeV incident protons, substantial numbers of (p,np) and (p,pn) protons can be seen appearing below 3-MeV. For 17-MeV incident protons, in Fig. IV-23 the spectrum is dominated by these protons, which appear below 6-MeV. The STAPRE calculation includes (p,p') and (p,pn) but not (p,np) events. It appears that (p,np) is the dominant proton contributor at low energies. The HYBRID calculation is also shown in this figure with the cut off at $B_n + 1 = 7$-MeV indicated. At this energy and for this nucleus this results in an overestimate of the (p,p') spectrum. Sharply cutting off the HYBRID calculation is an oversimplification and it appears that the fall off may actually occur over several MeV. This becomes a more severe problem as the energy increases and may account for the disagreement between cut off HYBRID calculations and the gamma data. Alternatively, the HYBRID calculation simply may not be producing enough preequilibrium emission.

Fig. IV-24 shows the ^{56}Fe(n,n') data of Kammerdiener[24] and others[57,58] with the STAPRE calculations superimposed. The direct collective contribution to this spectrum, as calculated by the coupled-channel code, has been added to the STAPRE calculation. The agreement between the measurement and the calculation is good, although multiple scattering corrections or better coupled-channel calculations might improve the agreement, since there is an indication that some cross section has been

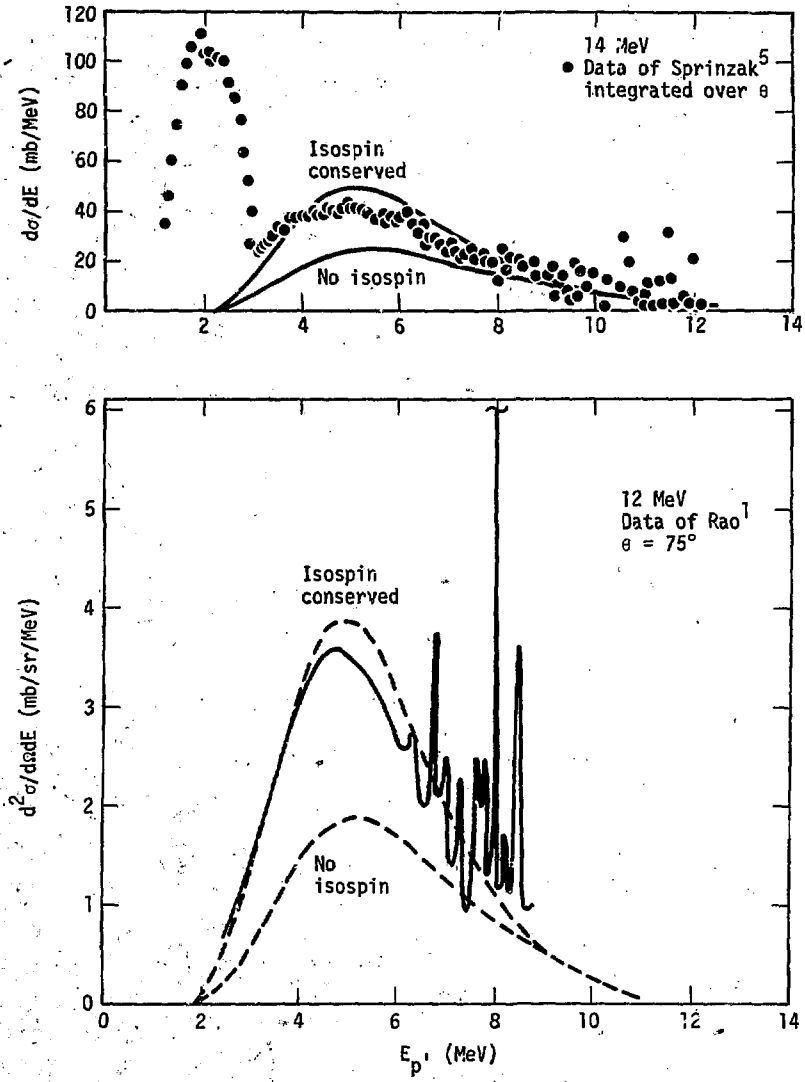

Fig. IV-22. ^{62}Ni(p,p') data with STAPRE calculations.

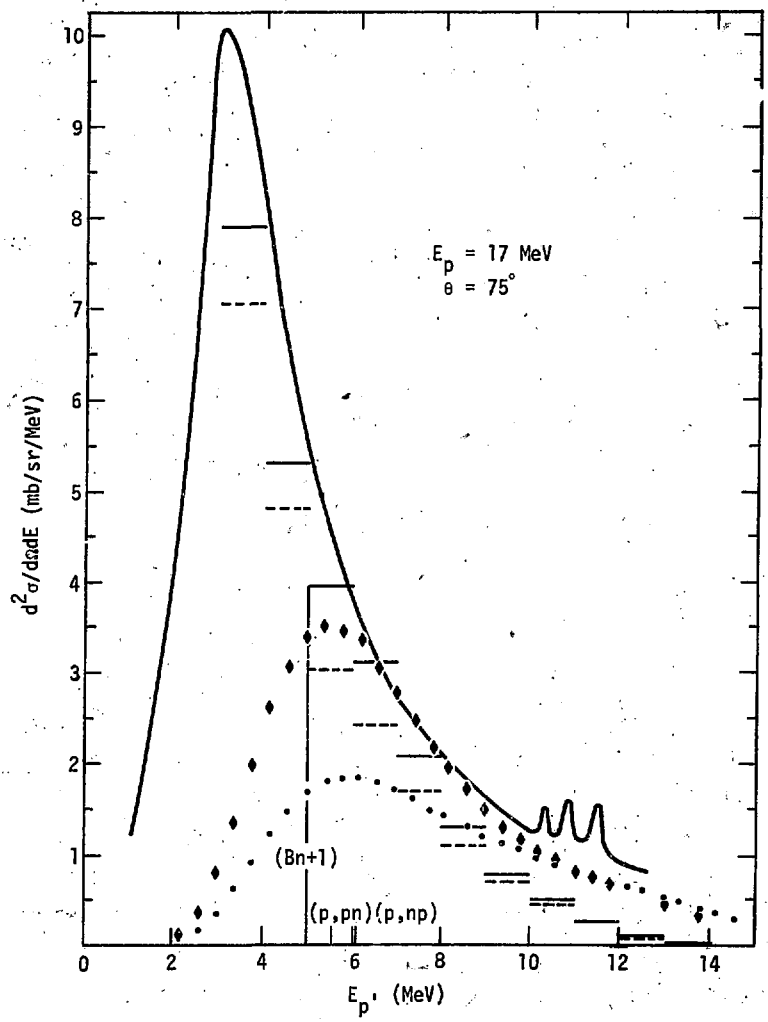

Fig. IV-23. The ^{62}Ni(p,p') data of Rao[1], STAPRE calculation with isospin (♦) and no isospin (•), and HYBRID calculations with isospin (——) and no isospin (---).

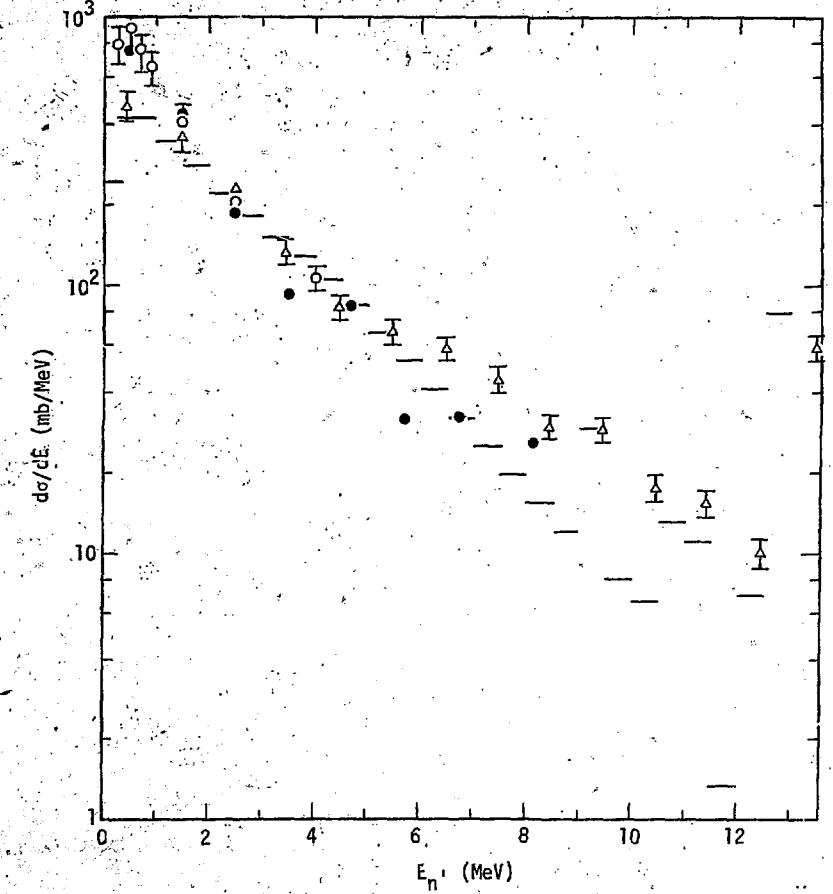

Fig. IV-24. The Fe(n,n') data of Kammerdiener[24] (Δ), Mathur[58] (●), and Clayeaux & Voignier[57] (○), and STAPRE calculations with direct (from coupled-channel calculations) added, for 14 MeV neutrons

missed at high energies. This could mean that it is necessary to include more levels than just the first one and two-phonon levels in the coupled-channel calculations.

Comparison with $(p,p'\gamma)$ and $(n,n'\gamma)$ Data

Since STAPRE calculates the gamma cascades, it is possible to compare measured gamma cross sections directly with calculated gamma cross sections. The $^{62}Ni(p,p'\gamma)$ gamma data from this work, with the STAPRE calculations superimposed, are shown in Fig. IV-25. The direct collective contribution to these transitions, as calculated by the coupled-channel code, has been added to the STAPRE calculations for the isospin conserved and isospin mixed (no isospin) cases. The agreement between measurement and calculation is, in general, quite good. Certainly the agreement is very good for the 1.173-MeV $(2^+\rightarrow 0^+)$ and the 1.163-MeV $(4^+\rightarrow 2^+)$ transitions, while it is only fair for the weaker 1.129-MeV $(2^+_1\rightarrow 2^+)$, 0.876-MeV $(0^+_1\rightarrow 2^+)$, and 2.301-MeV $(2^+_1\rightarrow 0^+)$ transitions. The calculation puts more strength into these weak transitions than was actually observed. Because only a very limited number of levels were included in the calculational description of the nucleus, it seems probable that the calculation has forced additional strength into these levels that would otherwise have been distributed among other weak transitions.

Fig. IV-26 shows the 1.173-MeV $(2^+\rightarrow 0^+)$ gamma transition, with the direct collective contribution subtracted, and the STAPRE calculation for isospin conserved and isospin mixed (no isospin). Between about 8 and 16-MeV, isospin mixing is clearly important and the data indicate a mixing fraction of about 50% would be appropriate. Above 16-MeV, the calculation without isospin gives a slightly better approximation to the data. Also shown are the

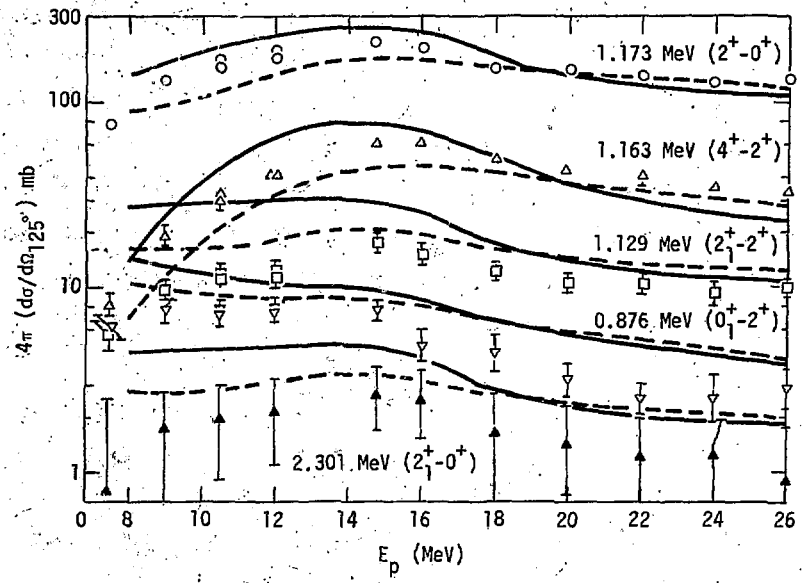

Fig. IV-25. The ^{62}Ni(p,p'γ) gamma cross sections with STAPRE calculations for isospin conserved (—), no isospin (--).

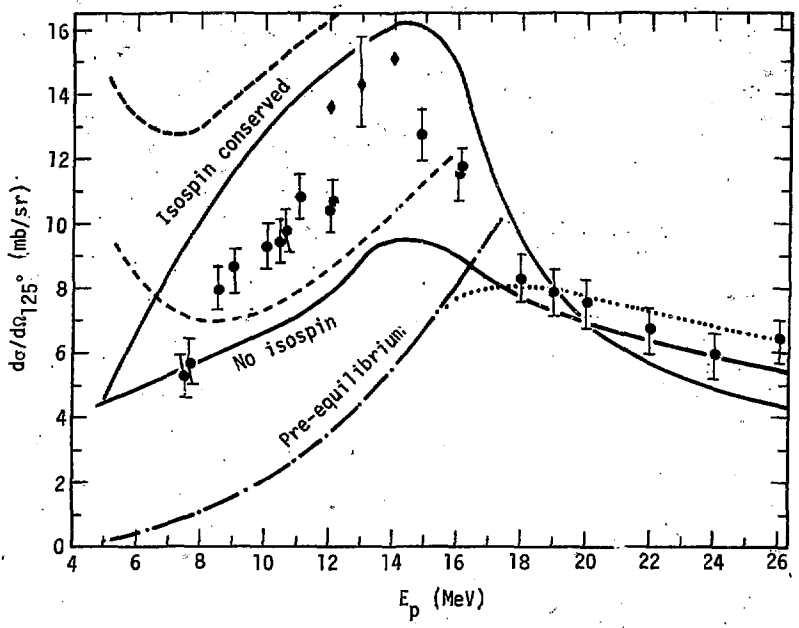

Fig. IV-26. The $^{62}Ni(p,p'\gamma)$ 1.173 MeV $(2^+ \rightarrow 0^+)$ gamma cross section minus direct (♦), STAPRE calculations for $(2^+ \rightarrow 0^+)$ gammas (——), for total protons (---), and for pre-equil. protons (-·-), cut off at Bn+1 (....), and integrated proton data (♦).

calculated proton cross sections. The dashed curves represent the total cross section, the dot-dash curve is the pre-equilibrium part, and the dotted curve represents the pre-equilibrium proton emission cross section cut-off at B_n + 1-MeV. This may be compared with the HYBRID calculations shown in Fig. IV-14 From 8 to 14-MeV, the proton emission cross sections calculated by the two codes are in good agreement. Above 14-MeV, it is necessary to cut off the proton emission spectra 1-MeV above the neutron separation energy (B_n + 1 MeV). In Fig. IV-26 only the pre-equilibrium part of the inelastic proton cross section is shown above 16-MeV. First, it is apparent that the Cline-Blann[46] formalism used in STAPRE predicts substantially more pre-equilibrium emission for ^{62}Ni(p,p') than does the HYBRID calculation. Second, the cut off pre-equilibrium proton cross sections are in good agreement with the gamma data and the gamma calculations, for incident protons with energies of 18-MeV and above, and account for all of the observed cross section going into (p,p'γ) events. The difference between the integrated proton spectra and the ($2^+ \rightarrow 0^+$) strength is due primarily to gamma transitions which bypass the first 2^+ state and decay directly to the ground state. Estimates of the strength of these transitions can best be obtained from the STAPRE calculations, once it has been determined that the calculations are reproducing the experimental data reasonably well.

Fig. IV-27 shows the amount of gamma decay bypassing the first 2^+ and going directly to the ground state, as a percentage of the total gamma decay cross section, for both ^{62}Ni(p,p') and ^{110}Cd(p,p'). As was indicated indirectly by our ($0_1^+ \rightarrow 2^+$) gamma data, this is important at low energies. For ^{62}Ni above 10-MeV and for ^{110}Cd above 16-MeV, less

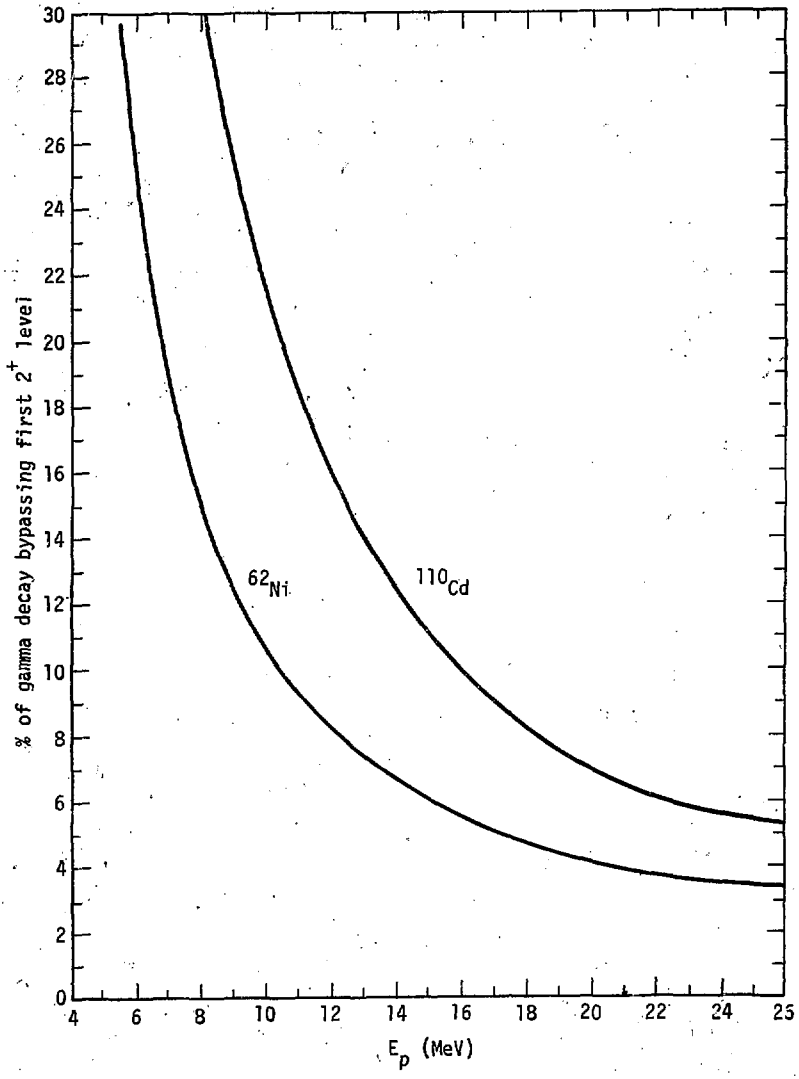

Fig. IV-27. Gamma decay bypassing the first 2^+ level for $^{62}Ni(p,p'\gamma)$ and $^{110}Cd(p,p'\gamma)$ from STAPRE calculations.

than 10% of the total gamma decay, or $(p,p'\gamma)$ cross section, bypasses the first 2^+ level. The displacement between these two calculated curves is probably due to Coulomb effects.

The $^{56}Fe(n,n'\gamma)$ total gamma cross section at 13.6-MeV was calculated to be 670 mb. Our measurement of the $2^+ \rightarrow 0^+$ gamma cross section yields 790 mb at about the same energy, which is in excellent agreement with the calculation. The total calculated neutron emission cross section is about 1065, however. If the (n,2n) cross section ($\sim$400 mb[59]) is subtracted from this, the result is 665 mb which is in good agreement with both the gamma data and the calculation. This indicates that little gamma strength bypasses the first 2^+ level for (n,n') reactions at about 14-MeV.

V. Conclusions and Recommendations

A. Conclusions About Experimental Methods

1. If one is to obtain reliable gamma cross sections from (p,p') or (n,n') experiments, it is necessary, in most cases, to employ pulsed beam and timing or coincidence techniques so that the spectra will not be contaminated by gammas from electron capture or beta decay from the products of (p,n) or (n,p) reactions, or from general background.

2. If very accurate absolute cross sections are desired, angular distributions of the gammas, for at least one energy, would be desirable, since it appears that errors of up to 9% are involved in neglecting the P_4 Legendre polynomial in the angular distribution by simply multiplying the measurement at 55° or 125° (where $P_2 \approx 0$) by 4π.

3. For the $(n,n'\gamma)$ experiments with large ring samples, it was found that the multiple scattering corrections could be significant (19% for Pb), at least above the (n,2n) threshold.

B. Conclusions Based on Experimentally Observed Systematics

1. When nuclei with the characteristic level structure shown in Fig. I-1 undergo gamma decay from highly excited states, the result is a cascade of gamma transitions down to the ground state. What is observed is that, for sufficiently high incident energies, nearly all of these decay cascades pass through the first 2^+ level, so that the $(2^+ \rightarrow 0^+)$ transition is very nearly a measure of the (n,n') or (p,p') part of the inelastic cross section. This conclusion is

based on comparisons with integrated experimental (p,p') spectra, inferences about transitions bypassing the first 2^+ level and feeding the 0^+ ground state based on the population of the 0_1^+ level, and model calculations.

The integrated (p,p') spectra generally agreed with the ($2^+ \rightarrow 0^+$) cross sections. Unfortunately the data were sparse and generally only available at relatively low energies, i.e. below 15-MeV. The (p,p') measurements often had experimental problems which were associated with trying to measure particle spectra down to low energies. For incident proton energies of 16 and 17-MeV, the spectra were dominated by low energy protons from (p,np) reactions which make the (p,p') cross section difficult to extract.

The feeding of 0^+ levels from the continuum becomes more important at low energies because little angular momentum is being brought into the nucleus. Hence transitions from the continuum directly to the ground state, not passing through the first 2^+ level, are more likely at low energies. This conclusion is based on observations of the population of the 0_1^+ level as a function of incident particle energy, and supported by STAPRE nuclear reaction model calculations which include a detailed model for the gamma-ray cascades. These calculations indicate that for ^{62}Ni(p,p') reactions, more than 90% of the gamma decay passes through the first 2^+ level for incident proton energies of more than 10-MeV; for ^{110}Cd(p,p') reactions, more than 90% passes through the first 2^+ level for incident proton energies of more than 16-MeV. The difference is probably due to the larger Coulomb barrier for ^{110}Cd and implies

that a larger percentage of decays through the 2^+ level would be obtained for neutron induced reactions. At low energies, the amount of gamma decay bypassing the 2^+ and going directly to the ground state appears to be significant.

2. Our measurements indicate that the cross sections for both the $(2^+ \rightarrow 0^+)$ and the $(4^+ \rightarrow 2^+)$ transitions rise with increasing incident proton energy to a maximum around 15-MeV. The $(4^+ \rightarrow 2^+)$ transition generally accounts for about half of the strength of the $(2^+ \rightarrow 0^+)$ transition, although in some nuclei the $(3^- \rightarrow 2^+)$ transition is stronger. Angular momentum effects cause the $(4^+ \rightarrow 2^+)$ cross section to peak at higher energies than does the $(2^+ \rightarrow 0^+)$ transition, while the $(0_1^+ \rightarrow 2^+)$ transition is maximum at very low energies and decreases steadily with increasing energy.

3. The strengths of the various gamma transitions for ^{62}Ni(p,p') reactions as functions of incident proton energy are reproduced reasonably well by the STAPRE calculations. The $(2^+ \rightarrow 0^+)$ and the $(4^+ \rightarrow 2^+)$ transition cross sections, which are by far the strongest, are reproduced very well, while the weaker $(2_1^+ \rightarrow 2^+)$, $(0_1^+ \rightarrow 2^+)$, and $(2_1^+ \rightarrow 0^+)$ transitions are somewhat overestimated by the calculation. It is believed that the extra strength calculated for the weak transitions would be divided up among other weak transitions if a more complete description of the levels had been available and had been used in the calculation.

4. Estimates of (n,n') cross sections at 14-MeV, obtained by subtracting cross sections for all competing reactions[59] from the

non-elastic cross sections, generally agree with our $(n,n'\gamma)$ data, within the uncertainties of the various measurements. The agreement is good for Fe, Ni, Zn, and Sn, but Cd, particularly ^{110}Cd, and ^{206}Pb show serious discrepancies. Since the (n,2n) reaction is the only serious competitor to the (n,n') reaction for these nuclei and at this energy, we suggest that the (n,2n) cross sections for these nuclei may not be reliable.

C. Implications for Reaction Mechanisms

1. Coupled-channel calculations have been used quite successfully to reproduce the direct, collective excitation of the low-lying levels in even-even nuclei as observed in (p,p') and (n'n') data. These calculations indicate that direct, collective reactions account for up to 50% of the $(2^+ \rightarrow 0^+)$ gamma cross section. For $(p,p'\gamma)$ reactions on the lighter elements Fe, Ni, and Zn, this percentage varies considerably with energy. For the heavier elements Pd, Cd, Sn, and Pb, the percentage remains essentially constant over the energy range of 10 to 26-MeV. For the $(n,n'\gamma)$ reactions at 14-MeV, the percentage of direct collective strength varied from 12% for ^{110}Cd to 48% for ^{116}Cd, reflecting the substantial decrease in (n,n') cross section with increasing isotopic mass. The direct, collective cross section itself remained relatively constant.

2. The (n,n') and (p,p') cross sections decrease rapidly with increasing isotopic mass, as has been observed from the $(2^+ \rightarrow 0^+)$ cross sections in this work and by Cohen et al.[1,14] However, even for the heavy isotopes, calculations indicate that below about 20-MeV

there is still some contribution from equilibrium compound nuclear processes, although only for isospin conserved reactions. The importance of these processes decreases with increasing energy, due to the onset of pre-equilibrium reactions, until, for energies exceeding 20-MeV, one can say that direct processes such as pre-equilibrium and direct, collective excitation account for essentially all of the (n,n') or (p,p') cross section.

3. Partial isospin conservation has been shown to be important in describing (p,p') reactions, at least for proton energies up to 18-MeV. Explicit inclusion of isospin in the calculations is important for the heavier nuclei Cd, Sn, and Pb, where in some cases HYBRID calculations indicate that all of the observed (p,p') cross section, other than that due to pre-equilibrium events, comes from $T_>$ states. For the lighter nuclei Fe and Ni, there is less difference between the isospin conserved and the isospin mixed calculations and for Zn they are nearly identical.

Substantial amounts of mixing of the $T_>$ states into the $T_<$ states are, in general, required to reproduce the data. Uncertainties in the parameters used to describe nuclear level densities and reactions do not allow an accurate determination of the amount of mixing, but it does seem to fall within the range of 0.3 to 0.7 (where 1.0 means complete isospin mixing).

Comparison of HYBRID calculations with the experimental data gives the impression that a systematic decrease in isospin mixing occurs with increasing mass in an isotopic sequence such as the Cd or Sn isotopes. This may just reflect the systematic decrease in (p,n)

Q values with increasing isotopic mass or the increase in symmetry energy. Alternatively, it might simply be a consequence of the global parameters (particularly the level density parameter) not being sensitive enough to changes in isotopic mass.

4. An attempt was made to compare HYBRID and STAPRE (p,p') calculations with ($2^+ \rightarrow 0^+$) gamma cross sections above the neutron separation energies (B_n) of the various nuclei by cutting off the emission spectra at B_n + 1 or B_n + 2 MeV. This was done in an attempt to eliminate low energy protons from (p,np) and (p,pn) reactions, which tended to dominate the emission spectra as the incident energy increased above B_n. In general this failed at high energies for the HYBRID calculations. The cut off cross section was only about half of what was observed. Cutting off the STAPRE ^{62}Ni(p,p') spectrum at B_n + 1 was consistent with the calculated ($2^+ \rightarrow 0^+$) gamma strength and agreed with our measured ($2^+ \rightarrow 0^+$) gamma cross sections. Between 8 and 14-MeV the STAPRE and HYBRID calculations agree at least in the case of ^{62}Ni for which a complete STAPRE calculation was made. The Cline-Blann[46] pre-equilibrium formalism used in STAPRE calculates substantially more pre-equilibrium emission at all energies than does HYBRID, and for energies above 18-MeV, the STAPRE calculated pre-equilibrium emission accounts for essentially all of the observed cross section.

Because of the ambiguities involved in cutting off the calculated emission spectra, and because (n,2n) reactions are such strong competitors with (n,n') reactions once the neutron separation energy (B_n) is exceeded, it is difficult to compare the (n,n'γ) data at 14-MeV with the HYBRID calculations. The appropriate effective

cut off appears to increase from $B_n + 1$ for ^{56}Fe to $B_n + 5$ for ^{206}Pb, which tells us that something is amiss in either the calculation for heavier nuclei or in the procedure of sharply cutting off the spectra above the neutron binding energy.

5. HYBRID calculations reproduce experimental (p,p') spectra of ^{56}Fe, ^{62}Ni, ^{64}Zn, and the Cd and Sn isotopes at low energies (below 15-MeV), and the $^{110}Cd(p,p')$ data of Lux et al. at 16-MeV, but fail to reproduce the other Cd and Sn data at 16 and 17-MeV. The calculation appears to fail to produce enough pre-equilibrium emission at high incident particle energies, a conclusion which is supported by the failure of the cut off emission spectra to reproduce the gamma data.

The HYBRID calculations for (n,n') reactions on Fe, Ni, and Pb reproduce the data quite well. The Pb data are systematically slightly high, perhaps because of uncorrected multiple scattering effects.

D. Recommendations for Future Experiments

In the course of doing the work described here, certain ideas and experimental techniques evolved which might be of value to someone doing related work in the future. First, if more accurate absolute cross sections are desired, it would be worthwhile to measure the angular distributions of the gammas for at least one energy. Next, a series of proton-gamma coincidence experiments for $(p,p'\gamma)$ reactions on some of the nuclei discussed in this work could yield some valuable information on pre-equilibrium reactions and the behavior of other reaction mechanisms with changes in incident particle energy.

For instance, if the scattered proton spectra in coincidence with the $2^+ \rightarrow 0^+$ gamma transition were determined, it would be due entirely to (p,p') events. If this were compared with the singles (p,p') spectra as a function of energy it would be possible to separate the (p,np) and (p,p') reactions and to examine their behavior as a function of energy. At high energy (above 24-MeV) this work has indicated that the (p,p') reaction is due almost entirely to pre-equilibrium reactions. These coincidence measurements would allow the experimental determination of a nearly pure pre-equilibrium (p,p') spectrum which could be very valuable for comparison with pre-equilibrium model calculations, especially if the measurements were done over a range of nuclei and for several nuclei in an isotopic sequence.

If gamma spectra were taken in coincidence with a series of energy windows placed on the scattered proton spectrum, it would be possible to examine the change in intensity of the gammas, from the various levels of interest, as a function of the energy of the outgoing particle. This could provide valuable information on the behavior of the gamma cascade under changing energy and angular momentum conditions. In addition, the various portions of the proton spectra can nominally be identified with different reaction mechanisms, i.e. the evaporation peak, the pre-equilibrium region, and the (p,np) peak, etc. More information about these reactions and their contributions to the gamma cascade could be obtained by doing these coincidence experiments.

Appendix I - Multiple Scattering from the Copper Shadow Shield

Since the copper shadow shield is massive and quite close to both the tritium target and the scattering ring, neutrons scattered from it back onto the ring might be important. Figure A-I-1 shows the configuration to be calculated.

The flux of source neutrons at the front face of the slug is

$$\phi_{S_o} = \frac{S_o}{4\pi x_o^2} \quad .$$

The reaction rate at position x in the slug is

$$dR_n(x) = \phi_S \pi \frac{d^2}{4} e^{-\sigma N x} \sigma N dx \quad .$$

The flux of scattered neutrons on the ring is (assuming the slug to be a line source of neutrons)

$$d\phi_R(x) = \frac{dR_n(x)}{4\pi r^2} \quad .$$

$$\therefore \quad \phi_R = \int_o^{\ell} \frac{dR_n(x)}{4\pi r^2} = \phi_{S_o} \frac{\pi d^2}{16\pi} \int_o^{\ell} \frac{\sigma N e^{-\sigma N x} \, dx}{(r_o^2 + (x_o + x - y_o)^2)} \quad .$$

We assume that

$x_o = 10$ cm,

$y_o = 10$ cm,

and $r_o = 10$ cm,

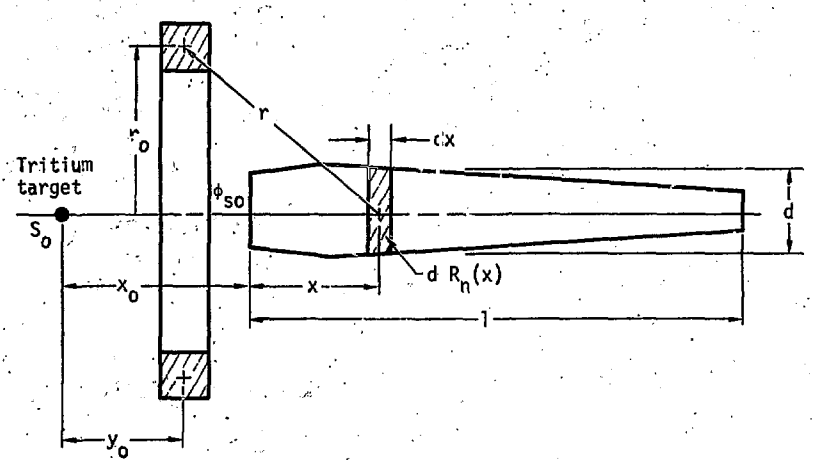

Fig. A-I-1. The scattering ring and shadow bar for the multiple scattering calculation.

and we know that

$$S_o = 1.1 \times 10^9 \text{ n/s},$$

$$N = \frac{N_A \rho}{M} = 8.46 \times 10^{22} \text{ nuclei/cc},$$

$$d = 6.2 \text{ cm}, \ell = 46 \text{ cm},$$

and $\sigma_{\text{non elastic}} = 1.5$ b for 14-MeV neutrons.

The resulting integral cannot be solved analytically but can be estimated by assuming

$$\phi_R = A \int_o^{\ell} \frac{ae^{-ax}\,dx}{b^2 + x^2}\,dx \simeq A \int_o^{\ell} \frac{ae^{-ax}}{b^2}\,dx = 2 \times 10^4 \frac{n}{cm^2 \cdot sec},$$

where

$$A = 2.09 \times 10^6,$$

$$a = 0.127,$$

and $b = 10$.

Integrating numerically yields

$$\phi_R = 1.4 \times 10^4 \frac{n}{cm^2 \cdot sec}.$$

The flux directly from the source on the ring is

$$\phi_S = \frac{S_o}{4\pi(y_o^2 + r_o^2)} = 4.4 \times 10^5 \frac{n}{cm^2 \cdot sec}$$

The scattered contribution is only 3% of the direct source contribution.

Monte carlo calculations indicate that the neutrons scattered from the copper shield have an energy distribution peaked near 14 MeV, since elastic scattering is the dominant reaction mechanism. These calculations

support the analytical calculation and indicate that the copper shield adds about 3% to the (n,n') cross section.

References

1. G. R. Rao, R. Balasubramanian, B. L. Cohen, C. L. Fink, J. H. Degnan, *Phys. Rev.* C4, 1855 (1971).
2. J. C. Davis, J. D. Anderson, E. K. Freytag, D. R. Rawles, *IEEE Trans. Nucl. Sci.*, NS-20, 213 (1973).
3. P. R. Bevington, *Data Reduction and Error Analysis*, McGraw-Hill, 1969.
4. D. W. Marguardt, "An Algorithm for Least-Squares Estimation of Nonlinear Parameters", *J. Soc. Ind. Appl. Math.*, 11 (2) 431-441 (1963).
5. A. Sprinzak, A. J. Kennedy, J. C. Pacer, J. Wiley, N. T. Porile, *Nucl. Phys.*, A203 280 (1973).
6. J. R. Huizenga and R. Vandenbosch, *Phys. Rev.*, 120, 1305 (1960). R. Vandenbosch and J. R. Huizenga, *Phys. Rev.*, 120, 1313 (1960).
7. S. F. Eccles, H. F. Lutz, V. A. Madsen, *Phys. Rev.*, 141, 1067 (1966).
8. C. Kalbach-Cline, J. R. Huizenga, H. K. Vonach, *Nuc. Phys.*, A222, 405 (1974).
9. J. H. Degnan, B. L. Cohen, G. R. Rao, K. C. Chan, L. Shabason, *Phys. Rev.* C8, 2255 (1973).
10. J. R. Huizenga and G. Igo, *Nucl. Phys.*, 29, 473 (1962).
11. W. Zobel, et al., *Gamma Rays from Bombardment of ^{7}Li, Be, ^{11}B, C, O, Mg, Al, Co, Fe and Bi by 16 to 160-MeV Protons and 59-MeV Alpha Particles*, ORNL-4183 (1967), Oak Ridge National Laboratory.
12. C. C. Lu, L. C. Vaz, J. R. Huizenga, *Nucl. Phys.*, A190, 229 (1972).
13. C. R. Lux, N. T. Porile, *Nuc. Phys*, A277, 413 (1977).
14. B. L. Cohen, G. R. Rao, J. H. Degnan, C. K. Chan, *Phys. Rev.* C7, 331 (1973).
15. A. H. Wapstra, N. B. Gove, *Nuclear Data Tables* 9, 267 (1971).
16. C. R. Lux, N. T. Porile, S. M. Grimes, *Phys. Rev. C* (to be published).

17. M. J. Stomp, F. A. Schmittroth and V. A. Madsen, *The Oregon State Coupled-Channel Code*, Contract No. AT(45-1)-2227.

18. T. Tamura, *Rev. Mod. Phys.*, 37, 679 (1965).

19. F. D. Becchetti and G. W. Greenlees, *Phys. Rev.*, 182, 1190 (1969).

20. D. Wilmore and P. E. Hodgson, *Nuc. Phys.*, 55, 673 (1964). (with the correction, W = 9.52 - 0.053 E, made on pp. 676)

21. P. H. Stelson, L. Grodzins, *Nuc. Data*, A1, 21 (1965).

22. V. A. Madsen, V. R. Brown, and J. D. Anderson, *Phys. Rev.*, C12, 1205 (1975).

23. T. H. Curtis, H. F. Lutz, W. Bartolini, *Phys. Rev.*, C1, 1418 (1970).

24. J. L. Kammerdiener, Ph.D. Thesis, *Neutron Spectra Emitted by* ^{239}Pu, ^{238}U, ^{235}U, *Pb, Nb, Ni, Al, and C Irradiated by 14-MeV Neutrons*; UCRL-51232 (1972), Lawrence Livermore Laboratory.

25. *Nuclear Data Sheets*, B3 (3,4) 43 (1970), A = 56; 19 445 (1976), A = 58; 16 317 (1975), A = 60; 13 443 (1974), A = 62; 12 305 (1974), A = 64; 16 383 (1975), A = 66; B7 33 (1972), A = 108; B5 487 (1971), A = 110; B7 69 (1972), A = 112; 16 107 (1975), A = 114; 14 247 (1975), A = 116; 17 1 (1976), A = 118; 17 39 (1976), A = 120; B7 161 (1972), A = 206; B5 243 (1971), A = 208.

26. R. B. Day, *Phys. Rev.*, 102 767 (1956).

27. E. F. Plechaty, J. R. Kimlinger, *TARTNP: A Coupled Neutron-Photon Monte-Carlo Transport Code*, UCRL-50400, 14 (1976), Lawrence Livermore Laboratory.

28. J. Lachkar, et al., *Nuc. Sci. Engr.*, 55 168 (1974).

29. E. Sheldon and D. M. Van Patter, *Rev. Mod. Phys.*, 38 143 (1966).

30. U. Abbondanno, R. Giacomich, M. Lagonegro, G. Pauli, *J. Nucl. Energy* 27 227 (1973).

31. P. W. Martin and D. T. Stewart, *J. Nucl. Energy*, 19 447 (1965).

32. J. K. Dickens, G. L. Morgan, F. G. Perey, *Nuc. Sci. Engr.*, 50 311 (1973).

33. R. L. Robinson, F. K. McGowan, P. H. Stelson, W. T. Milner, R. O. Sayer, *Nuc. Phys.*, A124 553 (1969).

34. F. Bjorklund and S. Fernbach, *Phys. Rev.*, 109 1295 (1958).

35. R. L. Auble, *Nuclear Data Sheets*, 12 322 (1974).

36. J. Benveniste, et al., *Phys. Rev.*, 133 B323 (1964).

37. H. F. Lutz, W. Bartolini, T. H. Curtis, *Phys. Rev.*, 178 1911 (1969).

38. C. Glashausser, D. L. Hendrie, J. M. Loiseaux, E. A. McClatchie, *Phys. Letters*, 31B 289 (1970).

39. B. Joensson, K. Nyberg-Ponnert, I. Bergqvist, *Arkiv. Fysik*, 39 295 (1965).

40. M. Blann, *Nuc. Phys.*, A213 570 (1973).
M. Blann, *Ann. Rev. of Nuc. Sci.*, 25 123 (1975).
M. Blann, *Phys. Rev. Lett.*, 27 337 (1971).
M. Blann, *Phys. Rev. Lett.*, 28 757 (1972).
M. Blann, R. R. Doering, A. Galonsky, D. M. Patterson, F. E. Serr, *Nuc. Phys.*, A257 15 (1976).

41. J. M. Blatt and V. F. Weisskopf, *Theoretical Nuc. Physics*, p. 340, John Wiley & Sons Inc., New York (1952).

42. S. M. Grimes, J. D. Anderson, C. Wong, *Phys. Rev.* C13 2224 (1976).

43. A. Gilbert and A. G. W. Cameron, *Can. J. Phys.*, 43 144 (1965).

44. S. M. Grimes, J. D. Anderson, J. W. McClure, B. A. Pohl, C. Wong, *Phys. Rev.*, C10 2373 (1974).

45. J. J. Griffin, *Phys. Rev. Lett.*, 17 478 (1966).

46. C. K. Cline and M. Blann, *Nuc. Phys.*, A172 225 (1971).

47. M. Blann, et al., *Nucl. Phys.*, A257 15 (1976).

48. L. Hansen, S. M. Grimes, R. J. Howerton, J. D. An[illegible] *Nucl. Sci. Eng.*, 61 201 (1976).

49. S. M. Grimes, J. D. Anderson, A. K. Kerman, C. Wong, *Phys. Rev.* C5 85 (1972).

50. P. E. Nemirovsky and Yu. V. Adamchuk, *Nuc. Phys.* 39 551 (1962).

51. M. J. Fluss, J. M. Miller, J. M. D'Auria, N. Dudey, B. M. Foreman, L. Kowalski, R. C. Reedy, *Phys. Rev.*, 187 1449 (1969).

52. N. T. Porile, J. C. Pacer, J. Wiley, C. R. Lux, *Phys. Rev.*, C9 2171 (1974).

53. C. R. Lux, N. T. Porile, *Nuc. Phys.* A248 441 (1975).

54. D. H. Wilkinson, *Phil. Mag.*, 1 379 (1956).

55. A. M. Lane, R. G. Thomas, *Rev. Mod. Phys.*, 30 257 (1958).

56. V. A. Madsen, "Inelastic Scattering and Charge Exchange", *Nuclear Spectroscopy and Reactions*, Part D, pp. 249, J. Cerny, Ed., Academic Press, Inc., New York (1975).

57. G. Clayeaux and J. Voignier, *Diffusion Non Elastic de Neutrons de 14-MeV Sur Mg, Al, Si, S, Ca, Sc, Fe, Ni, Cu, Au, Pb, Bi*, CEA-R-4279, Centre-de'Etudes de Limeil (1972).

58. S. C. Mathur, P. S. Buchanan, I. L. Morgan, "Inelastic Neutron Scattering Cross Sections in Several Elements with 15-MeV Neutrons", NDL-TR-86, Texas Nuclear Corp. (1967); *Phys. Rev.*, 186 1030 (1969).

59. R. J. Howerton, et al., *An Integrated System for Production of Neutronics and Photonics Calculational Constants*, UCRL-50400, 8, Rev. 1, Lawrence Livermore Laboratory (1976).

60. P. Guenther, et al., *Measured and Evaluated Fast Neutron Cross Sections of Elemental Nickel*, ANL/NDM-11, Argonne National Laboratory (1975).

61. V. F. Weisskopf, *Phys. Rev.*, 52 295 (1937).

62. I. Halpern, "Evaporation Spectra", *Statistical Properties of Nuclei*, pp. 465, J. B. Garg, Ed., Plenum Press, New York-London (1972).

63 J. R. Huizenga, "Experimental and Theoretical Nuclear Level Densities", *Statistical Properties of Nuclei*, pp. 425, J. B. Garg, Ed., Plenum Press, New York-London (1972).

64. Perey and Perey, *Atomic Data and Nuclear Data Tables*, 13 (4) 294 1974 (with the correction, V = 47.01 - 0.267E - 0.00118E^2, made on page 296).

65. L. Wolfenstein, *Phys. Rev.* 82 690 (1951).

66. P. Marmier, E. Sheldon, *Physics on Nuclei and Particles*, II 10 (1970).

67. V. A. Madsen, private communication.

68. M. Uhl, B. Strohmaier, "STAPRE, A Computer Code for Particle Induced Activation Cross Sections and Related Quantities", IRK-76/01, Irstitut für Radiumforschung and Kernphysik der Österreichischen Akademic der Wissenchatten, Vienna (1976).

M. Uhl, *Nuc. Phys.*, A184 253 (1972).

M. Uhl, *Acta Physica Austriaca*, 31 245 (1970).

69. G. A. Bartholomew, et al., *Advances in Nuclear Physics*, 7, Chapt. 4, Plenum Press, N.Y. (1973).

P. Axel, *Phys. Rev.*, 126 671 (1962).

70. C. Kalbach-Cline, *Nuc. Phys.*, A210 590 (1973).

71. C. Kalbach, S. M. Grimes, C. Wong, *Z. Physik*, A275 175 (1975).

72. G. M. Braga-Marcazzan, E. Gadiolo-Erba, L. Milazzo-Colli, P. G. Sona, *Phys. Rev.*, C6 1398 (1972).

73. P. A. Moldaner, *Rev. of Mod. Phys.*, 36 1079 (1964).

74. H. K. Vonach, M. Hille, *Nuc. Phys.*, A127 289 (1969).

75. W. Dilg, et al., *Nuc. Phys.*, A217 269 (1973).

76. D. Gardner, private communication, 1976

77. J. P. Davidson, *Collective Models of the Nucleus*, pp. 96, Academic Press, New York and London (1968).